STEEL 3D PRINTING FOR STRUCTURES

AN EXPLORATIVE STUDY ON THE TEAR-OUT STRENGTH OF A PIN OR BOLT IN A WIRE AND ARC ADDITIVELY MANUFACTURED CARBON STEEL PLATE

GEERTE KOTTEMAN

MSC THESIS

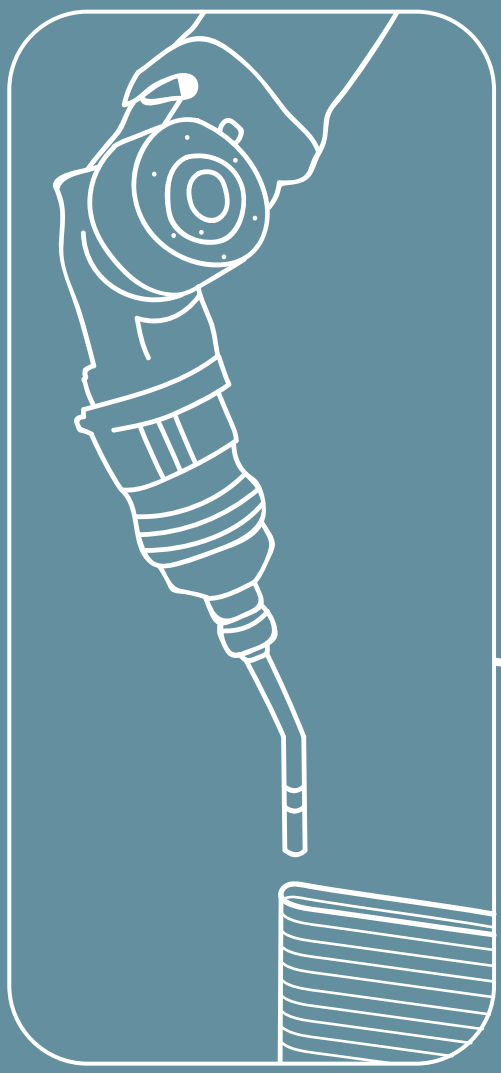

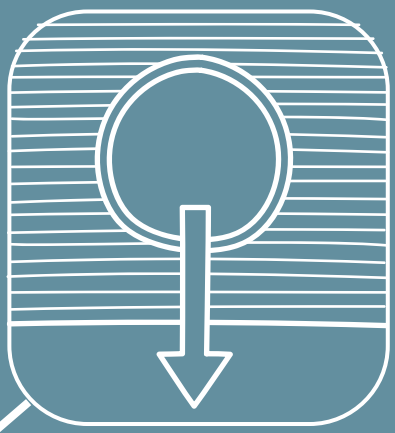

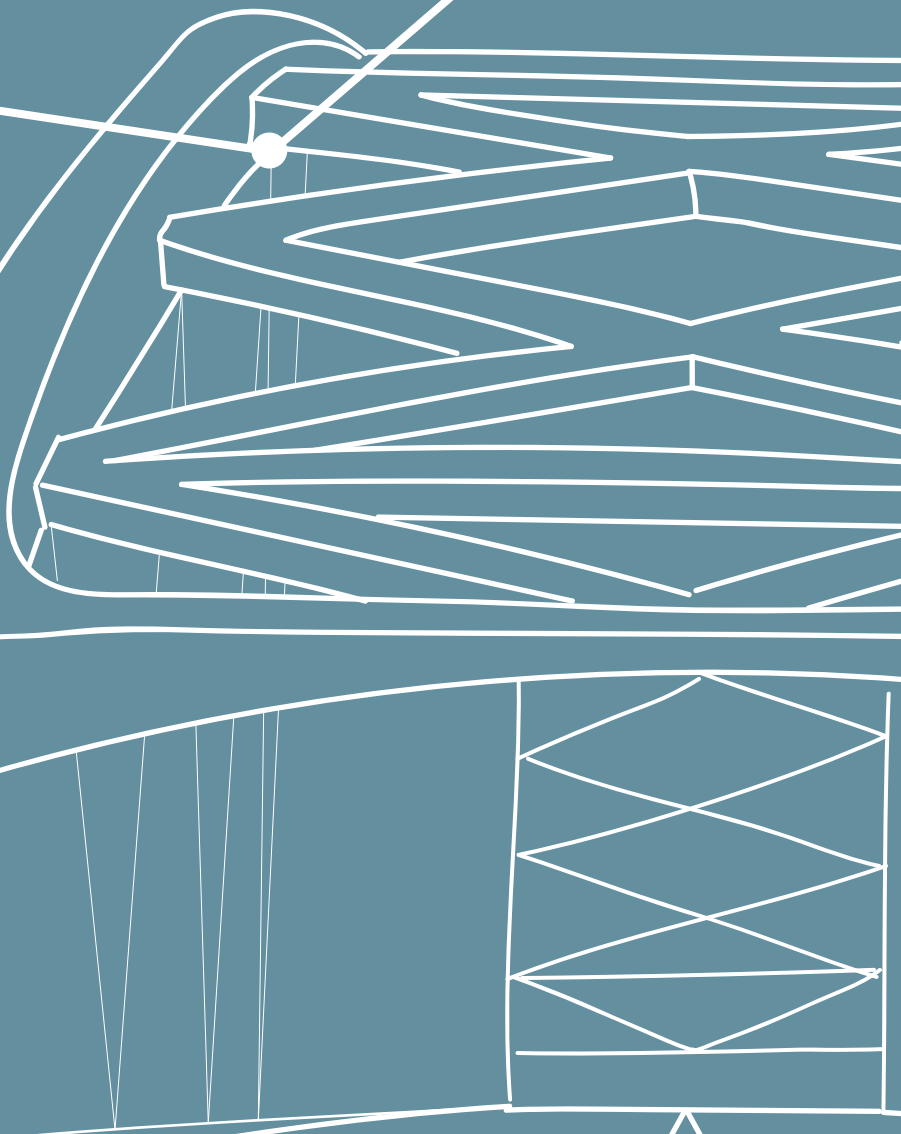

TUDelft

Steel 3D printing for structures

An explorative study on the tear-out strength of a pin or bolt in a Wire and Arc Additively Manufactured carbon steel plate

by

Geerte M.G. Kotteman

to obtain the degree of Master of Science
at the Delft University of Technology,
to be defended publicly via Zoom on Thursday July 2, 2020 at 1:00 PM.

Student number:	4223225	
Project duration:	December 4, 2018 – July 2, 2020	
Thesis committee:	Prof. dr. ir. M. Veljkovic,	TU Delft, chair
	Dr. ir. M.J.M. Hermans,	TU Delft
	Ir. P.A. de Vries,	TU Delft, daily supervisor
	Ir. G.S. van Bolderen,	Royal HaskoningDHV, company supervisor

An electronic version of this thesis is available at http://repository.tudelft.nl/.

TU Delft Delft University of Technology

MX3D

Royal HaskoningDHV
Enhancing Society Together

Preface

This master thesis research has been a very extensive and challenging project. I gained a lot of knowledge by doing research, performing experiments, communicating, writing and presenting. I am very happy to finalise my study career with this result.

Firstly, I would like to thank Royal HaskoningDHV for giving me the opportunity to work on my thesis under their supervision. I have learned and seen a lot from this engineering company. I want to express gratitude to Geoffrey van Bolderen, who advised me and learned me a great deal throughout the whole process; from tiny grammar errors in my report to the bigger picture of the relevance of my research. I could profit from his knowledge about the subject.

Second of all, I would like to thank MX3D and Filippo Gilardi specifically, for producing the carbon steel objects by wire and arc additive manufacturing for my tensile coupons and tear-out specimens, so I could conduct the experiments in the laboratory of Stevin at the Civil Engineering faculty. There, I was guided by the employees and Giorgos Stamoulis mainly, whom I worked together with gratefully.

Peter de Vries was also nearby or in the laboratory and he was always available to answer my questions. When it came to the experimental tests, this happened even more eagerly. Also, I want to thank professor Milan Veljkovic, who led me through the academic process of writing a thesis.

Material Science professor Ian Richardson and Marcel Hermans have shown me a lot on the complicated microstructural behaviour of carbon steels.

I would like to thank my friends; my room- and clubmates for supporting me, those who were in the same phase for mental support and those who were not for distractions. It was good to have you around at the TU Delft or at home. I had good brainstorm sessions with Laura van Utenhove. I want to thank Nina van Wijk in particular; for making the beautiful front page of my report and for being my graduation buddy in good and bad times.

A last thanks is for my parents and Frederik, who love me and embraced me when I needed it the most. They know everything about this subject now and they can even answer most of the questions.

Geerte M.G. Kotteman
Delft, June 2020

Abstract

Additive manufacturing (AM), or 3D printing, is emerging as a technology for different applications made of steel. It is expected that in the coming years the construction industry will benefit from the free and lightweight forms that can be fabricated and the possible material savings.

A few experimental results of 3D printed stainless steel are published, while no data is available on the material properties of wire and arc additively manufactured (WAAM) low carbon steel nor on specific connections. Carbon steel is widely applied in the construction industry and is less expensive, compared to other types of steel, as stainless, which was investigated for WAAM in other studies, at the TU Delft and abroad. Therefore, WAAM low carbon steel plates with thicknesses of 3 and 6 mm, produced by the company MX3D, were investigated thoroughly in this research.

Tensile coupon tests were performed to determine the strength, stiffness and ultimate strain. The surface roughness, effective thickness and the influence of the thickness and the printing direction on the material properties were investigated by experiments and an evaluation of 3D scanning and Digital Image Correlation (DIC). The Archimedes' principle was used to establish an effective thickness. The experiments were conceived to predict the tear-out failure behaviour of 3D printed plates. This is one of the basic failure modes in bolted connections. The conducted experiments provide the necessary evidence for the behaviour of single bolts and pins that interact with the WAAM material. A design formula for bolted and pinned connections is proposed based on experimental results.

The results of the tensile and tear-out tests were compared with conventionally produced carbon steel and existing findings on WAAM stainless steel. The influence of the end distance of a double lap bolted connection is evaluated by comparing the experimental results with the existing standards and studies on rolled carbon steel. This research was performed to assess the applicability of current design standards for conventionally produced carbon steel to WAAM low carbon steel connections. The reliability of this method was checked by a statistical analysis.

A new design factor for the tear-out strength of single bolts and pins in a WAAM low carbon steel plate is recommended. This factor reduces the design resistance of a tear-out connection and includes the ultimate tensile strength of the WAAM low carbon steel, the end distance, effective thickness of the plate and printing direction, compared to the applied force. The reduction factors that originate from the effective thickness determination and that reduce the ultimate tensile strength due to the surface roughness effect have to be incorporated for WAAM material as well.

The starting hypothesis was confirmed by the investigation and following is concluded: WAAM carbon steel is a suitable material for structural applications, due to its lower costs and higher stiffness compared to the stainless steel alternatives. The experimental results of this research are meant to be used for design purposes and as input for Finite Element Modelling, so the resistance of more complex geometries can be studied accordingly. It is expected that with topology optimisation (TO) of connections, considering the printing direction, and the consequential material efficiency, full potential of 3D printing can be yielded for the manufacturing of structural parts.

Contents

Nomenclature

Abbreviations

3D	Three Dimensional
AISC	American Institute of Steel Construction
AM	Additive Manufacturing
BS	British Standard
CAD	Computer-Aided Design
CCT	Continuous Cooling Transformation
CNC	Computer Numerical Control
DIC	Digital Image Correlation
DMD	Direct Metal Deposition
DMLS	Direct Metal Laser Sintering
DMP	Direct Metal Printing
EBAM	Electron Beam Additive Manufacturing
EBM	Electron Beam Melting
EC	Eurocode standard
FEA	Finite Element Analysis
FEM	Finite Element Model(ling)
GMAW	Gas Metal Arc Welding
GTAW	Gas Tungsten Arc Welding
HAZ	Heat Affected Zone
HSS	High Strength Steel
IT	Information Technology
ISO	International Organization for Standardization
LENS	Laser Engineered Net Shaping
LMD	Laser Metal Deposition
LMF	Laser Metal Fusion
MAG	Metal Active Gas
MIG	Metal Inert Gas
NEN	NEderlandse Norm
PAW	Plasma Arc Welding
SEM	Scanning Electron Microscope
SEM	Standard Error of the Mean
SLM	Selective Laser Melting
TIG	Tungsten Inert Gas
TS	Travel Speed
WAAM	Wire and Arc Additive Manufacturing
WFS	Wire Feed Speed
WLAM	Wire Laser Additive Manufacturing

Roman symbols

Symbol	Description	Unit
A_{corner}	Area corner tensile coupon	mm^2
A_{total}	Total area	mm^2
c	Clearance hole	mm
d	Diameter bolt	mm
d_0	Diameter bolt hole	mm
E	Young's modulus	N/mm^2
e_1	End distance	mm
e_1'	New end distance Kamtekar	mm
e_2	Edge distance	mm
e_3	New end distance	mm
F	Force	kN
F_e	Maximum force experiment	kN
$F_{max,\,as-printed}$	Maximum force as-printed specimen	kN
F_t	Maximum theoretical force	kN
f_E	Strength for determination of E	MPa
f_u	Ultimate tensile strength	MPa
$f_{u,\,milled}$	Ultimate tensile strength milled specimen	MPa
f_y	Yield strength	MPa
I	Welding current	A
L	Length	mm
L_{end}	Length outer parts tensile coupon	mm
L_f	Fracture line length	mm
L_{middle}	Length middle part tensile coupon	mm
L_0	Initial length	mm
ΔL	Change in length	mm
$\Delta L_{fracture}$	Elongation at fracture	mm
m_1	Mass dry	kg
m_2	Mass in water	kg
n	Number of samples or tests	-
P	Force	kN
p_1	Spacing between bolts	mm
p_2	Spacing between bolts	mm
R_a	Average roughness	μm
R_d	Design resistance	
R_{nom}	Nominal resistance	
r	Radius	rad
t	Thickness	mm
Δt	Change in thickness	mm
t_{avg}	Average thickness	mm
t_{eff}	Effective thickness	mm
t_{max}	Maximum thickness	mm
t_{min}	Minimum thickness	mm
U	Arc voltage	V
V	Volume	m^3
v_{travel}	Travel speed	mm/min
V_x	Coefficient of Variation	-
w	Width	mm
w_{sr}	Width including surface roughness	mm
$w_{as-printed}$	Width as-printed	mm
w_{end}	Width outer parts tensile coupon	mm
w_{middle}	Width middle part tensile coupon	mm

Greek symbols

Symbol	Description	Unit
α_R	Reliability factor	-
β	Reliability index	-
γ	Design factor	-
γ_2	Material factor	-
δ	Deformation	mm
ΔL	Change in length	mm
Δt	Difference in thickness	mm
ε	Strain	-
ε_y	Strain at yield point	-
ε_u	Strain at ultimate strength	-
ζ	Δt as a function of t_{avg}	-
η	Process efficiency	%
θ	Angle	°
λ	Wavelength of electromagnetic radiation	nm
μ_x	Mean	
ν	Frequency of electromagnetic radiation	Hz
ξ	End distance e_3 as a function of fracture line length L_f	-
ρ	Density	kg/m^3
ρ_{fl}	Density water	kg/m^3
σ	Stress	N/mm^2
σ_x	Standard deviation	
τ_u	Shear stress	N/mm^2

List of Figures

List of Tables

1 Introduction

In this chapter the background and the relevance of this research subject are discussed. Then, the main objectives (section 1.2) and the main research question together with the sub questions (section 1.3), that are necessary to get an answer on the main research question, are shown.

1.1. Background and Relevance

This research is part of the master's degree Structural Engineering of the Civil Engineering faculty at Delft University of Technology. The construction industry is considered by some as a slightly conservative sector. As the whole world is becoming more digital, this sector has a challenge in this field. One of the parts of digitisation is automation, which can be applied in different environments in the sector, as can be seen in figure 1.1. McKinsey has investigated the potential for Information Technology (IT) in the construction industry. As can be seen in the figure, almost half of this sector in the United States can be automated on a higher level. This trend will lead to more innovations in the building industry, as 3D printing for example. The possibilities with this new technique are endless and have a potential to become leading in the field of the manufacturing of free form structural parts. Not only the technique is developing, the applications around it are evolving too. In this research only parts of the technique and its possibilities can be highlighted. The future is a convergence of technologies, linked to other technologies; there is not one dominating technology. In the digital world, everything is linked easily, so a strong bond is created and innovations can get a boost.

3D printing, a synonym for Additive Manufacturing (AM), is growing extensively the last 30 years [59]. It has been a famous topic for a few decades, but mostly in the production of plastics. Now the construction industry starts to print in 3D; in concrete [36], in steel [37], [62], [61], [58] and even in fibre reinforced polymers[22]. The development of 3D printing of steel is evolving rapidly; the free form and rapid on site construction are two of multiple advantages. The printing of steel can be seen as welding by a robot arm with a welding head that rotates and moves around multiple axes. The term Additive Manufacturing is more precise than 3D printing, as layer upon layer is deposited to build up the object. The conventional way of the production of such a specimen would be to mill a solid block, so a large amount of material would be thrown away [55]. Another advantage of 3D printing; material can be saved, which means that the fabrication process is more sustainable.

The next step in the research on 3D printed materials in the construction industry, and 3D printed steel in particularly, can be taken. A whole bridge was printed in stainless steel (type ER308LSi), by MX3D in 2018 [37], as can be seen in figure 1.2. However, the use of printed steel in constructions in the near future will be in the smaller items, in the connections for example. With the current technologies and its developments, it is more expensive to print steel than to use a rolled member, which has the same dimensions. When 3D printing will become a more standardised way of constructing, the price of 3D printing will drop. Connections are expensive parts of a construction due to their complexity and therefore it pays off to optimise and print a connection. Combining 3D printing with topology optimisation (TO) is therefore a good idea. This research project concerns a fundamental research

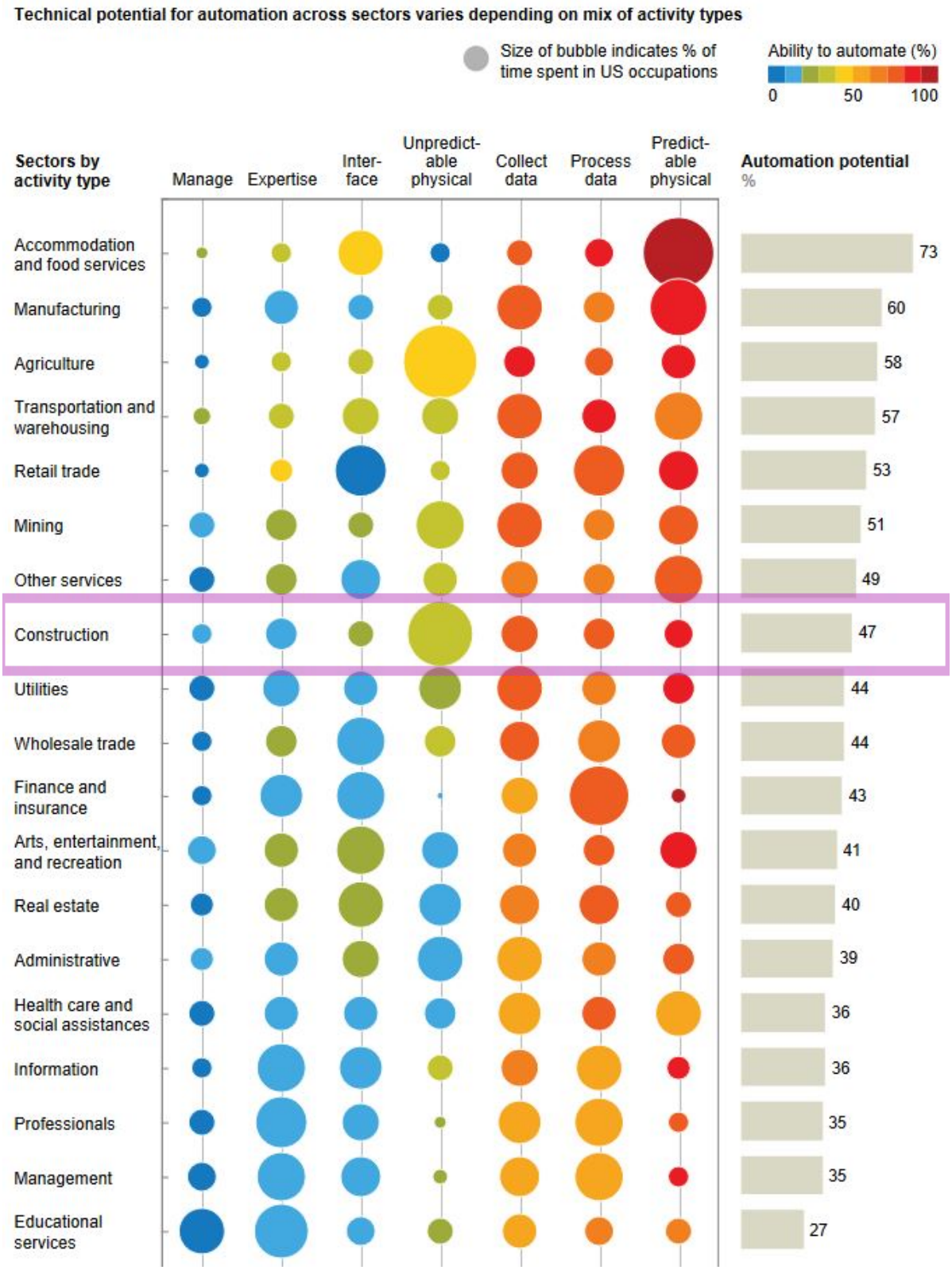

Figure 1.1: Automation potential in construction sector in the US [43]

Figure 1.2: MX3D stainless steel printed bridge [3]

focussed on the strength of a 3D printed steel connection. The strength of 3D printed material has to be known before 3D printed nodes or steel members can be designed.

In 2017 a ship's propeller was made by RAMLAB and Damen by means of 3D printing, instead of the conventional way of casting the steel [12]. It only took seven months to develop and days to print the object, which is quite fast for this new technique. One of the reasons for this short amount of time was that the total cooling time of all the small printed layers is shorter than the total cooling of a casted member, which will stay hot on the inside for a long time. The properties of printed material are better than the properties of cast steel, when the volume is big, due to the cooling process, as segregation occurs during the solidification of the steel. This also causes impurities in the core, because the core will cool down the slowest.
The strength of the steel is lower when the cooling process is slow [39]. This propeller is certified and in use. In figure 1.3 the propeller can be seen together with the printing robot.

The material costs of carbon steel are lower than the costs of stainless steel and therefore carbon steel is used most often in the construction industry. This, together with the advantages of 3D printing as free forming with layer by layer build up, material savings and lightweight structures, is a reason to do research on the properties of 3D printed carbon steel.

Until present, 3D printed stainless steel is produced more often, because of its corrosion resistance and high aesthetic features. However, carbon steel that is conventionally produced, is used more often, because it is cheaper than other steel alloys. The strength of these 3D printed carbon connections is probably as high as stainless, as this is also the case for rolled steel, but it is worthwhile doing research on carbon steel to find the best properties of this type of steel when printed. In this way the designs of nodes can be optimised in material deposition and for their purpose, to resist a certain type of applied loads, specifically.

One of the Additive Manufacturing (AM) methods is Wire and Arc AM (WAAM). This technique is faster than powder based AM techniques, such as Direct metal laser sintering (DMLS), as more material is added in a smaller amount of time. For the automotive industry small, very precise parts are indispensable, so a steel powder based printing method is used for the 3D printing of these automotive parts. For the construction industry parts with lower resolution suffices. Therefore, the technique that is used for this research is WAAM. In section 2.1 more is explained about the different AM technologies.

Wire and arc additive manufacturing of steel will always be combined with other production or adaptation techniques. Two of them are described here. The first logical production method that can be combined with 3D printing is machining, to have an even more optimised form of the 3D printed

Figure 1.3: Propeller made by RAMLAB and Damen [12]

node. Drilling a bolt hole is much more precise than printing a bolt hole. When drilling, a smooth bolt hole surface is produced, which is advantageous for the spread of the forces. The forces will be applied on the bolt and thereby on the bolt hole surface. Contrary to printing a hole for a bolted connection, when the bolt hole surface would be irregular and rough. Another example of machining is when milling a surface. After printing, every side of the specimen is irregeular, due to the weld bead roughness. When really smooth surfaces are needed, Computer numerical control (CNC) milling with sanding is a solution.

The second production method that is a favourable combination with 3D printing is in the software sector and concerns the optimisation of the topology. Size optimisation and shape optimisation are different from topology optimisation, as Verbart et al. [65] stated. When the size is optimised, the geometry is changed, such as the length and diameter for example. When optimising the shape, a more round shape can be made out of a rectangular form. When the topology is optimised, the material is redistributed, so the shape and the size are not fixed. The result will be a totally optimised design of an object, depending on the forces that act on the node.

An example of an optimised node is the tensegrity node, designed by Arup [32]. In figure 1.4 the development of this node by topology optimisation can be seen. The node was made by Direct Metal Laser Sintering (DMLS), another Additive Manufacturing (AM) technique than WAAM. More on DMLS can be found in section 2.1. The WAAM method combined with topology optimisation is investigated by the Technical University of Darmstadt [42]. Instead of using stiffeners made of rolled plates in an H-beam, an optimised geometry can be used, as can be seen in figure 1.5a. On the left the conventional way of producing stiffeners is shown and on the right the topology optimised stiffener. The same holds for two beams that are connected with plates, so a T-stub is created. Instead of using a connecting plate, the bolts can be connected to the beam by a wire and arc additively manufactured and topology optimised geometry, as can be seen in 1.5b.

Structures that are demountable are becoming more popular, due to the sustainability value; when demounting a structure, the different parts can be reused. This is an important reason to investigate a bolted connection.

Another connection that consists of a plate with a bolt hole in it is when a cable has to be attached to a column or beam. A brace or a stay holds a membrane structure, for example, just as the Olympic

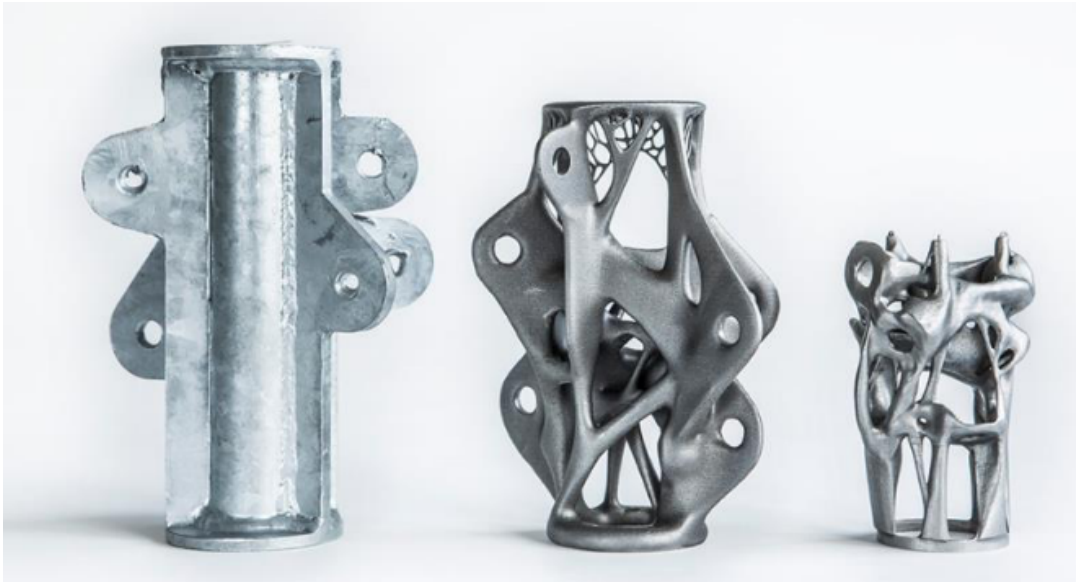

Figure 1.4: Development of the Tensegrity node of ARUP [32]

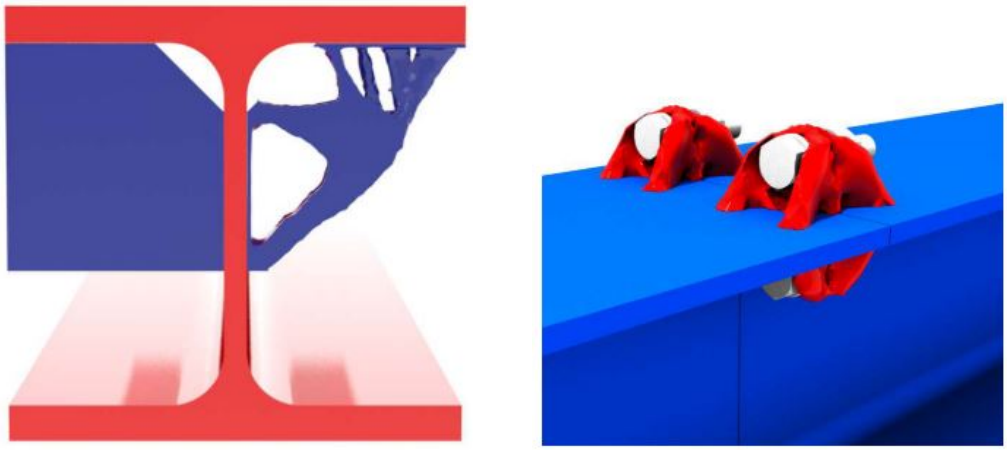

(a) Stiffeners in H-beam

(b) Topology optimised T-stub

Figure 1.5: Topology optimisation combined with WAAM [42]

stadium in Munich, a construction where a lot of tensile forces have to be resisted to hold the roof over the stadium. Such a node can be seen in figure 1.6. A reason to print this node is when more flexibility is wanted in designing. One knows that the ties should be connected with each other in this node, but what the node will look like exactly can be decided later on. The node can be printed on site, when the exact forces on the node are known. This could lead to a change in the design of structures.

A second reason to print these nodes is that material can be saved, by combining the 3D printing with topology optimisation, which is more economical and environmentally friendly. A free form can be designed and then printed by a flexible robot, that is multiple employable, just by changing the printing parameters and the kind of steel for example. Even the welding head can be replaced by another tool. The easiest, cheapest and fastest application is when the surface of the node does not have to be milled, but if the surface can stay as-printed. In section 2.4.3 and 3.3 more is explained on this matter.

The node that can been seen in figure 1.7 is a WAAM node produced by Autodesk. The customer made some specifications for the functions of the node. One of these was to have a custom-made node with a perfect fit. When building, some connections have low tolerances for fitting, so it would be effective to have a design that can be adapted. In this way the changes can be implemented on site and an updated node can be printed. Due to optimisation, the weight of nodes can be smaller and they can be installed more easily. In this way no extra parts have to printed, which would lead

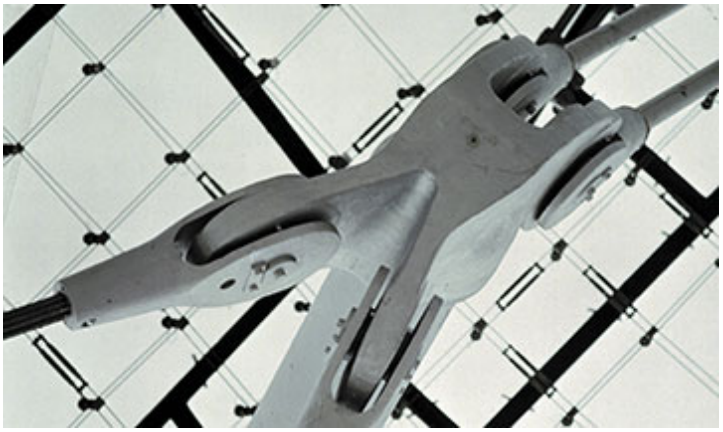

Figure 1.6: Node Olympic Stadium Munich [4]

Figure 1.7: Node for braces in front of facade [66]

to waste of material when they are thrown away. In this sense, the technique results in more flexible and sustainable design solutions. A consequence of saving material is that the structure has a lower self-weight, so a lighter total structure can be designed, which will save more material again and thereby saves costs. The costs will not only be saved by using less material, but also by having lighter structures and thus less transport costs.

The second suggestion of the customer was that different structural components can be fabricated in one single part, so a complex node can be made, that does not consist of small parts, all connected to the large basis component. The strength will increase when the whole connection is one component, as Heat Affected Zones (HAZ), initiated by the welding in the base material, are weak under a cyclic loading [67]. This node in figure 1.7 is connected by rods and cables.

An interesting other case is the Shaded Dome, that can be seen in figure 1.8, designed by Shaded Dome technologies, a collaboration of the companies Zwarts & Jansma architecten, Royal HaskoningDHV and Poly-Ned. This dome consists of a tent dome that is held by ties. Some details that are shown in 1.9 represent steel plates with bolted connections. This node can be used as case study, as there are lips with a thickness of 10 mm with a bolt hole of 18 mm diameter, as can be seen in figure 1.9a. The triangle shown in figure 1.9b is also a plate of 10 mm thickness, but with M20 bolts. Cables are tied to these bolts. A failure of the steel plate may occur, such as tear-out failure for example, when the bolt is torn out of the steel plate when the force is parallel to the plate.

Due to all the developments in the printing of steel, there is enough reason to further investigate the properties of WAAM carbon steel.

Figure 1.8: Shaded Dome Groesbeek [52]

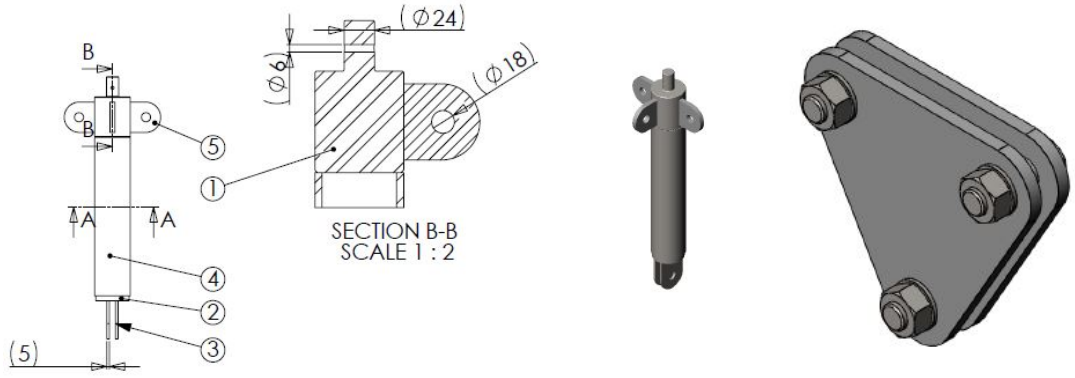

(a) Tie

(b) Assembly of ties

Figure 1.9: Details Shaded Dome

1.2. Main objectives

With the background and relevance discussed in the last section 1.1, the objectives can be stated. The main objective of this fundamental research is to determine the strength of a Wire and Arc Additively Manufactured (WAAM) carbon steel and to determine design values for WAAM connections in the current building industry. To attain this, the following steps have to be taken:

1. By performing a literature research, the current situation of 3D printing of steel in the building industry is represented and the necessity of this innovation is exposed.

2. The strength of a wire and arc additively manufactured carbon steel plate is analysed, by means of laboratory tests on the tensile and tear-out strength of a single bolt hole.

3. With the analysis of the results of the tensile tests, design values for WAAM carbon steel can be determined. With the analysis of the tear-out tests, an exploration of bolted connections on WAAM carbon steel plates is made.

1.3. Research questions

With the main objectives in mind, as stated in 1.2, the following research questions can be defined. The main research question is:

'What are the design rules that need to be determined to assess the tear-out strength of a bolt or pin in a wire and arc additively manufactured carbon steel plate?'

To be able to answer this main research question, the following sub questions are formulated:

- What are the mechanical properties, such as the yield and ultimate tensile strength, Young's modulus and ductility of a wire and arc additively manufactured carbon steel plate?
- How is the anisotropy, caused by the weld direction, affecting the mechanical properties of wire and arc additively manufactured carbon steel plates?
- Are the mechanical properties of the wire and arc additively manufactured carbon steel compliant to the existing standards, such as the Eurocode; NEN-EN 1993-1-8?
- How can the tear-out of pinned connections be compared to bolted connections in wire and arc additively manufactured carbon steel plates?
- To what extent can the tear-out strength of a wire and arc additively manufactured carbon steel connection of a plate with a single bolt hole be compared to a rolled carbon steel member?
- How can the tear-out strength of wire and arc additively manufactured bolted connections be translated into design values?

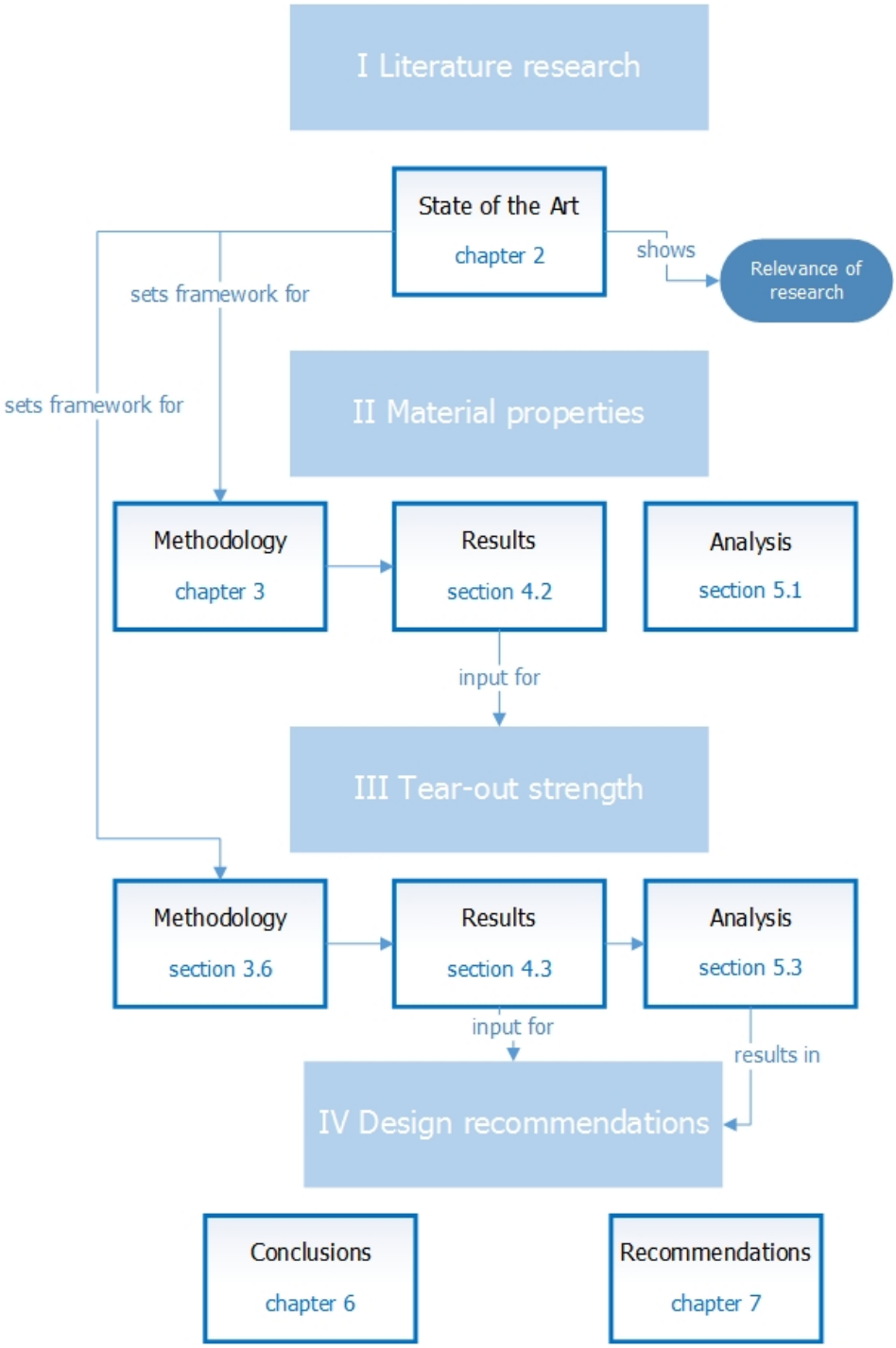

Figure 1.10: Thesis outline

1

2

State-of-the-Art

More and more is known about Additive Manufacturing (AM), mostly of polymers, but gradually also more on metals and concrete. Not only the printing process of steel develops, but also the printing software and therefore the outcome, so the printing quality of the manufactured object improves. These developments are advantageous for the construction industry as more freedom of form and design is possible, next to the positive fact that less material can be used, due to optimised designs where material is only put in the spots where it is needed. This also results in structures that are light-weight. Due to experiments with structural elements in laboratories and finite element models, even more is known about the behaviour of the material properties of additively manufactured parts.

The advantages of 3D printing will be discussed in 2.1. One of the additive manufacturing (AM) techniques that is suitable for large-scale production is WAAM, which will be discussed thereafter, in 2.2. Then the printed material is discussed, which is carbon steel, section 2.3. And in the last section, 2.5, the current developments of the research on the tear-out strength are highlighted.

2.1. Additive Manufacturing

There are several materials that can be used for Additive Manufacturing (AM), either for the powder or the wire methods, that are described in this section. A summation of these metals and some of their advantages and disadvantages can be seen here, after which the focus will stay on carbon steel, as this material is used for this research.

- Carbon steel: This is the cheapest and most widely used material in the construction industry. More can be read on this material in sections 2.3 and 3.1.2.
- Stainless steel: The first researches on WAAM are done on stainless steel, so a lot of knowledge is gained in this field. Stainless is corrosion resistant, hence its name, and has a higher ductility than carbon and is 1,5 times more expensive. There are several types of stainless steels, based on their crystalline structure.
- Aluminium alloy: This metal has a high strength-to-weight ratio and has a low stiffness, compared to the other metals named here.
- Titanium alloy: This is one of the strongest and most expensive metals and therefore one of the most applied metals for AM of medical, aerospace and automotive parts for example. It is corrosion resistant.

The most published research on 3D printing of steels is about stainless steels. Joosten, as well as van Bolderen and Tebbens have conducted research on printed stainless steel; they took the additively manufactured bridge of MX3D as an inspiration for their graduation work. These reports will be of great value for this follow-up study on AM of steel.

Currently there are different additive manufacturing (AM) technologies. There are two main methods; the first is based on powder and the second on wire. A scheme of these technologies can be seen in figure 2.1. There are two types of powder processes; powder bed and powder fed. Powder

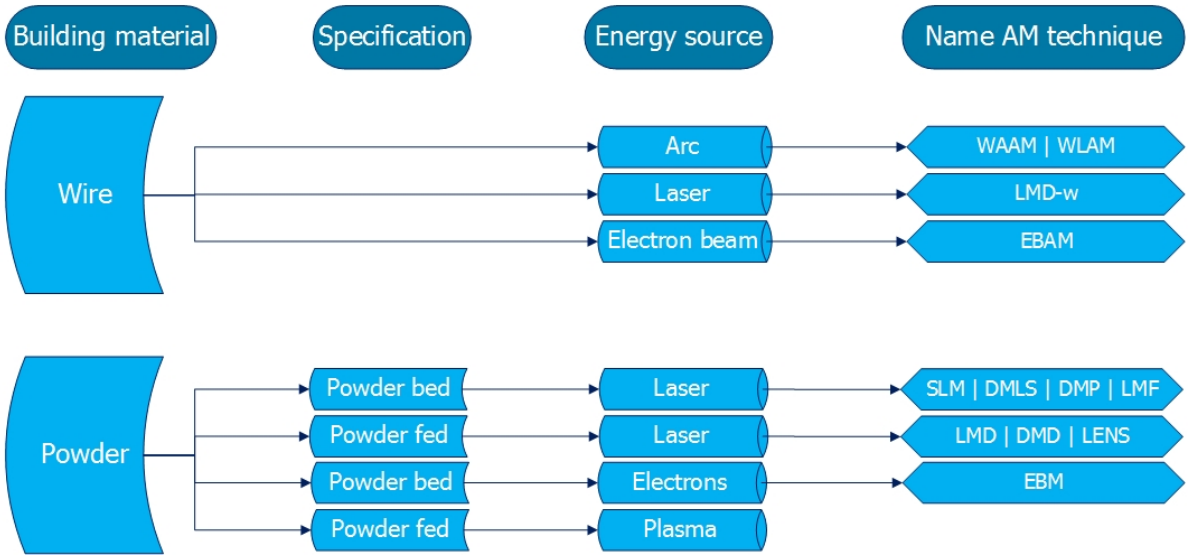

Figure 2.1: Scheme of AM technologies; wire and powder based. Picture based on [21].

fed is comparable to the wire fed processes, due to the fact that the material is added via a nozzle. There are laser and plasma powder fed processes, as can be seen in figure 2.1. The laser powder fed processes are Laser Metal Deposition (LMD), Direct Metal Deposition (DMD) and Laser Engineered Net Shaping (LENS) [21].

In the powder bed process a large amount of extra powder of the material, the metal in this case, is needed and a part of the powder that is stacked will melt into the desired form. An electron or a laser beam can be used to melt the metal particles into a product. One of the laser powder bed processes is called Direct Metal Laser Sintering (DMLS) [24] and is used a lot in the automotive and aerospace industry. Other laser powder bed processes are Selective Laser Melting (SLM), Direct Metal Printing (DMP) and Laser Metal Fusion (LMF) [21].

The process of making a powder out of the metal is labour-intensive and expensive. A cheaper option is to use a metal wire, as in wire and arc additive manufacturing (WAAM). Another advantage of WAAM above powder fed processes is that the porosity is less [27], so a more homogeneous material is created with WAAM.

Next to the WAAM technique there is Wire Laser Additive Manufacturing (WLAM), where the metal wire melts due to the laser. The third technique is by electron beam and is called Electron Beam Additive Manufacturing (EBAM), this is the same as Electron Beam Melting (EBM), but instead of metal in a powder bed in a vacuum room, a wire is used.

The advantages of printing steel, according to the Steel Detailers' Manual, is the increase in adaptability, which will lead to flexibility in planning and the possibility of upgrading bridges. This can be seen in table 2.1 [35].

Another advantage of printing is the small amount of material that is used, which causes a low weight of the structure or structural parts, which means lighter foundations and thereby a smaller amount of material is used again, as was the starting point of this reasoning also. The next advantage of AM is that material waste can be reduced when no mould is needed [29]. When replacing the casting by an AM process for nodes for instance, the latter is more economical. Most of the time large amounts of repetitive building details, such as nodes, are needed to reduce the costs. When additive manufacturing, this mass customisation is not necessary; unique nodes can be produced, without increasing the costs extensively.

In the production of a component of a structure, storage of certain parts can become redundant. For example when printing the connection part of façade elements just in time; just before they are needed on site, storage of those parts and the investments for tools is no longer applicable [56]. This saves room for storage and thereby reduces costs. The 3D printing robots themselves have been an investment, but only once. After the purchase, the break-even point is reached fast. For AM it is not the production process that determines the design, but it is the other way around [55].

Table 2.1: Table with advantages of 3D printing; 1, 2, 6 and 9 [35]

Feature	Leading to	Advantage	
		in buildings	in bridges
1. Speed of construction	Quick erection to full height of self supporting skeleton	Can be occupied sooner	Less disruption to public
2. Adaptability	Future extension	Flexible planning for future	Ability to upgrade for heavier loads
3. Low construction depth	Reduced height of structure	Cheaper heating Reduced environmental effect	Cheaper earthworks Slender appearance
4. Long spans	Fewer columns	Flexible occupancy	Cheaper foundations
5. Permanent slab formwork	Falsework eliminated	Finishes start sooner	Less disruption to public
6. Low weight of structure	Fewer piles and size of foundations Typical 50% weight reduction over concrete	Cheaper foundations and site costs	
7. Prefabrication in workshop	Quality control in good conditions avoiding sites affected by weather	More reliable product Fewer specialist site operatives needed	
8. Predictable maintenance costs	Commuted maintenance costs can be calculated. If repainting is made easy by good design, no other maintenance is necessary	Total life cost known Choice of colour	
9. Lightweight units for erection	Erection by smaller cranes	Reduced site costs	
10. Options for site joint locations	Easy to form assemblies from small components taken to remote sites	Flexible construction planning	

Summary state-of-the-art AM

There are two main types of Additive Manufacturing (AM) technologies for metals, one is with powder and the other is with wire. The subcategories of those two methods are all pointed out. The method used in this research is based on a low carbon steel wire that melts due to an arc, therefore this process is called Wire and Arc Additive Manufacturing (WAAM).

2.2. Wire and Arc Additive Manufacturing

The technology that is used for this research is WAAM, due to the high deposition rate. The following three WAAM methods are available [70].

1. Gas Metal Arc Welding (GMAW)
2. Gas Tungsten Arc Welding (GTAW)
3. Plasma Arc Welding (PAW)

The reason to use GMAW is that the deposition rate (in $kg/hour$) is high, even two-to-three times higher than GTAW and PAW processes. This is advantageous when larger products have to be created, as is the case for connections of structures. So, this method is used in this research. GTAW, which is also called TIG (Tungsten Inert Gas) welding, is mostly used for joints of thin objects. An extra wire is added, that melts due to the non-consumable tungsten electrode and the arc. Another application of GTAW is for the repair of fillet welds; to prolong the fatigue life [57]. PAW is known for its delivery of a high energy concentration on a small area [60]. For GTAW and PAW a tungsten electrode is used that is not consumed. In the GMAW process the wire electrode is consumed. Different methods of transferring this metal are known: short arc, globular, spray arc and pulsed arc transfer [57].

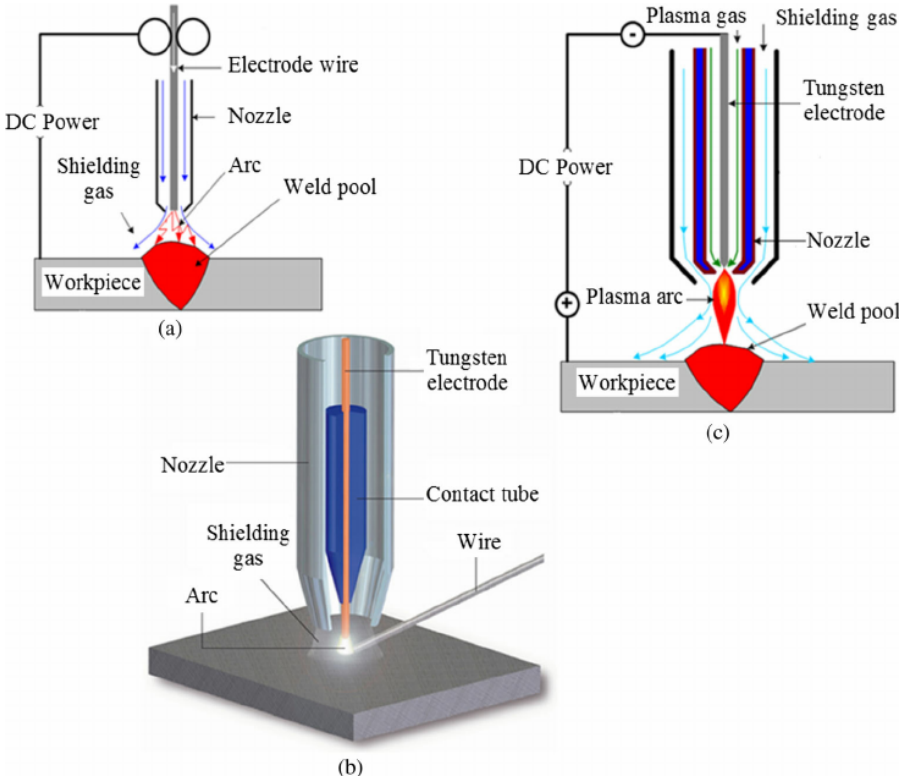

Figure 2.2: Schematic drawings of the processes **(a)** GMAW, **(b)** GTAW and **(c)** PAW [27]

2.2.1. WAAM advantages

According to Attaran [18] there are five key advantages of AM over the traditional way of manufacturing, namely:

- Speed
- Cost
- Quality
- Innovation or transformation
- Impact

For the construction industry WAAM is a good method, as a lot of steel can be deposited in a relatively short time period. This is advantageous, because when constructing a bridge for example, the production of material and therefore the erection of the structure is fast.

Another advantage of wire additive manufacturing is that up to 100% of all the material that is used for the printing process will be deposited, which is not the case when the material is added as a powder [27]. To work with powder metals is dangerous for the operators, that is why the metal parts are fabricated in a closed box in the machine. This box is one of the reasons why the size of the metal components that can be made is limited. The material costs of the powder made of the metal are higher than the costs for the metal wire.

The use of WAAM is more sustainable than the other Additive Manufacturing techniques, such as Electron Beam Melting (EBM) and Direct Metal Laser Sintering (DMLS), as is explained by Bekker [19]. In figure 2.3a the costs of the three techniques can be seen.

A big advantage is design freedom; any form can be made. This will lead to a wide variety in products, because one can make adjustments in the design easily. [21]

Material saving by AM is another advantage; by eliminating material at certain spots, where it is not needed for structural integrity or for the actions due to loading, a lighter object is created. This will also lead to a lighter structure and support structure, which causes a more sustainable product.

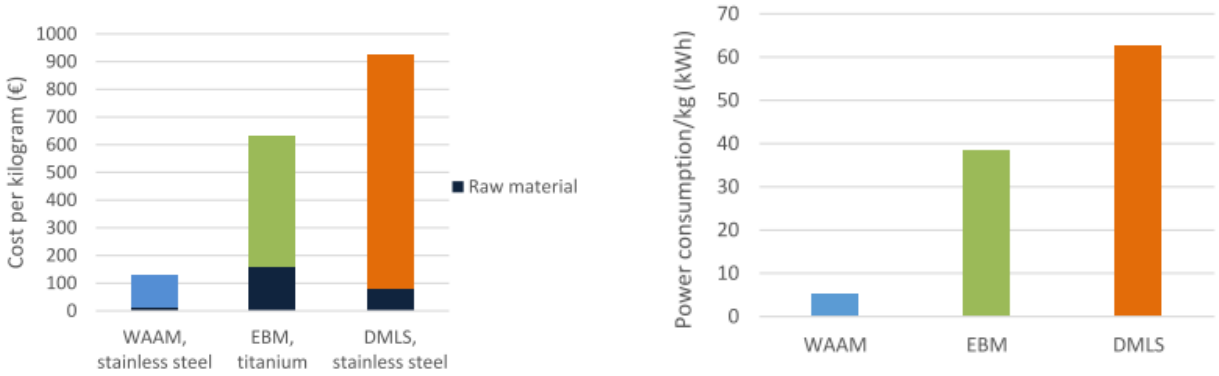

(a) Costs

(b) Powerconsumption

Figure 2.3: Comparison sustainability Additive Manufacturing [19]

Less steps in the design process are needed, because less parts need to be produced; a one-piece product, like a connection, can be made with AM. Assembling is eliminated, which introduces a very efficient fabrication process.

2.2.2. WAAM disadvantages

One of the disadvantages of wire and arc additive manufacturing is that the produced specimen is rough; an irregular, wavy surface is created, which means that the material has inaccuracies. This is due to the size of the steel components for fabrication, that is larger than powder-based material components, so the deposition rate must be higher. The surface roughness depends on the printing parameters [26], this is discussed in 2.4.3. Post-processing of these fabricated objects are common, to remove the irregularities.

Another disadvantage is the oxidation that appears on the surface when welding. This layer has to be removed in order to let the shining surface appear.

The third disadvantage is that the welding cannot take place in an open space, as shielding gases are needed to protect the weld. Wind on the construction site for example might be a risk for the weld quality, hence strict precautions should be taken when printing on-site, so the printing can take place in a controlled environment.

Even the quickest printing techniques are not that fast to make objects, as the conventional way of producing steel is quicker, but the techniques are improving and the printing velocities will still increase. WAAM steel has many advantages (as can be read in 2.2.1) that cannot be guaranteed when producing steel conventionally. Although this printing speed is a big disadvantage, it outweighs the advantages.

Not only knowledge about the machine and the process is needed for the AM technology in general, but also about the new design codes and possibilities. Investment is needed in people and time to realise this. Only a few companies need a printer, that others can use too, by sending an order to the printing company. This business model can be made profitable, despite the large investments that are made, if the machine is used multiple times [21]; then it is even cheaper than the costs of a printing robot and welding head, let alone a whole steel factory with all the operation processes.

WAAM steel can be seen as a "new" material. The wire material is well known, but the fabrication process for the objects with an accumulation of the wire material is new. Little is known about the material properties of such an object, which means that there are no guidelines for the quality control or validation of the printing, let alone for designing structures or connections. This is the reason to do research on this topic, as there are many things to discover in this area.

Summary state-of-the-art WAAM

Three methods of WAAM exist. In this research Gas Metal Arc Welding (GMAW) is used, due to its high deposition rate, which is advantageous for larger objects, such as parts of structures. A disadvantage of WAAM is the irregular surface that is created. A second disadvantage, which can be regarded as a research opportunity, is the little knowledge on the material and its behaviour, so there are no guidelines to follow for the design steps or production of AM objects. This knowledge gap will be partially filled by this research.

2.3. Material: low carbon steel

To decide what kind of steel to perform this research on, the relevancy of this investigation is determined. This is discussed in section 1.1. In this chapter the advantages and disadvantages of carbon steel are discussed.

Carbon steel is inexpensive, compared to other steels, such as stainless, that is why rolled members of carbon steel are used more in the construction industry. A lower resolution of steel suffices in the building industry, next to the fact that large volumes of material are needed and that there is none or only a small profit margin, so low costs are very important. Carbon steels with a low carbon content (up to 0.30% carbon) are typically used for structural applications [57], due to the high ductility of this alloy. That is why medium- and high-carbon steels are left out of the scope of this research.

When the steel has a very low carbon content (up to 0.13%), its weldability is good, especially when the manganese content is more than 0.30% and internal porosity is prevented. For WAAM a low carbon wire is needed, which is cheaper than wires of other steels. The prices are following the steel market value. Stainless steel wire Inertfil 308L is €2.90 per kg, while carbon steel wire Carbofil 1A is €1.90 per kg [1].

Despite the aforementioned advantages (section 2.2.1) and disadvantages (section 2.2.2), little is known on wire and arc additively manufactured **low carbon steel**. This is a reason to take the first steps in this direction; to determine the material properties, such as the strength.

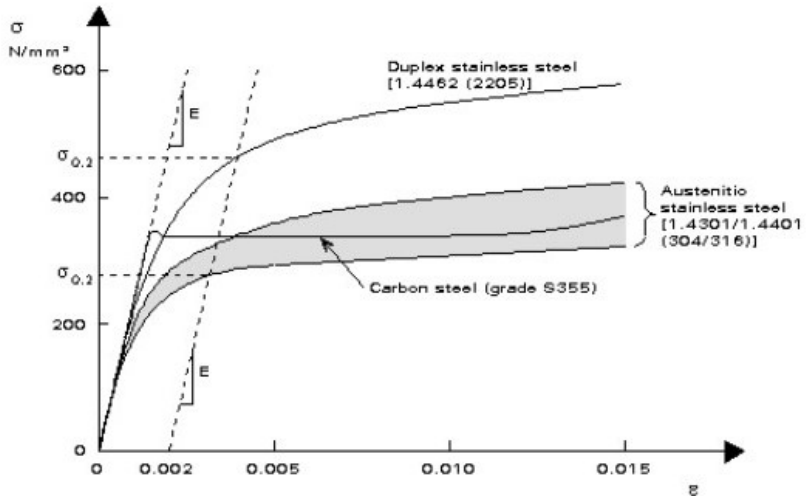

Figure 2.4: Stress-strain curves carbon and stainless steel [14]

2.3.1. Carbon steel material properties

The material properties of rolled carbon steel are well known. In figure 2.4 a stress-strain diagram of different types of steel can be seen. The carbon steel curve is clearly distinguishable, as the linear elastic part and the yield plateau are well-defined.

[1] According to the current steel prices from MX3D at the time of writing; January 2020

There are several grades carbon steel, the one shown in the graph is S355. The number indicates the **yield strength** in MPa. From the value of 460 MPa, so S460, this group of steels are called 'high strength'. After yielding, the steel starts to deform plastically. The strength at failure is called **ultimate tensile strength**. More on the results, such as stress-strain diagrams and how they are produced can be read in chapter 4.

Stainless steel shows a stress-strain curve that does not exist of linear parts, but it is more curved.

2.3.2. Influence of microstructure on strength of low carbon steel

When welding two steel plates, to connect them, a single or multi-pass weld is used. When using WAAM, the welding is different; hundreds of weld beads are placed on top of each other, instead of just one weld or tens of welds (for multi-pass welding).

When we have a look at the yield and ultimate strength of the WAAM object and compare these values to the material properties of the weld material, the strength values of the weld are higher than of an object made of multiple beads. This can be explained by zooming in to the microstructure of the WAAM low carbon steel.

The carbon content of the used steel is very low; 0.06%, as can be seen in A. The lower the carbon content (wt% C), as is displayed on the lower x-axis of figure 2.5, the lower the yield and tensile strength, displayed on the left y-axis. The relation between the two is shown by the red and green curves.

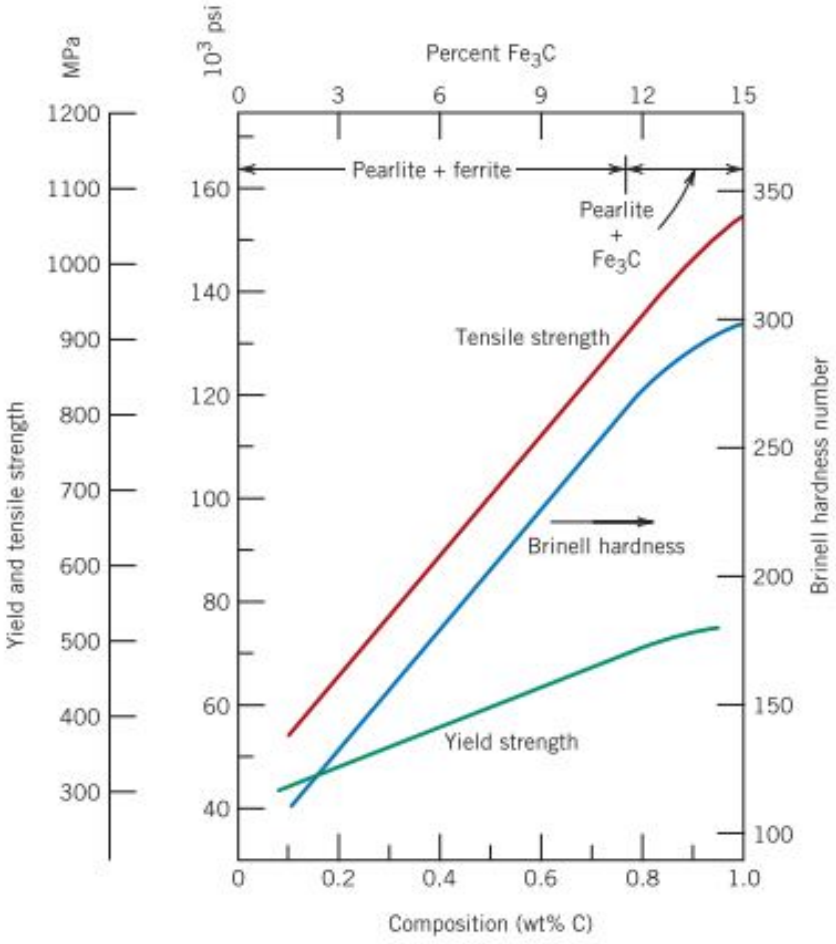

Figure 2.5: Relation between carbon content, strength and hardness [23]

The strength of a steel is determined on a microstructural level by the ability of plastic deformations to appear. They are formed by atoms that slip. When a material deforms plastically, a large amount of dislocations moves. This is called "slip", as can be seen in figure 2.7. The planes along which the slip occurs are at an angle of 45 degrees compared to the direction of the applied force, the tensile axis.

This is namely where the least stress is needed for the material to deform. For slip two main objects are of influence:

- Dislocations
- Grain size and boundaries

Dislocations are defects in the arrangement of atoms, in the crystal lattice. In figure 2.6 an edge dislocation is displayed, which can be regarded as an extra atomic plane in the lattice. Dislocations have a size of around 10 to 100 nm [23]. When a shear stress is applied to such an arrangement of atoms the number of bonds that should be broken to move the dislocation by one atomic distance is small compared with a perfect lattice structure.

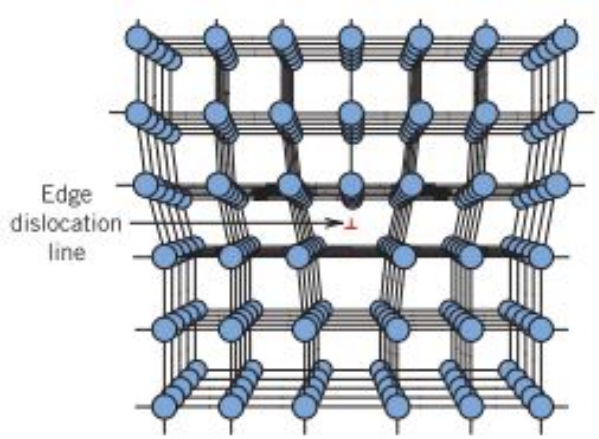

Figure 2.6: Dislocation in the crystal lattice [23]

The strength of a material can be increased when the mobility of dislocations is reduced. This can be achieved by:

I Alloying a material by replacing Fe-atoms by substitutional atoms with a difference in size. This creates a stress field in the lattice reducing the mobility of dislocations.

II Increasing the dislocation density. The movement of a dislocation is delayed by the presence of other differently orientated dislocations. An increase in dislocation density takes place when the material is strain hardened.

III Introducing precipitates that hinder the movement of a dislocation (called precipitation hardening).

IV Grain boundaries (figure 2.7). The dislocation should continue its path in a different direction in the adjacent grain. The finer the grain size the stronger the material.

The last item is the most important for this study. Firstly, the grain size is strongly affected by the heat introduced during welding. At high temperatures grain growth will occur. The mobility of the atoms is high at higher temperatures, whereas the system aims to obtain the lowest possible energy level. This can be achieved by reducing the interface energy by lowering the amount of grain boundaries. This can be seen in the coarse heat affected zone (HAZ), next to the fusion line of the weld.

Secondly, the grain size is also affected by solid state transformations taking place during heating and cooling. Initiation of nuclei of the new phase during the transformation has a grain refining and thus a strengthening effect. A fine grained heat affected zone can be found in the region near the weld where the temperature just exceeded 900 ℃ when a low carbon steel with 0.06 wt% C is used [23], as in this study.

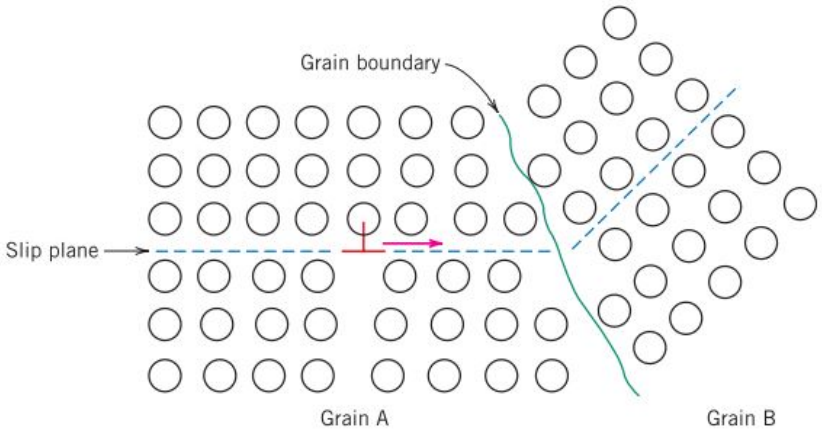

Figure 2.7: Grain boundary and slip by a dislocation [23]

The production process of WAAM low carbon steel can be considered as a heat treatment, such as annealing; with every weld bead the temperature of the object is elevated. The cooling rate of the material determines the microstructure that is formed. A Continuous Cooling Transformation (CCT) diagram of a low carbon steel shows the formation of microstructures, as can be seen in figure 2.8. The temperature is indicated on the y-axis and the time on the x-axis. When the material is cooled very fast, martensite is formed; a very hard and brittle microstructure. When the cooling is done more gradually, pearlite and ferrite are created. In the material used in this study the carbon level is very low, which makes martensite formation unlikely.

2.3.3. Corrosion

Carbon steel structures are susceptible to corrosion, especially in an environment where the humidity or salinity is high. Carbon steel has very little resistance against corrosion, in contrast to stainless steel. The surface of carbon steel looks the same to the naked eye as stainless steel, until the corrosion starts. Therefore, carbon steel might need a coating, such as protective paint. When it concerns protecting steel structures, it is common to apply a primer first, then the paint and afterwards a top coat. Most civil engineering structures are made of carbon steel, including the Golden Gate bridge, that has to be painted with a protective coating every year.

Galvanised (zinc) coating is an option too. It has a more constant thickness than applied paint, is more scratch-resistant and has a more complete protection, which all ensures better corrosion resistance. The only two disadvantages of galvanising are the high costs and the predefined colour; silver.

Conductive polymers can be also applied as protective layer [51]. Another possibility is to remove the rusty layer; after the first corrosion layer, the corroding slows down [74]. The attachment of the protective layer to the steel has to be good. When the steel is printed, a layer of slag appears, this originates from the coating of electrodes or welding wires, also called flux. This coating melts, together with the core wire, as can be seen in 2.9. The slag floats to the surface of the weld, because the metal is heavier than the slag.

The slag contains deoxidation products that originate by reactions of the oxides, air and the flux. Next to that, the slag protects the weld, when it is still molten, from gases and other impurities in the atmosphere. [7], [72]. It is better to remove this layer before applying a protection layer on the steel. Corrosion on the surface of the carbon steel will have a small, negligible, influence on the strength of the material. The influence of corrosion and the protection against it are outside the scope of this project, as it is most likely that a protective coating will be applied on the WAAM connection or on the structure as a whole.

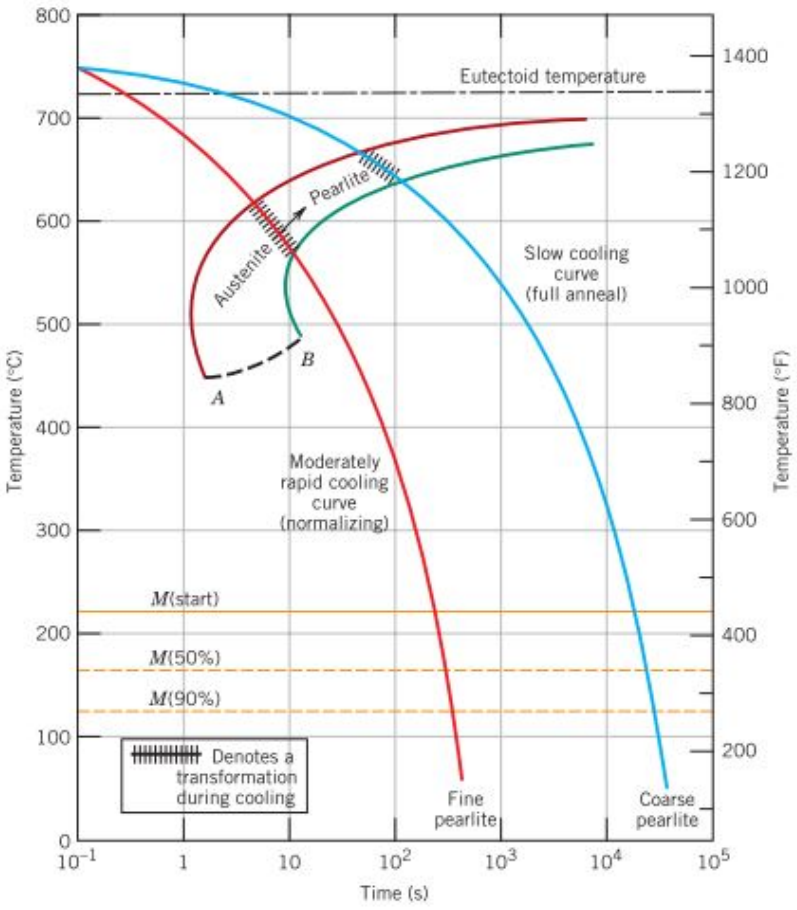

Figure 2.8: Continuous Cooling Transformation diagram [23]

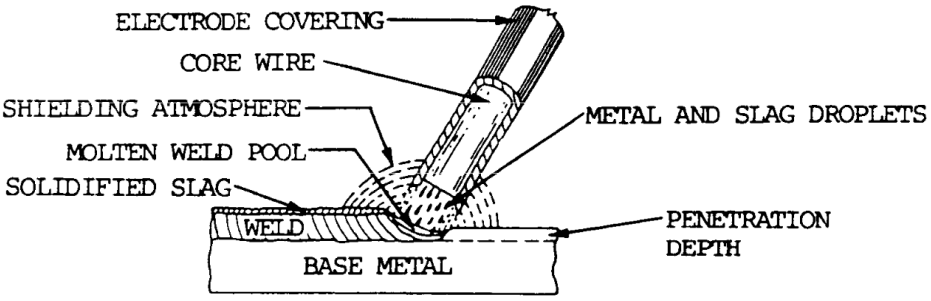

Figure 2.9: Shielded Metal Arc Welding [7]

2.3.4. Fatigue

In general steel connections are prone to fatigue. Fatigue is caused by cyclic loads on a structure that appear due to wind, seismic or traffic loads.

The fatigue strength is influenced by four parameters mainly [64]:

I Material

II Stress concentrations, due to geometric discontinuities

III Local stresses, due to the weld shape and dimensions

IV Local defects of the weld

When bolts are preloaded, the fatigue resistance is increased. In this study non-preloaded bolts are used, because the bearing strength of the 3D printed steel plate is determined [47] and not the resistance of the bolts. Fatigue resistance is most important in the case of bolts in tension [64]. That is the first reason why this subject is left outside the scope of this research. The other reason is that outside this research, another investigation on the fatigue behaviour of WAAM stainless steel is conducted at present.

Summary state-of-the-art materials

The material that is chosen for this research is low carbon steel, due to the low costs and the regular use in steel structures. The microstructure has an influence on the strength of steel; the larger the amount of dislocations and the number of grain boundaries, the higher the strength. Corrosion and fatigue resistance are disregarded in this research.

2.4. Factors that influence the printing process

During the printing of carbon steel some features have to be taken into account, such as the printing parameters, that influence the printed result. Next to that, the geometry difficulty, surface roughness and active cooling are discussed in this section.

2.4.1. Printing parameters

When printing steel and in this case a wall of steel, the settings of the printing robot have to be such that the desired specimen, with the right dimensions, is created. The variables that are of interest and that have an influence on the appearance of the specimen and on the microstructure are mentioned below. This is of great importance for the outcome of the material properties. No values of these printing process parameters are stated, because this is confidential information of MX3D, the WAAM company [3].

Welding heat input

The welding heat input is determined by the voltage (U), current (I), travel speed (v_{travel}) and process efficiency (η), as can be seen in equation 2.1 [25]. The process efficiency for GMAW is in the range of 60 to 90%. The bigger the heat input (in kJ/mm), the lower the cooling rate, the more ductile, which means a lower hardness, but the weaker (in tensile and yield strength) the material is. The elongation ε will increase when the ductility is increased.

$$Heat\ input = \eta \frac{U\ I}{v_{travel}} \tag{2.1}$$

Arc voltage

When the arc voltage U (in V, W/A, J/C or $kg\ m^2/s^3/A$) is increased, the heat input is higher and the penetration depth is increased, as well as the bead width.

Table 2.2: Cooling rate ranges for various fabrication processes [61]

Fabrication Process	**Cooling Rate [K/s]**
Directional Solidification	10^{-1} to 10^{1}
Casting	10^{0} to 10^{2}
Arc Welding	10^{1} to 10^{3}
Electron-Beam Welding	10^{2} to 10^{4}
Laser-Beam Welding	10^{2} to 10^{6}
Single-laser Pulse	10^{7} to 10^{8}

Current
The welding current I (in A or C/s) affects the heat input. The nozzle-to-bead distance is also of influence. To control the welding current, one has to adjust the wire-feed speed.

Wire speed
The amount of wire that is used in a certain time period is called the wire speed (in m/min). The higher the wire speed, the smaller the deposition rate, the penetration depth and the smaller the height of deposited layer.

Printing speed
The speed that the robot arm has to print the steel layer is called printing speed, travel speed (v_{travel}), the welding pulse time or arc speed. The unit is mm/min. 'The welding pulse time is the period the machine prints or welds at a single spot and can be related to the welding speed parameter in ordinary GMAW processes.', as Joosten stated. The higher the speed, the faster the cooling of the specimen is, because less heat is used per unit length for the additive manufacturing process.

Deposition rate
The deposition rate shows (in $kg/hour$) how much steel is deposited on the layer of steel, the bead, that was made just before. This determines, together with the printing speed, the height of the deposited layer.

Wire diameter
The wire diameter is around 1 mm. The thicker the wire, the more heat is needed to let the wire melt so it can be deposited.

Nozzle angle combined with specimen angle
The nozzle angle (in °) is assumed the same as the wire angle and this combined with the specimen angle is called the printing angle. The angle determines the cooling rate a bit and thereby the grain direction, but this effect is minimal. The cooling rate has a larger influence on the grain direction, which influences the strength [37]. The penetration depth is also affected by the printing angle.

Preheat temperature
The specimen can be preheated before the next bead is applied on the specimen. This will influence the strength of the specimen, as the cooling rate is reduced, when preheated.

Cooling rate
The **interpass temperature** is the temperature of the printed object before the next weld bead (pass) can be applied. This has to do the cooling rate (in $℃/s$), which depends on the welding heat input and the amount of layers that is made. Then one knows how long it takes before the heat of the object is transferred via the base plate via radiation.

Radiation
Heat is a form of electromagnetic radiation with a specific wave length range. The velocity of the radiation c is determined by the wave length λ (in nm) and the frequency ν (in Hz), according to equation 2.2.

$$c = \lambda \, \nu \tag{2.2}$$

2.4.2. Production of geometries

In some cases, when producing a certain object, the robot has difficult angles to make, due to the complicated geometry of the specimen that is produced. Angles are hard to make, harder than a cylindrical shape, as a non-smooth turn has to be made by the robot. The more angular the turns are, the more heat is accumulated. The robot has 6 degrees of freedom, but a more precise and more homogeneous print is made, when a degree of freedom is controlled by a second mechanism or robot, as is used for the propeller in figure 1.3. The printer settings have an influence on the shape of the printed object and the other way around; this has to be aligned.

In this research the hole in the WAAM plate for the double lap joint is drilled instead of printed, so a smooth hole surface is created. This is advantageous for the distribution of the forces that are applied on the bolt or pin. Thus, a combination of 3D printing with CNC milling might become more prevalent.

2.4.3. Surface roughness

The properties of the specimen are influenced by the printing parameters. One of the properties that has consequences for the geometry of the specimen is the surface roughness, measured in mm. "Surface texture is the repetitive or random deviation from the nominal surface that forms the three-dimensional topography of the surface." According to Bhushan [20]. He also states that the surface texture can include the following four items:

- roughness (nano- and micro-)
- waviness (macroroughness)
- lay
- flaws

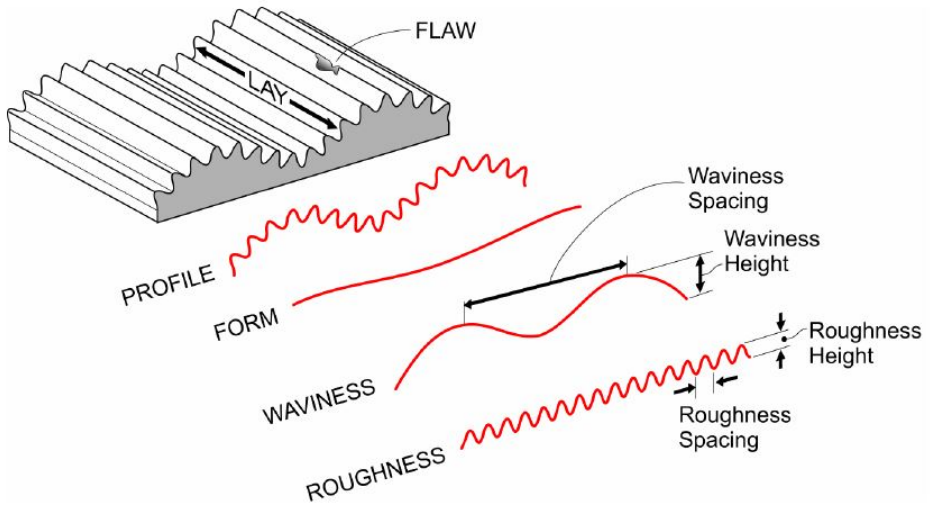

Figure 2.10: Surface texture [13]

With the drawing in figure 2.10 the meaning of those four terms is explained. The first two of this list are of interest for this research. Waviness is present on a larger scale than roughness. The latter includes the local highs and lows that are larger than the size of the molecules. In this case we can see the maxima and minima of the WAAM low carbon steel easily by the naked eye.

Xiong [71] stated that the interlayer temperature, the wire feed speed and the travel speed have a significant influence on the surface roughness of thin-walled parts. The surface roughness can be decreased when the inter-layer temperature is decreased and also when the wire feed speed is decreased. To improve the surface quality even further, the travel speed can be increased, but no more than 0.4 m/min. At this speed the arc becomes unstable.

Another factor that has an influence on the surface roughness is the wire-feed-speed-travel-speed-ratio (WFS/TS); the lower the wire feed speed (WFS) and therefore the lower the ratio, the lower the

surface roughness is. In practice a larger travel speed will be used, around 2 m/min, as a large amount of material has to be printed, especially for this research.

In general, it can be seen that the thicker the single pass welds are, the more wavy the printed wall is, as more material has to be deposited, so the wire feed speed must be decreased and/or the travel speed increased.

The WAAM technique is evolving, so the quality of the printed parts is getting better, because more is tested and investigated. This will also lead to specimens with less irregularities and a smoother surface.

The surface roughness is of importance when the effective thickness is determined, as in this research (more on this can be read in section 4.1), or when the milled surface is wanted, for aesthetic reasons for instance.

2.4.4. Active cooling

When using active cooling or a heat treatment, the material and therefore the mechanical properties of the steel will change. This is done to improve the material, when the hardness has to be increased for example.

Regarding the microstructure during active cooling; the grains of the steel will be finer and they will be directed in the same direction when the heat input is low [69].

There are several ways of cooling; with liquids or gases, the types of these gases can differ. The easiest is to use air under pressure. Next to that there are different moments in the building process to cool or to heat, namely; in-situ, interlayer and post build [25].

An advantage of active cooling during the production process is that the stopping time of the welding robot can be reduced. The robot has to be stopped until the last weld has cooled down enough, before the new weld can be applied on top [61]. This means that the printing process is more efficient and more material can be deposited in a shorter amount of time, so the production level can be raised. From an economical point of view this is interesting.

In this research continuous printing is used as process with a predefined interpass temperature and other printing parameters, as can be read in section 2.4.1. This affects the cooling of the object while printing.

The active cooling equipment is not well-evolved at present, as the temperature can not be regulated well enough, so this post-welding treatment is left out of the scope of this project.

Summary state-of-the-art printing

A list of printing process parameters that influences the properties of the printed object is mentioned in this section. Furthermore, the difficulty of the object geometry determines the quality of printing, such as the surface roughness for example. In general; the more heat is put into the material, the more irregular the surface of the steel becomes. Post-welding treatment, such as active cooling, can be applied on the object, while printed, to improve the mechanical properties. In this research, no active cooling is applied.

2.5. Tear-out strength

There are different literature sources where information on failure modes of single bolted and pinned connections in steel plates can be found, so a well-considered decision can be made on how the tear-out test should be performed. Firstly, the European standard, the Eurocode [10] is well-known as one of the guidelines to follow, although the design calculations are known as being very conservative. The Eurocode and other standards are studied in 2.5.1.

Other researches are done on the tear-out failure of rolled steel plates, this is discussed in 2.5.2. Due to the conservativeness of the Eurocode, experiments are conducted at the TU Delft, to come up with more realistic design rules, discussed in 2.5.3.

The next section, 2.5.3, the failure mode splitting is described. In 2.5.5 more information is given on pinned connections.

There are two types of elements that may fail in a connection of a steel plate with a bolt hole; the bolt or the plate. There are different modes of failure for the plate; net cross-section failure [54], bearing

failure and shear failure [47], [38]. When the net section, so the distance $2e_2 - d_0$, as can be seen in figure 2.11a and 2.13, is insufficient, the plate will fail in this net section area. When the distance (e_1) is governing instead of (e_2), bearing and shear failure (also called tear-out) are the options. It is hard to distinguish the two, as they come together most of the time. As Kim and Yura stated; the strength of a bolted connection is determined by the end tear-out first, which then goes over into bearing failure [40]. Tear-out happens when the end distance e_1 is insufficient. The tear-out strength depends on the shear resistance of the planes, the blue failure lines, in figure 2.11b and blue surfaces in figure 2.13. Bearing failure is when the hole of the bolt will deform and steel plate material will be accumulated, figure 2.11c.

As opinions are divided on how to call the failure mode of tearing a bolt or pin out of a plate in transversal direction, it is decided that in this study the combined failure of bearing and shearing is called tear-out from now on.

The bearing strength of rolled low carbon steel can be compared to rolled stainless steel. This comparison can also be made for the different kinds of printed steel with the weld direction parallel, perpendicular and diagonal to the applied force.

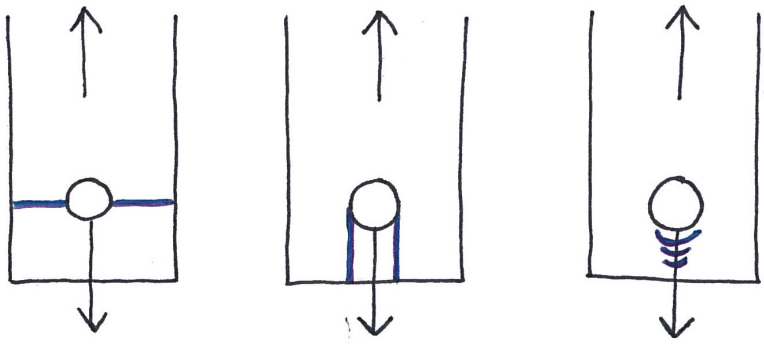

(a) Net section failure (b) Shear failure (c) Bearing failure

Figure 2.11: Failure modes of the plate with a bolt hole

The tear-out strength is influenced by the geometry of the specimen: the thickness (t), width (w), length of the plate, but also the size of the bolt hole, the end distance (e_1) of the hole and the edge distance (e_2). This can be seen in figure 2.13. To ensure that the mode of failure will be tear-out, the other failure modes must be avoided. When using a very strong bolt, that is definitely stronger than the plate, failure of the bolt is prevented. A second reason to prevent bolt failure is that this failure is brittle and ductile failure modes are desirable, due to the warning it gives before failure. The second failure mode that needs to be prohibited is net cross-section failure. This mode is avoided, when the entire resistance of the connection is attained [68]. This is why research is done on tear-out of the bolt.

There are no studies on the tear-out failure of WAAM plates, in any material. In the following subsections different models for this failure mode are discussed; all of them are for rolled steel.

2.5.1. Codes

There are different guidelines that can be followed for the construction of bolted connections:

- European; Eurocode (EC)
- British Standard (BS 5950)
- American Institute of Steel Construction (AISC)

Kamtekar [38] did a study “On the bearing strength of bolts in clearance holes” in 2012, where these three codes are compared with each other, theory and experimental results. This research is on carbon steel. In table 2.3 it can be seen that the edge distance varies from $1.20d_0$ to $2.67d_0$. Wherein d_0 is the diameter of the bolt hole, which is 1 or 2 mm bigger than the bolt itself, depending on the size of the bolt.

The European standard on the design of steel structures, Eurocode 3, has a part on connections; part 1-8. The design rules on bolted and pinned connections can be found here.

Another type of connection is a tie. This tie is attached by a bolt or pin to a plate and is then loaded with a tensile force, as in figure 1.6. In the case of this research subject, the plate, that is connected to the pin or bolt is 3D printed. In chapter 1, section 1.1, the relevance to study this connection is explained.

Bolted connections

In steel and timber structures, bolted connections of steel are used to connect elements as beams and columns to each other. The bolts consist of a hexagonal head and a circular shank. In this case the shank is only partly threaded, as can be seen in figure 2.12. On the thread a nut is attached. Between the bolt head and the steel plate a washer is placed, as well as between the nut and the plate, to distribute the forces that are applied on the bolt.

Figure 2.12: M16 bolt and pin

No research is done on the tear-out strength of 3D printed carbon plates. The only researches on this subject are on rolled steel plates, on carbon and on stainless steel, as well as on high strength steels [30], [38], [40].

The design rules in the Eurocode are supported by hundreds of experimental test results that were carried out during the last century [45]. To estimate the capacity of the tear-out strength of the WAAM plate, the equations in the Eurocode 1993 part 1-8 are used. The dimensions of the plate are also determined by these equations, as the desired failure mode is tear-out, where the shear force is governing. When bolts and pins are considered, the partial factor for a material property $\gamma_{M2} = 1.25$ is taken, that is also for uncertainties in models or variations in dimension. When the shearing plane does not take place through the thread of the bolt, $\alpha_v = 0.6$. When considering bearing strength, which is part of the tear-out strength as well, equation 2.3 is taken. The values herein for k_1 and α_b can be seen in equations 2.4 and 2.5.

$$F_{b,Rd} = \frac{k_1 \, \alpha_b \, f_u \, d \, t}{\gamma_{M2}} \tag{2.3}$$

$$k_1 = smallest\ value\ of \begin{Bmatrix} 2.8\, e_2/d_0 - 1.7;\ 1.4\, p_2/d_0 - 1.7;\ 2.5 \end{Bmatrix} \tag{2.4}$$

$$\alpha_b = smallest\ value\ of \begin{Bmatrix} \alpha_d = e_1/3\, d_0;\ f_{ub}/f_u;\ 1.0 \end{Bmatrix} \tag{2.5}$$

Pinned connections and comparison with bolted

Another connection for steel and timber plates is a pin. A pin is a simple version of a bolt, as can be seen in figure 2.12; it has no thread and no head, neither has it a nut or washers for the attachment.

Movement in the direction parallel to the pin is not restrained. Only shear, movement perpendicular to the length of the pin, is resisted.

Standard NEN-EN 1993-1-8 [9] part 3.13 includes guidelines for the calculation of pinned connections. The calculations and design of pins are the same as for bolts, when rotation is not considered and when the pin is three times smaller than the pin diameter. The steps can be seen in part 3.6.1. Otherwise, part 3.13.2 can be followed.

The only forces that can be transferred by a pin are shear forces. In this connection tear-out and bearing are the failure modes that are accepted, so only shear is accounted for [34].

Some of the plates where pins are put through, are thickened around the hole to create a higher strength pinned connection. Local thickening of plates can be done easily by printing.

The only downside is that a smooth surface can only be fabricated when machining is done after printing. So, when a tight fit between the connected plates must be made, the manufacturing of the connection is labour-intensive.

2.5.2. Current models bolted connections

Kamtekar examined in 2012 the bearing resistance of bolts in clearance holes of carbon steel [38]. He stated that the calculation method in Eurocode 3 could be improved and proposed two approaches. The first one is simple and can be applied when the deformations during failure are of importance. The second one can be used when this is not the case. The first method results in even more conservative calculations for the end and edge distances of bolted plates than EC 3, but this method is easier to use, because only the diameter of the hole must be known. The assumption is made that the bolts are likely to have a higher strength than the plate, so bolt failure will not occur. For both approaches of Kamtekar the following two assumptions are made. First, failure at bearing takes place when the bearing stress f_b equals $2f_u$. Second, the shear out planes are formed in the direction of the force from the bolt holt to the end of the plate, as can be seen in figure 2.13.

Another research on single bolted connections of mild steel was conducted by Može and Beg in 2014 [46]. They stated that shear failure of the bolt hole will occur when e_1 (end distance) has a maximum value of $1,5d_0$. Another statement they made is that the net cross section is not only of influence on the net cross section failure mode, but also on the bearing. When the latter takes place, the steel in front of the bolt is pushed and piles up, causing a larger area of contact of the bolt in the bolt hole in the plate. The material is yielded and therefore the stress concentrations in the plate are neutralised.

Table 2.3: Overview codes, papers and end and edge distances

Code	**End distance** e_1	**Edge distance** e_2
BS5950	1.25d_0	1.25d_0
AISC	varies	2.67d_0
EC3	1.20d_0	1.20d_0
Kamtekar method 1	2.67d_0	1.50d_0
Kamtekar method 2	e_1' = e_1 - (d_0/2) cos(θ)	0.5(1.2e_1'+d_0)
Moze and Beg	1.5d_0	–

As Wang et al. stated in his paper where he did research on single bolt holes in High Strength Steels (HSS); the failure mode depends more on the geometry of the specimen than on the steel grade, when a bolt is applied that has the same or a higher strength than the bolted plates. The equations 2.3 (bearing force), 2.6 (shear force) and 2.7 (ultimate force net section) can be found in Eurocode 3 [48], [47]. The tear-out failure has to be the governing failure mode, equation 2.6, as the tear-out strength is tested in this research.

$$F_{v,Rd} = \frac{\alpha_v \, f_{ub} \, A}{\gamma_{M2}} \tag{2.6}$$

$$N_{u,Rd} = \frac{0,9 \, A_{net} \, f_u}{\gamma_{M2}} \tag{2.7}$$

The area (A) in this equation is the area of the shear planes, which is the thickness of the plate (t) times the length of shear plane, which runs from the hole to the end of the printed plate, as can be seen in figure 2.13. When equation 2.10 is applied on the tear-out of a single hole, the only component that is of influence, is the shear stress part (τ_u). The other stresses are zero. To calculate the force that the printed plate can resist, equation 2.11 can be perceived.

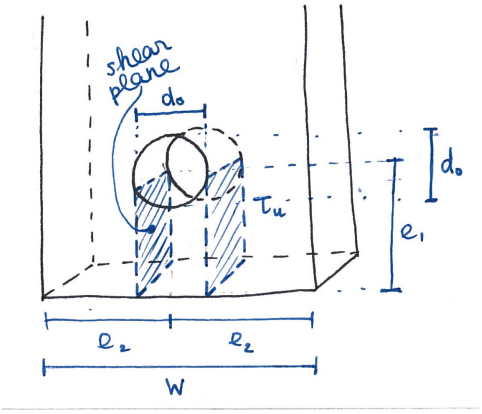

Figure 2.13: 3D printed plate with bolt hole. Shear surfaces of tear-out in blue.

2.5.3. Models for bearing

Tests are conducted at the TU Delft on rolled carbon steel plates with double bolt holes, in order to make less conservative design rules on the bearing failure mode of bolted connections. The new proposal for the bearing equation (2.8) is compared with the current equation (2.3). In the proposal equation k_1 is replaced by k_m and α_b for end bolts is three times higher than in equation 2.3, as can be seen in 2.9 [63]. The origin of this proposal comes from Snijder et al. in 1988.

The conclusions that are made after the analysis of these experiments is that the new proposed method for bearing is more realistic than the current method. e_2 is deleted from the equation, which has no influence on the bearing strength. The end distances should be taken into account; e_2 must stay the same, but e_1 can be downscaled. The material factor γ_{M2} can be downscaled too; the exact value must still be determined by further research.

$$F_{b,Rd,\,proposed} = \frac{k_m\,\alpha_b\,f_u\,d\,t}{\gamma_{M2}} \tag{2.8}$$

$$\alpha_{b,\,proposed} = min\left\{ e_1/d_0;\ 3f_{ub}/f_u;\ 3.0 \right. \tag{2.9}$$

$$f_u \geq \sqrt{\sigma^2 + 3\tau_u^2} \tag{2.10}$$

$$F_v = 2\,e_1\,t\,\tau_u \tag{2.11}$$

$$\tau_u = \frac{f_u}{\sqrt{3}} \tag{2.12}$$

Not only Snijder et al. stated that a change in the bearing model was necessary, also Može came up with amendments on the bearing resistance and capacity. He stated that the material factor $\gamma_{M2} = 1.25$ could be lower. And he proposed a simpler equation than 2.3, where a factor k_b is introduced instead of the two factors k_1 and α_b, as can be seen in 2.13. For equation 2.14 and 2.15 holds that $k_b \leq 5$. The proposed bearing resistance is based on the lower bound of the failures, which is the splitting failure.

Splitting means that the edge perpendicular to the loading direction, so the edge of the end distance e_1, will split in two. This happens due to high plastic deformation of this edge. A second deformation that takes place at this failure mode and that causes the splitting to develop even more, is the full

yielding of the net cross section. This distortion enables the longitudinal edges to rotate, so the corners will be pushed to the side. When the end distance is large, splitting failure is prohibited [45]. In this research the end distance is small, so splitting failure is an option.

$$F_{b,Rd,Moze} = \frac{k_b \, f_u \, d \, t}{\gamma_{M2}} \tag{2.13}$$

$$k_{b,end} = e_1/d_0 \tag{2.14}$$

$$k_{b,inner} = p_1/d_0 - 1/4 \tag{2.15}$$

2.5.4. End distance for tear-out failure

In conservative calculations an end distance e_1 is taken for the shear stress plane when tear-out failure occurs; so, planes tangential to the bolt hole are taken, as can be seen in figure 2.13. In reality the bolt does not act in this plane, as there is a hole clearance c between the bolt hole and the bolt itself, to have some tolerance when assembling the connection. It depends on the size of the bolt if c equals 1, 2 or 3 mm. For M16 bolts the hole clearance is 2 mm [8]. This results in a bolt hole d_0 dimension of 18 mm, as can be seen in equation 2.16.

$$d_0 = d + c \tag{2.16}$$

When the plate starts to shear, the shear fracture faces are parallel to the direction of the force, at the maxima of the bolt, where its projection is on the bolt hole. This is point A, as is shown in figure 2.14a. Kamtekar [38] defined a new end distance e_1', shown in equation 2.17 and 2.18. A more clarifying figure is shown (2.14) to derive these equations.

$$e_1' = e_1 - \frac{d_0}{2}\cos\theta \tag{2.17}$$

$$\theta = \sin^{-1}\frac{d}{d_0} \tag{2.18}$$

The most recent experiments on the tear-out strength of rolled carbon steel were performed at TU Delft, as can be read in the report of van Looveren [63]. Here, the same end distance e_1' was taken. This resulted in a maximum tear-out forces that were in line with the expectations, when equation 2.11 was regarded.

The same assumption for the tear-out strength as in equation 2.19 is made for the tear-out tests on WAAM low carbon steel. Here, the end distance is called e_3.

$$F_{max} = 2t_{eff} \, e_3 \, \frac{f_u}{\sqrt{3}} \tag{2.19}$$

2.5.5. Current models pinned connections

The reason to consider not only bolted, but also pinned connections for this research is that the test set-up for pinned connections suits the use of Digital Image Correlation (DIC) very well. A bigger hole can be made in the side plates to make the surface of the printed plate visible. Little is known on the behaviour of pinned connections, especially when comparing them to bolted ones for tear-out tests. So, to see if the results of both tests are comparable and therefore if the DIC results of the pinned connection are usable, both tests must be performed.

There are a few researches on pins in plates and the tear-out resistance. The tighter the hole around the pin, the higher the bearing stress will be. Duerr and Pincus designed a reduction factor C_r for the bearing stress when the hole diameter D_h divided by the diameter of the pin D_p is bigger than 1.0 [31].

$$\frac{D_h}{D_p} > 1.0 \tag{2.20}$$

In Eurocode 3 [48] the ultimate load P_u for plates loaded in tension has a factor α in numerator of the equation, which equals 2.5 for bolts and 1.5 for pins, due to the nut, that prevents the bearing failure [15].

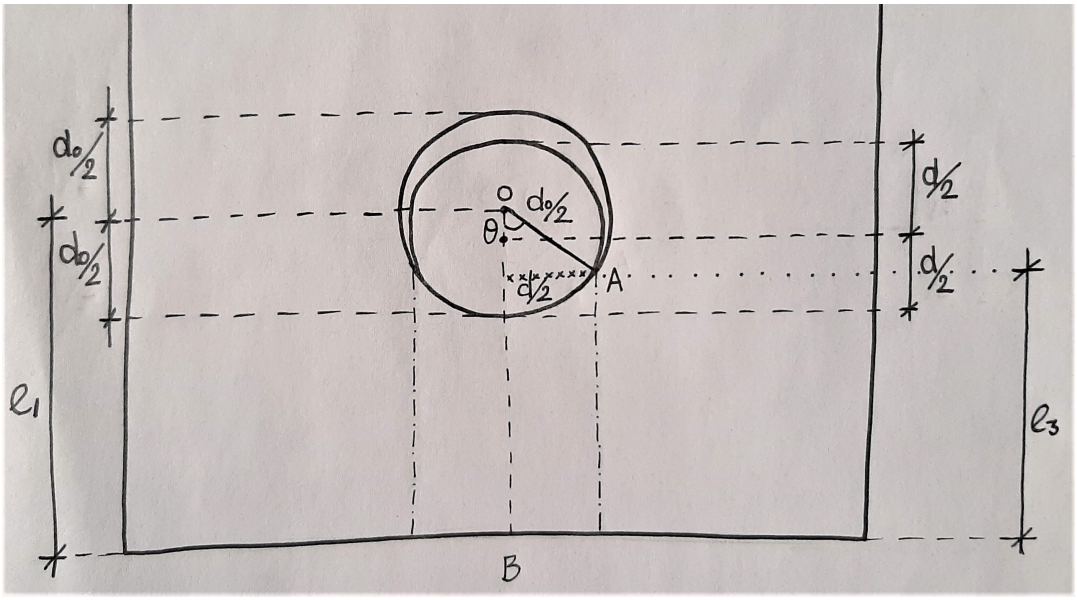

(a) Dimensions for end distance e_3, based on Kamtekar [38]

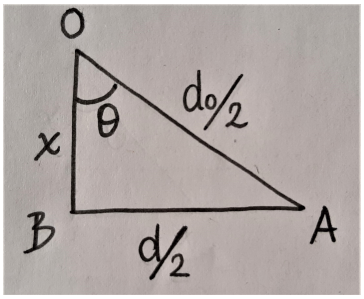

(b) Zoomed in on bolt d and bolt hole d_0

Figure 2.14: Derivation of end distance e_3

2.5.6. Numerical models of bearing strength in ABAQUS

Može and Beg conducted research on the bearing strength of single bolt holes by experimental tests and finite element analyses by numerical modelling in ABAQUS [46] [45]. The tests were performed on rolled steel. This guide of experiments and comparisons can be used to create the same model for WAAM steel, because no research had been done on WAAM objects in FEM until present. A similar model as in [46] is used for the numerical study of [45]. In [46] the force-displacement curves of both tests (experimental and numerical) are compared; they are matching well. Both shear and net cross section were the failure types in this study of S235 mild steel. The results are compared to high strength steel (HSS) S690, to see that mild steel (MS) has larger bearing deformation capacity. S235 failed in the shear plane instead of in the free edge. To test the reliability of the model, the maximum resistances of both tests are put in one graph and the correlation and regression coefficient are determined. Both numbers are near 1, so the obtained results of the model are reliable.

There is another Finite Element (FE) parametric study [33] on stainless steel of bolted connections, where the end distance for tear-out failure is $e_1 = 1,2d_0$ and the end distance for bearing failure is $e_1 = 3,0d_0$. d_0 is the size of the bolt hole. This means that there is a grey area for the failure modes for bolts; bearing and tear-out, when the end distance of the bolt hole varies.

In this research no FE model will be made, due to time constraints, so modelling will be outside the scope of this project. The DIC tear-out results of this study can be used as input for models of follow-up researches.

FEM with WAAM carbon steel

In the 21st century a lot of research is done in FEM. For WAAM steel no research has been done in FEM on tear-out tests. The difficulty in implementing a WAAM plate in a finite element model, is that

the properties of the material are not known. The starting point is to model a homogeneous model, although printed steel is an inhomogeneous material, next to the inclusions and the irregular surface the unmachined object has. The WAAM carbon steel is also orthotropic, as the mechanical properties differ when the material is tested in different directions; when the force is parallel, perpendicular and diagonal to the weld direction.

Another factor that determines the material properties is the printing process properties. The grains in the microstructure are formed in a certain direction, due to the cooling down of the material. This is of influence on the strength of the material.

The more developed the printing process is, the smoother and more confined the material. The same holds for the thickness of the printed steel; the thinner, the less heat was put into the steel object, the smoother the surface. Altogether, the material relies on so many uncertain factors, that is very difficult to print steel which has exactly the same material properties as the steel that is created before. When the printed steel is modelled in a finite element program, these properties must be known.

All the uncertainties that are named above and the fact that no research is done on WAAM steel in FEM have led to the decision not to include a finite element model in this research, although it would be valuable to validate the experimental outcome with the model.

Summary state-of-the-art tear-out strength

Several studies (Kamtekar and Može and Beg) concern the tear-out failure of bolted connections in rolled steel. On pinned connections little is known. For both connection types nothing is known on WAAM steel. Therefore, it will be valuable in the first place to see how WAAM low carbon steel behaves when a force is applied on it and secondly what the difference is between the two set-ups; bolted and pinned.

2

3

Research methodology

Tests are executed in the Stevin Laboratory of the department of Structural Engineering at the faculty of Civil Engineering at the University of Technology in Delft. In this chapter more will be explained on the production of the specimens and the test methodology. The tests are performed in order to give an answer on the posed research questions in section 1.3.

Before the tests in the laboratory can be performed, the carbon steel has to be printed, this can be read in section 3.1. Then the printed plates are cut (section 3.2) into the desired specimens needed for the tensile and the tear-out tests. A small part of the tensile test specimens is milled, as can be read in section 3.3. To determine the geometry and especially the thickness of the printed samples, different methods are used, as can be seen in section 3.4. In the sections that follow both test methodologies are described; the tensile test 3.5 and the tear-out test 3.6.

3.1. Preparation of specimens: printing

The wire and arc additively manufactured wall is produced as follows; on a base plate, also called substrate, the first welding bead is made. On top of this first bead the next welding bead will start and in this way two walls are built at the same time, that are connected by a cylindrical part, as is more extensively explained in the following paragraph. This is also called continuous printing. An anisotropic structure appears, partly due to the cooling conditions of the specimen [61]. The cooling is influenced by the travel speed of the robot and by how often the robot starts and stops. More about this can be read in section 2.4. The printing conditions are not mentioned, as this information must be kept confidential.

The walls are printed horizontally, so the built-up is vertically, and are made by MX3D in Amsterdam. MX3D develops the software for the WAAM robots. The maximum size the plates may have is around 400 mm in length and 300 mm in height. This is because of warping of the plate that may be caused by the heat input when the next welding bead is put on top of the wall. To prevent warping, two walls can be connected by half a cylinder, so the following hollow form, an object existing of two walls, is created. This is shown at figure 3.1. Two plates are extracted from this shape. In section 2.4.2 more can be read on the geometry and the difficulty to make certain geometries. The limit of the height and length of the plate are given due to printing experiences of MX3D.

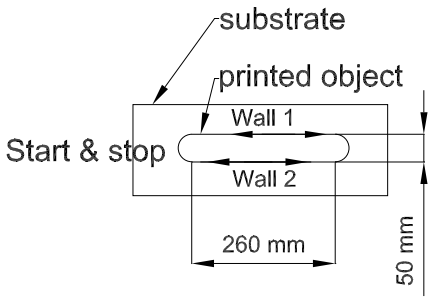

Figure 3.1: Topview printed double wall, connected by a cylindrical part

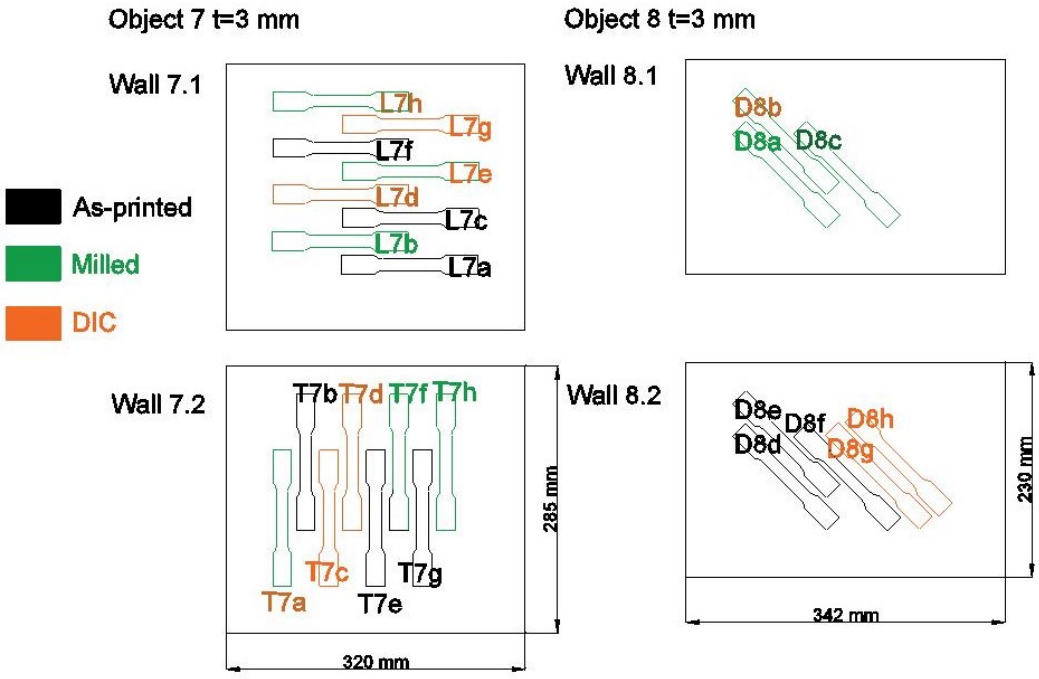

Figure 3.2: Tensile thin specimens (printing direction horizontally)

The final dimensions and number of walls are determined by the fitting of the samples. 60 tensile test samples were produced, of which 18 are milled. The size of the walls for the tensile test specimens can be seen in figure 3.2 and 3.3. The black and orange pieces are tested as-printed. The orange though are not only measured by an extensometer, as they all are, but also with Digital Image Correlation (DIC). More on this method can be read in 3.5.4. The green samples in this figure are the milled samples. More on the milling can be read in 3.3.

In figure 3.4 and 3.5 the tear-out samples in the walls can be seen. Like the tensile samples, the are cut in three different directions; transversally, longitudinally and diagonally compared to the direction of the weld beads. More on the choice of dimensions of the samples of the tensile and tear-out tests can be read in section 3.5 and 3.6 respectively. During the production of the steel geometrical imperfections may occur, such as surface roughness, an irregular cross section and out-of-straightness [41].

The higher the wall as described above, the more heat is put inside the wall, which means that the lower welding beads are reheated after they are welded more often than the upper beads. This heat input and cooling rate have an influence on the grain orientation and thereby on the strength of the printed steel. This also means that the location in the wall where the specimens are cut out, has an influence on the strength of the specimens. For these reasons, the bottom part, of about 35 mm, is not used for the production of the specimens. To be sure that the cut-out samples are as regular as they can be, without inclusions and irregularities in the microstructure as mentioned above, some space is also left to the side and upper parts.

3.1.1. Robot

The welding process for the fabrication of the samples is automated by a multi-axis robot with a Gas Metal Arc Welding (GMAW) head. In figure 3.7 the ABB robot of MX3D with a welding head can be seen in their workshop in Amsterdam, together with one of the objects. The combined nozzle-workpiece angle is 90 degrees.

The printing time of one object, consisting of two thick walls, was eight hours, excluding stops between the welds to let the object cool down. The deposition rate was 0.6 kg/h. The thin objects with an average wall thickness of 3 mm took also eight hours, but a smaller interpass time was needed. More material needs to be deposited when a thicker wall is created (deposition rate 1.2 kg/h), this results in a lower printing speed. Also, the cooling rate is lower, as more heat is put into the object. More on this can be read in section 2.4.1.

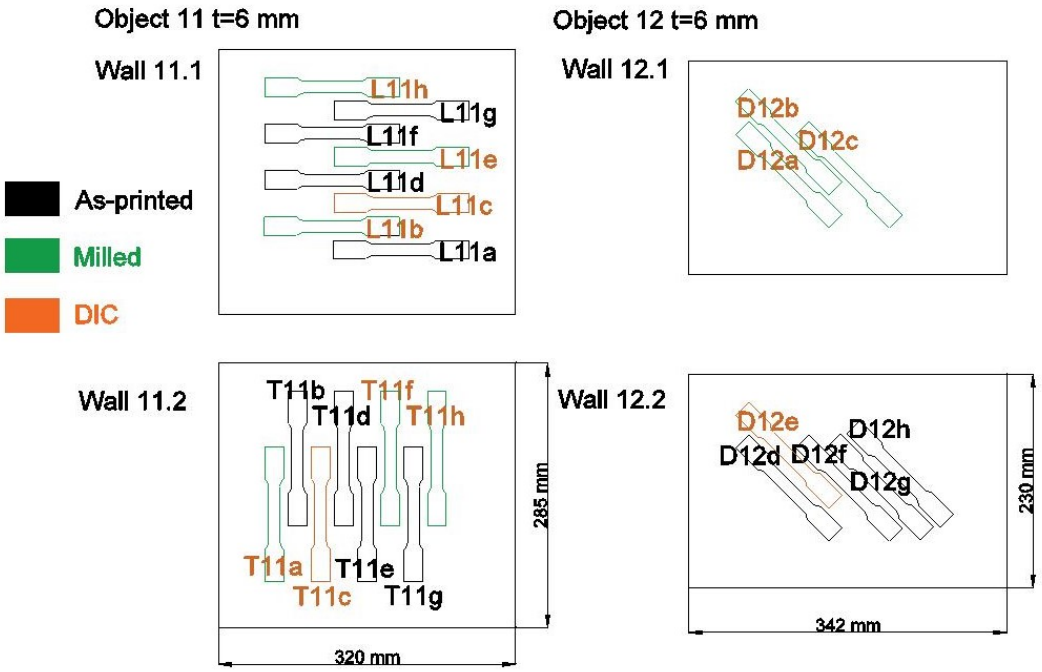

Figure 3.3: Tensile thick specimens (printing direction horizontally)

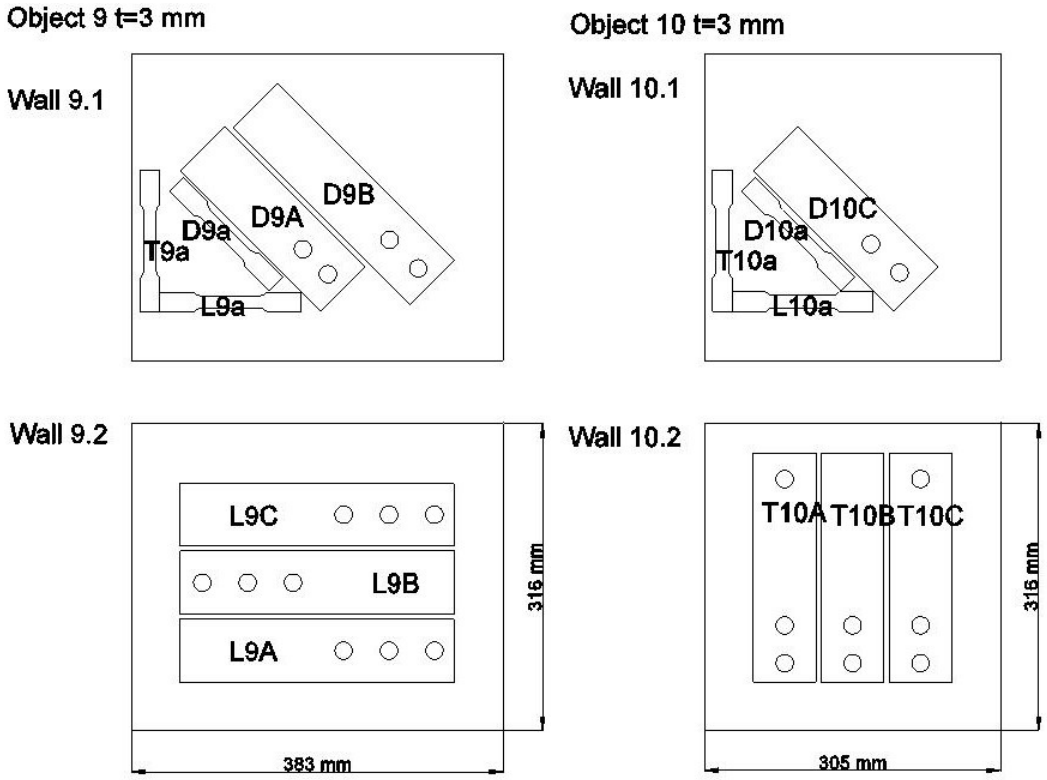

Figure 3.4: Tear-out thin specimens (printing direction horizontally)

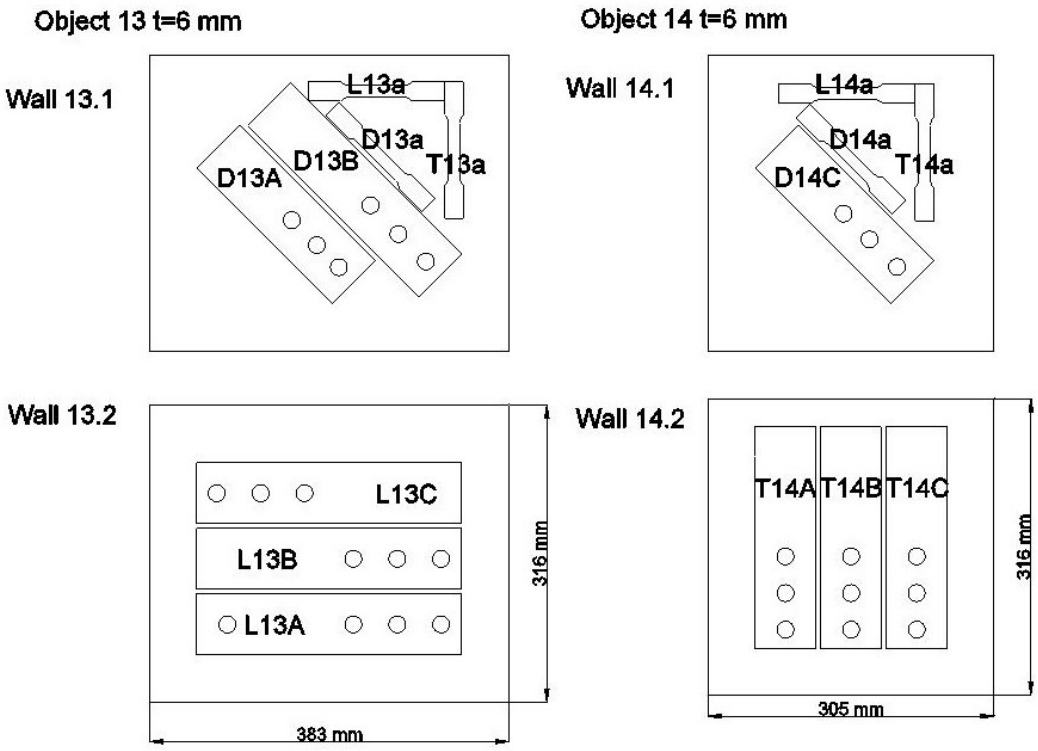

Figure 3.5: Tear-out thick specimens (printing direction horizontally)

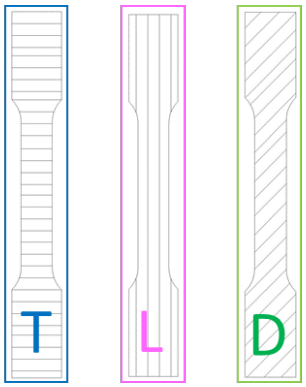

Figure 3.6: Printing directions of specimens; transversal, longitudinal and diagonal (45°)

To have a more regular top weld surface, even after the built-up of quite some layers, the fabrication sequence is as follows; one clockwise bead, then an anti-clockwise bead etcetera, this is demonstrated in 3.1. The weld stopped and started in one of the cylindrical parts.

When the whole object was printed and cooled down, it was cut from the substrate. In figure 3.8b the cuts can be seen.

3.1.2. Type of carbon steel

The carbon steel wire type that is used is $ER70S-6$ type $G4Si1$, also called Carbofil 1A.This is the type that is used by MX3D, therefore this carbon steel wire is chosen for this research. ER indicates that the wire is used for MIG or TIG welding. 70 stands for the tensile strength of the wire; the unit is psi, common in the Imperial Standard System. S means that the filler metal wire is solid. 6 indicates the chemical composition of the coating of the wire; which is copper in this case [5]. $Si1$ means that the chemical composition consists of 1% silicon. The yield strength when welded is 460 MPa, the tensile strength when welded 530-680 MPa. The datasheet with the properties of the used Oerlikon's Carbofil 1A wire can be found in [50].

Summary preparation of specimens: printing

Eight objects are printed and every object consists of two walls. Out of these walls, the test specimens are cut, for both tests; tensile and tear-out. The size of the specimens determines the amount and geometry of the objects that are printed. Every object took eight hours to be printed with a low carbon wire, called Carbofil 1A.

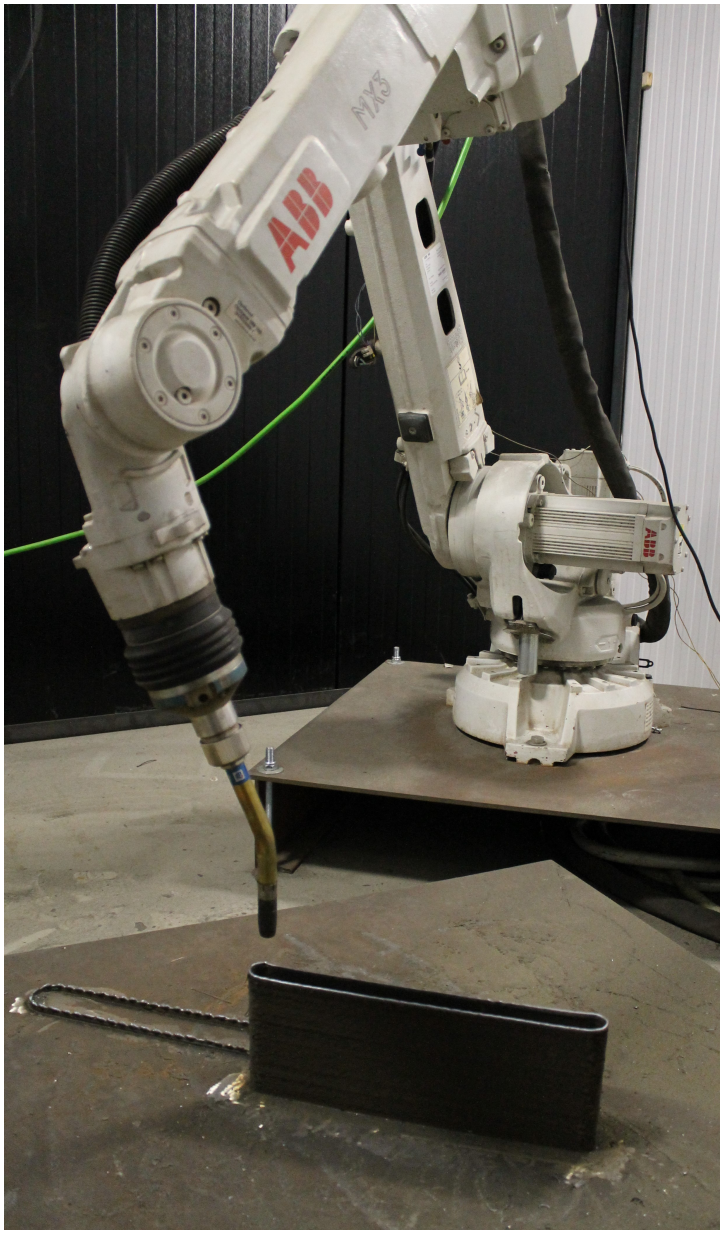

Figure 3.7: Welding robot MX3D

3.2. Preparation of specimens: cutting

The second step in the production of the specimens for the tests that are performed, is the cutting of the printed object into plates. Out of these plates the specimens are then cut. Three different printing directions in relation to the applied force are tested. The walls are printed in one direction only. To acquire the different directions in the specimens, the cutting is done in different directions, as can be seen in figure 3.2 till 3.5. Four objects are printed for the tear-out tests, two for the two thicknesses. The same holds for the tensile tests; four objects are printed, two for each thickness.

A water jet cutter is used. When cutting steel with this machine, not only water is used to cut, but an abrasive is added, in this case fine sand. The amount of sand determines the quality of the cut. The water is under very high pressure, almost 4000 bar. The velocity of the water with the sand is more than 900 km/h [1]. Due to this high velocity, the steel can be cut. The reason not to use a saw is that this causes the plate to heat up and this high temperatures might influence the crystal structure and therefore the mechanical properties. This is undesirable, so a water jet cutter is used instead [16].

As can be seen in figure 3.2, 3.3, 3.4 and 3.5 three milled and seven tensile test samples are cut

(a) Printed carbon steel object (b) Plates, cut from the object

Figure 3.8: Printed carbon steel

per thickness and print direction. Two thicknesses three printing directions are investigated, so a total of 60 tensile coupon tests is performed. In figure 3.9a the diagonal samples are seen and in figure 3.9b the transversal samples are marked with their names. The names of the samples are as follows: the first symbol is the letter that indicates the printing direction compared to the applied force, as is shown in figure 4.1. The force is applied in vertical direction. This printing direction is also called weld direction, due to the direction of the applied force.

- T = transversal = perpendicular
- L = longitudinal = parallel
- D = diagonal = with an angle of 45 °

The second symbol is a number that indicates the object it originates from. And the last and third symbol is a letter, lowercase for tensile coupons and capital for the tear-out plates, that shows the specific specimen in an object.

Figures 3.4 and 3.5 show the 18 tear-out specimens. The number of bolt holes indicate the number of tests: 50 in total. The rectangular tear-out test plates all have a width of 65 mm, so a net section failure is not likely to occur. The shorter ones are used for two tests and the longer ones for three tear-out tests. This means that the latter must be long enough for three pin holes with their end distances and the plastically deformed region above the bolt to be cut off. After a tear-out tests enough space must be available for clamping and for the next test.

Summary preparation of specimens: cutting

A water jet cutter, that decreases the amount of heat that is released by the cutting process, is used to cut 60 tensile coupons out of the eight plates of two different thicknesses. 18 tear-out specimens are cut out of the other eight plates, on which 50 tear-out tests can be performed. The specimens are cut such that three printing directions can be tested.

3.3. Preparation of specimens: milling

The surfaces of the printed plates are very rough and irregular, especially when compared to rolled steel plates. The application of the printed plates in structures will be as-printed, without milling. Milling is a process of machining. To leave the plates with the as-printed surface is quicker, cheaper and it

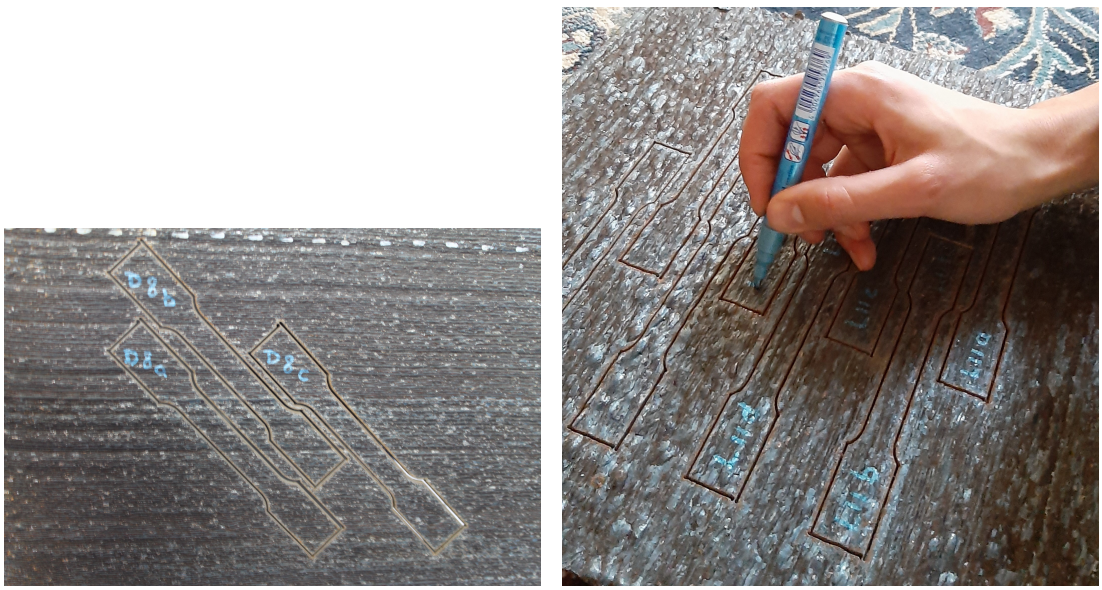

(a) Diagonal specimens

(b) Marking the specimens

Figure 3.9: Water jet cutted printed carbon steel

is not necessary for the connection to mill the printed part. The best representation of the node in a structure is unmachined. The ISO standard allows milled test pieces [11].

To have a better understanding of the printing technique and the effects of it on the strength of the printed steel, it is helpful to have some of the samples in the milled appearance, as this is the basis for the determination of the effective thickness of the as-printed samples. That is why 18 tensile specimens are milled.

The effective thickness is determined when the strength of the milled and the as-printed specimens is known. The thickness of the milled specimens can be defined very easily by using a calliper, as the surface is smooth and flat. For the determination of the mean thickness of the as-printed specimens, more complicated methods are needed, as the Archimedes' principle or 3D scanning. When comparing the test results of the as-printed and milled specimens, the influence of the surface roughness can be determined. In figure 3.10 the difference between the as-printed and the milled specimens can be seen. The milled specimen at the bottom of figure 3.10b has a porous weld in the middle, this was due to a printing error. The results of these specimens are not used.

The quality of milling is guaranteed according to the standard ISO 9001 [6]. For the thick specimens with an average thickness of $6\ mm$ a conventional milling machine is used. For the thin pieces with an average thickness of $3\ mm$ a surface grinder is used instead, because they would fail during milling. The heat input in these processes is negligible.

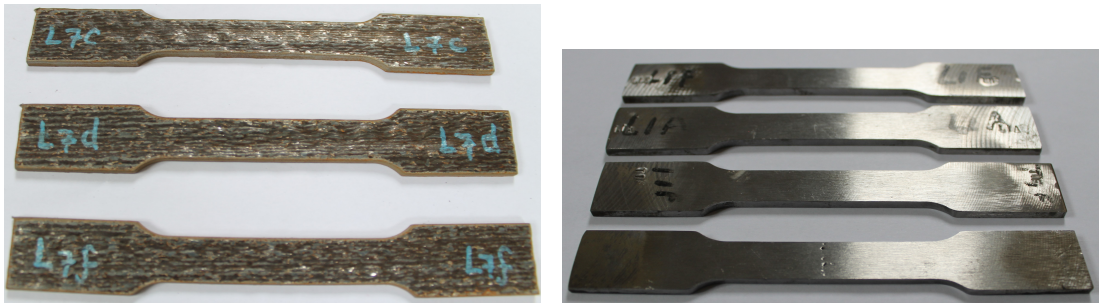

(a) As-printed

(b) Milled

Figure 3.10: Tensile specimens

Summary preparation of specimens: milling

The surface of 18 tensile pieces is smoothed; the irregular surface is milled, until it becomes flat and shiny. The test results of the milled samples are the basis for the determination of the material properties. These results can be compared to the as-printed specimens, to see the effects of the surface roughness on the strength.

3.4. Geometry determination

The geometry determination of the specimens is easy for the length and the width; those distances are water jet cut, as can be read in section 3.2 and can be measured by a hand calliper, because of the smoothness of these cut edges.

The cut is not exactly made perpendicular to the surface, so with an angle of 90 degrees, but under a very small angle in the direction of sample, so the cross section of the specimen is somewhat tapered. In figure 3.11 an exaggerated cross section of the middle part of a tensile coupon can be seen.

The thickness of the milled specimens is also measured with a hand calliper, but the thickness of the rough specimens can be calculated by the Archimedes' principle.

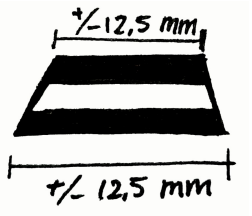

Figure 3.11: Exaggerated tapered cross section tensile coupon

3.4.1. Archimedes' principle

At the buoyancy test or Archimedes' principle, the steel sample is weighed in the air m_1 and in water m_2. Via the difference in weight between these two measurements and the density of the water ρ_{fl}, the total volume of the specimen is determined, as can be seen in equation 3.1. The cut edges of the sample can be measured by the calliper, so the total area A_{total} in figure 3.14 is known and calculated in equation 3.3. The dimensions from figure 3.14 are the desired sizes in [mm]. The real widths and lengths are measured by calliper for every tensile coupon. An average value is taken for every dimension. The average thickness of the total rough specimen can be calculated by equation 3.2. The values of these measurements can be found in appendix B.

$$V = \frac{m_1 - m_2}{\rho_{fl}} \tag{3.1}$$

Where:
ρ_{fl} = ρ_{water} = 998 $[kg/m^3]$
m_1 = $m_{in\ air}$ = dry mass $[kg]$
m_2 = $m_{in\ water}$ = mass in water $[kg]$

$$t_{average} = \frac{V}{A_{total}} \tag{3.2}$$

$$A_{total}[mm^2] = 2w_{end}\ L_{end} + w_{middle}\ L_{middle} + 4A_{corner} = 2 \cdot 20 \cdot 35 + 12.5 \cdot 58 + 4 \cdot 10 \tag{3.3}$$

3.4.2. 3D scanning

At the faculty of Industrial Design a handheld 3D scanner is available; the Artec Space Spider [2]. The 3D model, which is made out of photos by the scanner, a process that is called photogrammetry, is exported to a CAD programme, named Artec Studio 12, wherein the variance in thickness is seen and measured at certain sections. The scanner has a point accuracy of 0.05 mm and a 3D resolution of 0.1 mm.

In figure 3.13 the test set-up can be seen; on the bottom on the left the tensile test specimen is clamped in a bench vice that stands on a rotating table. On the right the Spider scanner is held and moved up and down, whilst the table is pushed and rotating, so a scan in one go is created, without having to merge several scans. This would namely introduce inaccuracies.

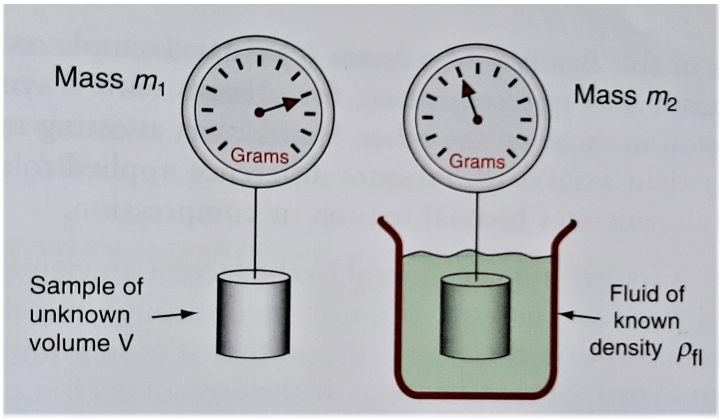

Figure 3.12: Archimedes' principle [17]

When the scan is made, the sample is put in the right coordinate system; the planes of the sample along the x-, y- and z-axis. This is done in order to make sections of the sample along a two-dimensional plane (x-y for example). Multiple sections are made and the perimeter is calculated of every single one.

Figure 3.13: 3D scanning

3.4.3. Statistical measures

Some statistical measures are applied on the thickness measurements, so the area (thickness times width) is determined, and the stress can be calculated, after the load is known, as can be seen in equation 3.7. It is important to determine the stress-strain curve, so the yield and the ultimate stress

can be defined. The strength of the material, as well as the stiffness (the Young's Modulus), is known, and the brittleness is determined. To be able to compare the specimens, the variable value of the cross-sectional area A must be left out. In Annex D of NEN-EN 1990 and ISO NEN-EN 6892-1 [11] guidelines on statistical evaluations can be found.

With equation 3.4 the standard deviation can be calculated, which indicates what the difference, upper and lower bound, of a calculated value can be. In chapter 4, figure 4.5 for example, a box plot can be seen with so called 'whiskers' that indicate the standard deviation.

Equation 3.5 shows how μ, the mean value, can be calculated. Seven ($n = 7$) as-printed tensile samples are tested and three ($n = 3$) milled samples for every weld direction and thickness.

$$\sigma_x^2 = \frac{1}{n-1}\sum(x_i - \mu_x)^2 \tag{3.4}$$

$$\mu_x = \frac{\sum x_i}{n} \tag{3.5}$$

$$V_x = \frac{\sigma_x}{\mu_x} \tag{3.6}$$

Where:
σ_x = Standard deviation
n = Number of tests
x_i = Value of variable
μ_x = Mean of the n test results
V_X = Coefficient of variation of X

Summary geometry determination

Several methods are applied to determine the geometry of the samples. The calliper, as well as Archimedes' principle and the 3D hand scanner, are used to deduce the dimensions of the samples, as-printed and milled. The thickness of the irregular as-printed sample surface was hard to measure, so an average value is determined with Archimedes' principle.

3.5. Experiment: tensile coupon test

Tensile tests, according to ISO [11], are performed on WAAM carbon steel coupons. In the following paragraphs, the test set-up and the methods of measuring are explained.

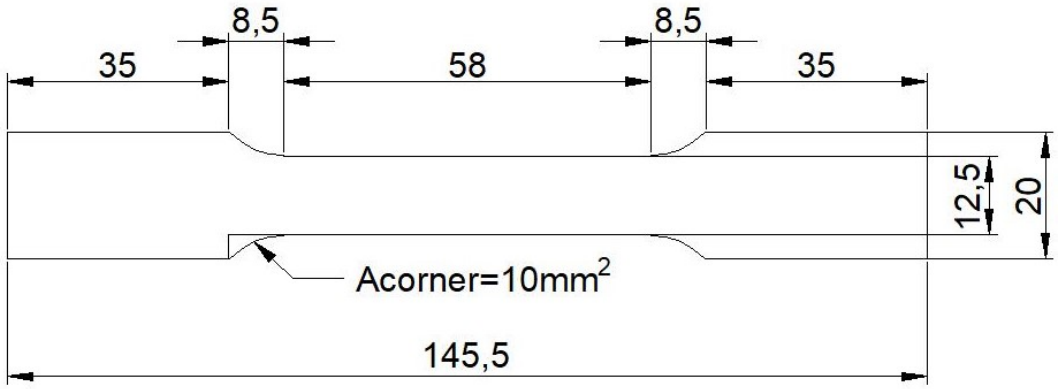

Figure 3.14: Tensile coupon dimensions

Samples with two different thicknesses were produced by MX3D and tested in the laboratory of the faculty of Civil Engineering in Delft, so a comparison could be made; walls with thickness around six and three mm were fabricated.

The time that the printing takes is a factor that was taken into account; the more material that has to be deposited, the longer the printing takes, as the cooling down of the object takes time for example. An extra reason to use a smaller thickness than usual is due to the optimisation opportunities AM has; in general construction material is saved, which may lead to smaller thicknesses of the plates in a connection.

The dimensions of the other parts are determined by the boundaries given by the ISO 6892-1 [11], table D.2 in Annex D. The dimensions can be seen in figure 3.14. The extensometer that has a length of $50\ mm$ must fit on the smaller width of $12.5\ mm$, so this part must be a bit longer to have a smooth transition of forces from the wider ($20\ mm$) to the smaller part. The wider part of $35\ mm$ is the gripping part for the clamps of the tensile test machine.

The specimens are cut out of a 3D printed wall on a base plate. There is more information on the influence of the location of the specimens in the wall in section 2.4.

The tensile tests are done to determine the mechanical properties of the printed steel. When the area (A), which is the width (w) times thickness (t), of the sample is known and the applied tensile force (F) on the steel is measured, the yield and ultimate stress is calculated with equation 3.7. The material used to manufacture the steel is a carbon steel wire, with a tensile strength, when welded, from 550 to $630 MPa$. This means that the maximum force that is needed to exceed the tensile strength of the material is $12.5 \times 6 \times 630 = 47\ kN$. The machine used has a capacity of $200\ kN$ when statically loaded, which was the test configuration here. The Instron machine can be seen in picture 3.15a.

The tensile tests are performed on specimens with welds in the direction parallel, transversal and 45 degrees to the applied force.

$$\sigma = \frac{F}{A} \tag{3.7}$$

$$\varepsilon = \frac{\Delta L}{L_0} \tag{3.8}$$

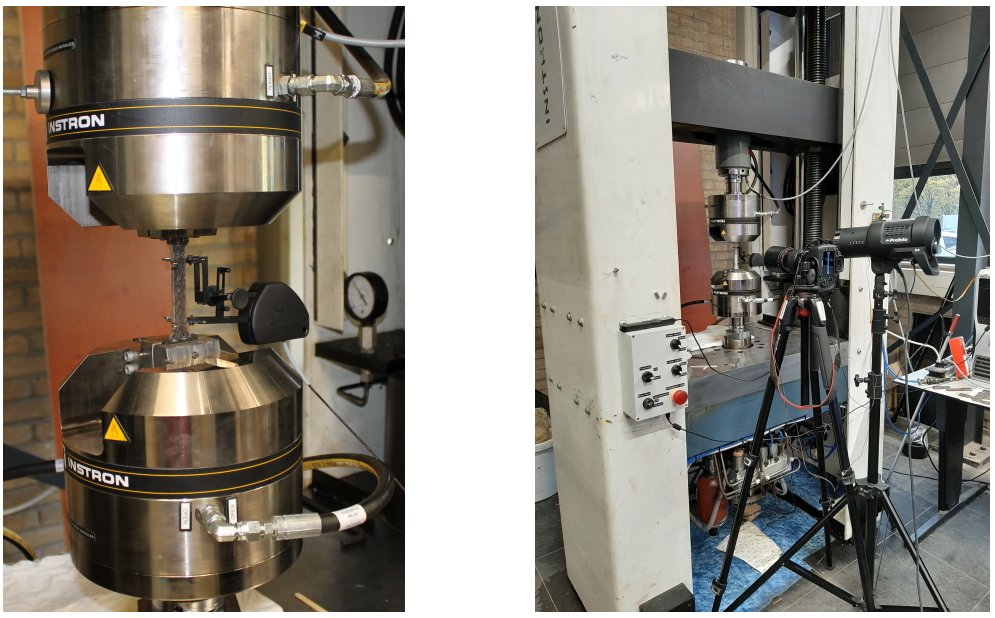

(a) Tensile coupon with extensometer

(b) Camera and flash for 2D DIC

Figure 3.15: Tensile test set-up

3.5.1. Guideline for tensile test

The standard ISO 6892-1, Annex D is used to determine the specimen dimensions for the tensile coupon test. Certain restrictions are given for the dimensions, such as a minimum total length, which is in this case $145.5 mm$, as can be seen in figure 3.14. The extensometer (more can be read in section 3.5.3) with a length of $50\ mm$ must fit on the middle part of the specimen of $58\ mm$ length, that has

a width of $12.5\ mm$. The interjacent part between the $20mm$ and $12.5\ mm$ wide part needs to have a radius (r), so a form as is shown in figure 3.14 is produced.

The clamping parts of tensile specimens that have a length of $35\,mm$ could have been up to $50mm$, but due to considerations such as material savings and reduction in printing time, a shorter clamping length is chosen.

3.5.2. Tensile test set-up

The tensile coupons are clamped into the hydraulic machine, a Schenck 200kN. The clamping edges of the specimens, that are $35\ mm$ in length, do not need smoothing, due to the fact that the clamps are tight enough; when tightened, the clamping edges of the steel specimen are pressed and a ticking sound is heard. The clamps itself have a length of $50\ mm$, but for the sake of material saving, the tensile coupons are made smaller.

Just before clamping the specimen, the side is pushed against a small steel strip, that is placed under an angle of exactly 90 degrees, so the specimen can be placed in the axial direction of the machine; in the direction of the force. Some samples were bend in the thickness direction due to milling. Those were pushed straight, when the second clamp was applied.

The axial force that is applied on the specimen by the machine is measured, as well as the difference in length, compared to the initial length, between the clamps, when pulling. This difference in length includes the slipping of the clamps, the movement of the machine and the elongation of the hole specimen, the clamping edges included. This is why a static axial clip-on Instron extensometer is used; to measure the elongation of a smaller length, of $L_0 = 50\ mm$. More on the extensometer can be read in section 3.5.3.

The load that is applied by the machine is displacement driven. During the first phase, that is linear elastic, a velocity of $0.005\ mm/s$ was applied. When the yield plateau was reached, the velocity was increased to $0.02\ mm/s$. After 300 seconds, when the plastic deformation phase had begun, the velocity was increased to $0.05\ mm/s$.

The extension is measured by the extensometer and the force by the testing machine. Now, the stress-strain diagram can be calculated.

3.5.3. Extensometer

To be able to do measurements on the extension (ΔL) of the tensile specimen, that has a length of $58\ mm$ with a small width of $12.5\ mm$, as can be seen in figure 3.14, an extensometer was needed. ΔL is measured when the load is applied statically by this axial clip-on tool over an initial length of $L_0 = 50\ mm$. The strain can then be calculated according to equation 3.8.

When a tensile static force is applied on the specimen, it will elongate. This elongation measurement of the extensometer has a maximum, due to the maximum displacement of the clips, and it is around 20%. This means that the deformation measurement is stopped.

3.5.4. Digital Image Correlation tensile coupon test

An extra measuring instrument was used during the tensile test, next to the extensometer, which is called Digital Image Correlation (DIC). DIC was used used for the tear-out tests mainly, in order to see the strain development, also locally. To get familiar with the DIC process and the analysis of the photographs, 22 tensile coupons were also tested with DIC.

The specimen is painted with a white rubber paint with black small dots sprayed on top of it. This flexibel paint stretched along with the elongation, like a rubber band and stayed on the specimen, even after failure. One photo of the specimen per second was made when the tensile load was applied and later, when the yielding was over, every 10 seconds a photo was taken. For every photo a flash was needed, this resulted in a delay of making photos and less photos than every second; around 10 %.

The difference in location of the black dots of one photo compared to the following is photographed. Thereby the displacement and strain in the specimen are determined with the GOM correlate software. The cracks that arise are seen as well. An extension-photocount graph is be made over a certain, self-determined, distance. The data of these graphs is exported to an Excel file. In this way they can be compared easily to the extensometer results.

The results of the extensometer should also be extension over time, to be comparable with the DIC results. The displacement of the specimen by DIC should be over a length of $50\ mm$, as this is the initial length of the extensometer.

Summary experiment: tensile coupon test

The tensile coupon tests are performed according to the ISO standards. The extension of the middle length of $50\ mm$ is measured by the extensometer and by Digital Image Correlation (DIC). The strains can be computed with both methods. The force is measured by the tensile testing machine and a stress-strain diagram can be made from these data.

3.6. Experiment: tear-out test

When the material properties, such as the effective thickness t_{eff} and the ultimate strength f_u are known, due to the tensile tests that were carried out, the second test could be performed: the tear-out test. The maximum force that was applied on a tear-out test sample was determined. The printed specimens were designed to fail in tear-out. Like the tensile tests, these tests were also performed on samples with the welds in three different directions; transversally, longitudinally and at an angle of 45°, compared to the direction of the applied force. All the tear-out tests were done on as-printed samples, as the use of the investigated connection will be in the as-printed condition.

In figures 3.4 and 3.5 it can be observed how the tear-out samples were cut out of the WAAM plates.

For the attachment of the bolt or pin, a hole was drilled through the 3D printed plate. By drilling instead of printing, a smooth and regular bolt hole was made, so the forces of the bolt or pin acting on the plate could be applied uniformly. When these holes shall be made in connections, this shall be done by CNC machining, so a drilled hole is a good representation.

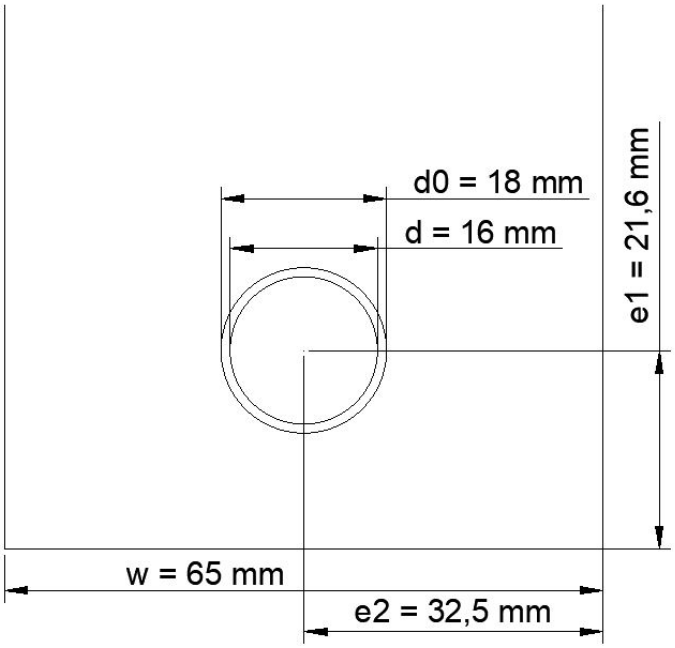

Figure 3.16: Tear-out specimen dimensions

3.6.1. Tear-out test set-up

In figure 3.16 the dimensions of the printed plate with the bolt diameter d and bolt hole d_0 can be seen. The end distance e_1 equals $1.2d_0$ was chosen as the target value for this research, as this is the minimum required end distance for the tear-out of single bolts in a plate, according to the EC1 [9]. From a distance of $3d_0$ bearing failure is considered. More on the failure modes can be seen in section 2.5 and figure 2.11.

This 3D printed plate was clamped into the upper clamp. Two other, conventional, steel plates with a hole were put on both sides of the printed plate and were bolted, each with three M6 8.8 bolts, onto

the base plate. The base plate is again attached to the lower clamping plate by two M12 8.8 bolts. This set-up is also called "Double lap joint".

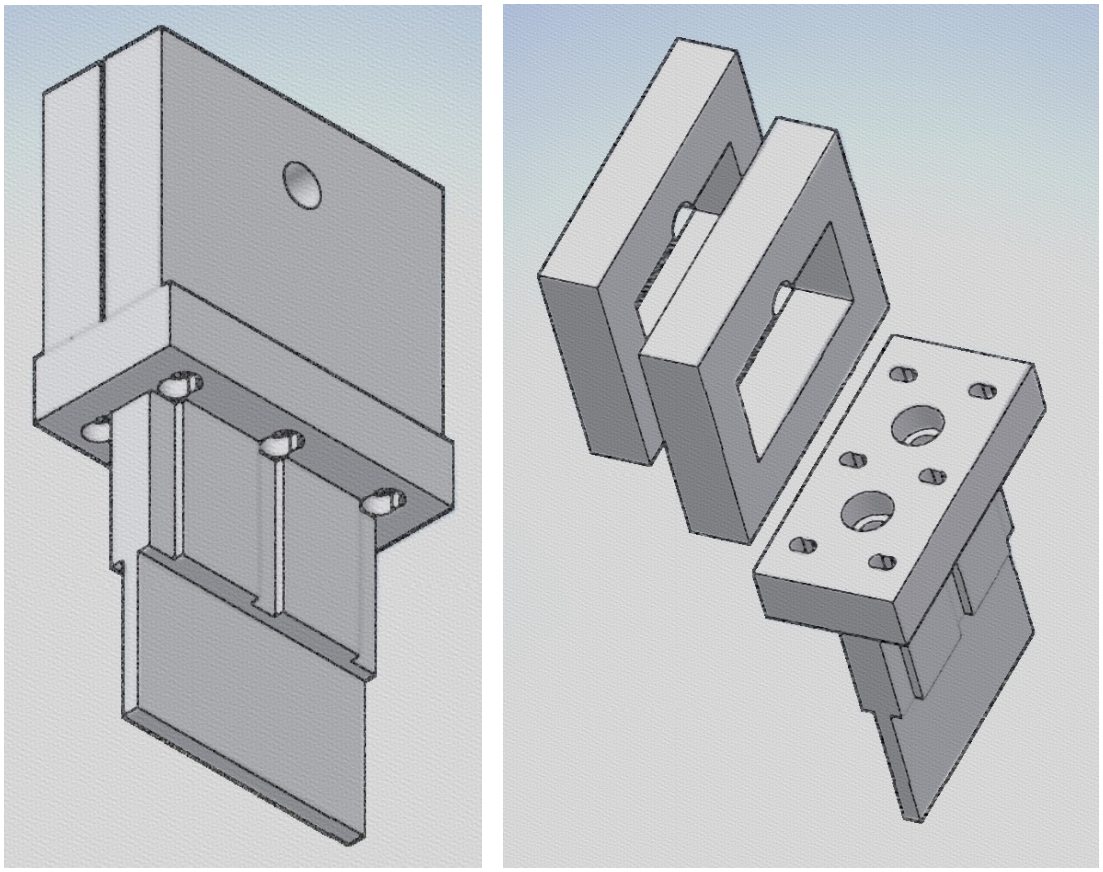

(a) Bolted connection (b) Pinned connection

Figure 3.17: Tear-out test set-up with different pairs of side plates

Two types of side plates were needed; one pair for the bolted connection and one for the pinned, as can be seen in figure 3.17. The first type of side plates 3.17a was for the test as it is normally done for a bolted connection. The bolt was attached with washers and a nut. A bolt M16 of class 10.9 was used, an overdimensioned bolt, to be sure bolt failure would not appear. The second type was especially designed for the DIC measurements; with a M16 10.9 pin.

In order to use the Digital Image Correlation (DIC), which was only done on the plates that are connected with a pin, the printed plate with the hole had to be visible, so the strains could be determined. This was done by making holes in the pin side plates that are wider and longer than the part of the printed plate that was visible when testing, as can be seen in figure 3.17b.

To improve the visibility of the WAAM plate even further, the decision was made to use a pin for half of the tear-out experiments instead of a bolt with nuts and washers. A comparison between the results of a bolt versus a pin will point out the interchangeability of the two.

The bolt with washers on both sides, so between the nut and the plate and between the head and the plate, was put through the three plates and the bolt was hand-tightened with a spanner by a nut. The same tightening force could be applied in this way, so this parameter would not be of influence on the tear-out strength [30]. The test set-up can be seen in figure 3.18c. The bottom middle plate is the Additively Manufactured (AM) plate.

Two thicknesses of WAAM plates were tested; one with an average thickness of 3mm and the other of 6mm. The space between the side plates could be adjusted by the slotted holes in the base plate, as can be seen in figure 3.17. This variation side plate position was not enough, so by turning both side plates with an angle of 180° with respect to the vertical axis, the gap for the WAAM plate could be varied, so both plate thicknesses fitted.

The tear-out test was displacement controlled. A speed of $0.025\ mm/s$ was used. Multiple researches that are conducted on single bolt connections have used the same speed, such as Wang et al., Snijder et al. and Može and Beg. These experiments are mostly on the bearing failure, but are nevertheless comparable with the experiments of this research.

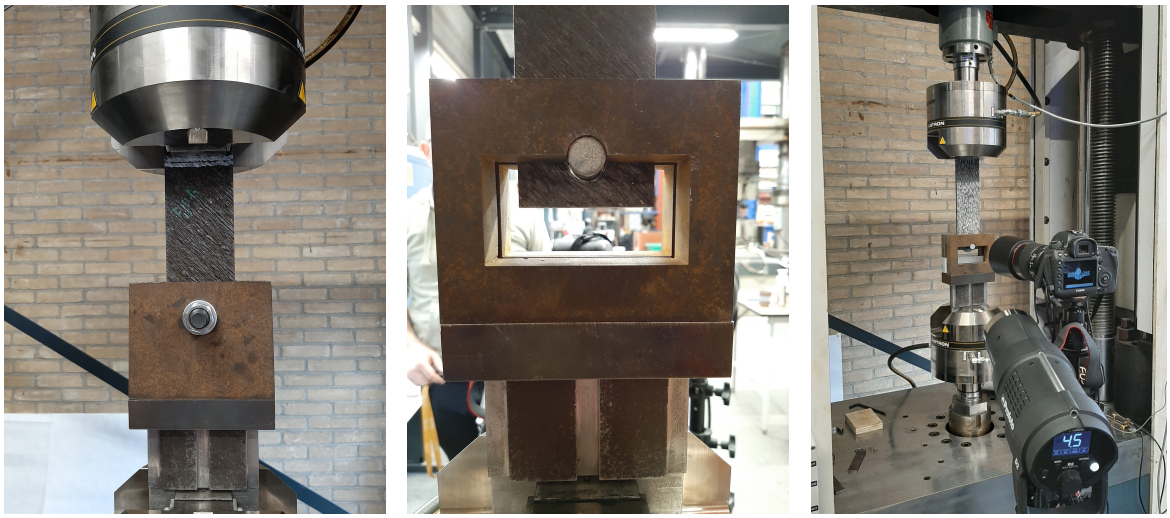

(a) Bolted (b) Pinned (c) Pinned with DIC

Figure 3.18: Tear-out test set-up

3.6.2. Digital Image Correlation tear-out

In section 3.5.4 everything can be read on 2D DIC. When two cameras are used instead of one, 3D DIC can be applied, as the depth can be captured. When bearing failure occurs, out-of-plane deformation of the steel underneath the bolt or pin can appear. The rest stays the same as for the 2D method.

In this research the end distances e_1 are designed such that bearing will not take place, but tear-out. From an end distance of around $3d_0$ bearing can take place.

Summary experiment: tear-out test

The tear-out test is the second type of test that is performed. This test is done with a bolted and with a pinned connection, to see if they are comparable. Normally, these tear-out tests are done with bolts, but in this case the strains in the printed specimen must be detected by DIC as well, so a pin is applied instead.
The samples for tear-out are tested in three printing directions, just as the tensile tests; transversally, longitudinally and under an angle of 45° compared to the force direction. The plates are in the as-printed condition.

3

4

Results

In this chapter the observations of the tests are described. The analysis of the results and observations are discussed in chapter 5.

4.1. Geometry results

Tables of the calliper measurements of the width of the tensile coupons can be found in appendix B. The thickness is not easy to find, due to rough and irregular surface that is made by the wire and arc additive manufacturing (weld layer on top of weld layer). When measuring with a calliper, the maximum thickness is determined. It is useful to calculate the effective thickness t_{eff}, the thickness that contributes to the strength of the material, so to the area on which the force is applied. This t_{eff} is used for design calculations of WAAM carbon objects. When a relationship between the as-printed, milled, average and effective thickness can be established, it is possible to implemented it in the design standards.

As discussed in 3.4, the Archimedes' method is used to calculate the average thickness of the rough specimens. To verify this method, the thickness of the milled specimens, that is measured by the use of the calliper, as they have a smooth surface, is compared to the thickness calculation by the Archimedes method. The result of this comparison is a difference of 10% maximum. Tables of these measurements can be found in appendix B.

4.2. Tensile test results

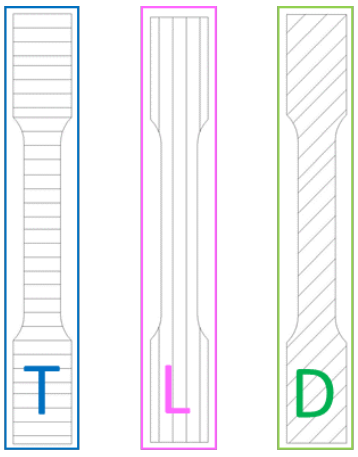

Figure 4.1: Colour explanation of printing directions of specimens in graphs

In total 60 tensile tests are performed. On as-printed, milled, transversal, longitudinal, diagonal (welds in the direction of 45 °), thin specimens with a target thickness of 3 mm and thick specimens with a target of 6 mm. From here on, the former is called **thin** and the latter **thick**. The reason is that the as-printed samples have an irregular surface and therefore the thickness cannot be determined easily, so precaution is needed when naming these values.

The last 12 tensile tests that were carried out, were extra tests. The tear-out samples were not cut out of the same plates as the tensile coupons. So, in order to make sure that the same kind of material was used, with the same material properties, extra coupons were cut out of the tear-out plates, as can be seen in figure 3.4 and 3.5.

One third of total amount of tensile tests is performed on the specimens that are named 'Transversal', which means that the force is applied in the direction perpendicular to the weld bead direction, as can be seen in figure 4.1; the first sample. The specimens are marked with their name, for example T1b. This

means that the specimen will be loaded in the transversal direction, hence the T and that the sample is cut out of object number 1. The b stands for the number of the specimen in the row that is cut out of the plate, alphabetically a to f, when there are 6 specimens. This can be seen in figure 3.2 and 3.3.

The second kind of sample is the 'Longitudinal' sample; the load is applied parallel to the printing direction, which is the second sample in figure 4.1.

The third kind is the 'Diagonal' sample. The load is applied with an angle of 45 degrees to the printing direction, third sample in figure 4.1.

4.2.1. Measurements tensile tests: results

The output of the tensile tests is the time [s], the extension [mm] and the force [kN]. The extension is measured by the Instron extensometer over a distance of $50mm$ and the applied force by the Schenck machine. A force-deformation diagram is created. Some specimens are also measured by the DIC equipment. These DIC measurements are only used as a check. All results are made with the measurements of the extensometer. To be able to compare the specimens, that all have a different cross section, due to the irregular weld beads or the milling, stress-strain diagrams are made.

The stress σ is calculated by 3.7; the force F in [N] is output of the test and the area $A = w$ x t is an average value where the average width w of around $12.5\ mm$ is measured by the calliper and the thickness t is measured by the Archimedes' principle, as is explained in 3.4.1.The area A of the milled specimens is an average value of eight measurements, for the thickness as well for the width, done by the calliper.

The strain ε is calculated by 3.8; the difference in length ΔL is measured over a length of $L = 50mm$ by the extensometer, so a dimensionless value appears. This is also explained in section 3.5.3.

Several times a hold in the extension measured by the extensometer was seen, due to the large elongation of the (mostly longitudinal) specimens and therefore the maximum reached displacement of the extensometer. In these cases the Schenck machine still measured the displacement of the ensemble. Hence, the same curve for the extensometer as for the jack of the machine (the latter is called 'ensemble') was drawn. In this way the extensometer curve could be extended by the shape of the jack curve when the extensometer stopped measuring.

The stress-strain diagrams can be seen in appendices E and F. In figures E.1b and E.2b respectively a zoomed-in graph is made of the linear elastic part of these stress-strain diagrams. From these diagrams the Young's modulus E in [GPa] is determined by equation 4.1. The most linear part is taken to determine this; so when diagram E.1b is used to calculate the E-modulus for the thin milled samples, the line between 50 and $250\ MPa$ is taken into account.

$$E = \frac{\sigma}{\varepsilon} \tag{4.1}$$

4.2.2. Results milled tensile specimens

Three milled specimens are tested of every printing direction, transversally, longitudinally and diagonally. These samples are measured with a calliper, which can be done easily, as the surfaces are smooth. The thickness determination with calliper is compared with the Archimedes test, about which can be read in section 3.4. This results in a deviation of 10% maximum between both thickness measurements; calliper and buoyancy. This means that the Archimedes principle is reliable, also for the rough specimens, that are not measurable by the calliper, as the surface is so irregular, that only the maximum thickness would be measured.

In appendix E two times nine curves can be seen; for every printing direction and thickness, three milled samples are tested. The transversal coupons are displayed by continuous blue, the longitudinal by pink dashed and the diagonal 45° by green dash-dot curves. The graph of the milled thick tensile coupons can also be seen in figure 4.3. The values of the yield strength f_y, ultimate tensile strength f_u, strain at ultimate strength ε_u and Young's modulus E with their coefficients of variation V_{f_y}, V_{f_u}, V_{ε_u} and V_E are shown in table 4.2. The results of the thin coupons can be seen in table 4.1 and in the appendix, figure E.1a.

4.2.3. Results as-printed tensile specimens

The thin as-printed plates were very smooth, compared to the thick plates, which was due to the smaller amount of material that was deposited and the fact that less heat has been used by the WAAM

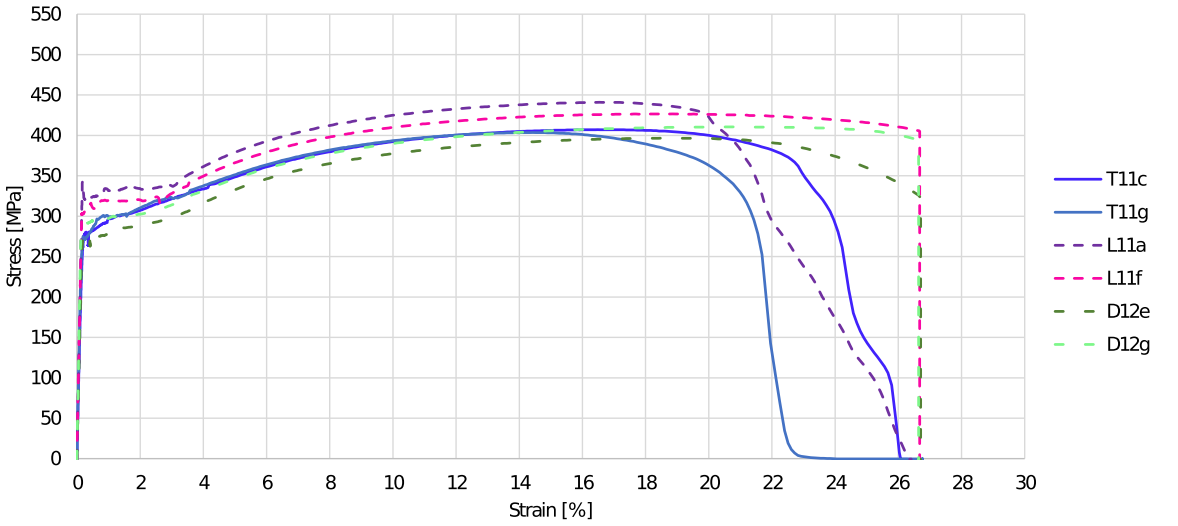

(a) Stress-strain diagram

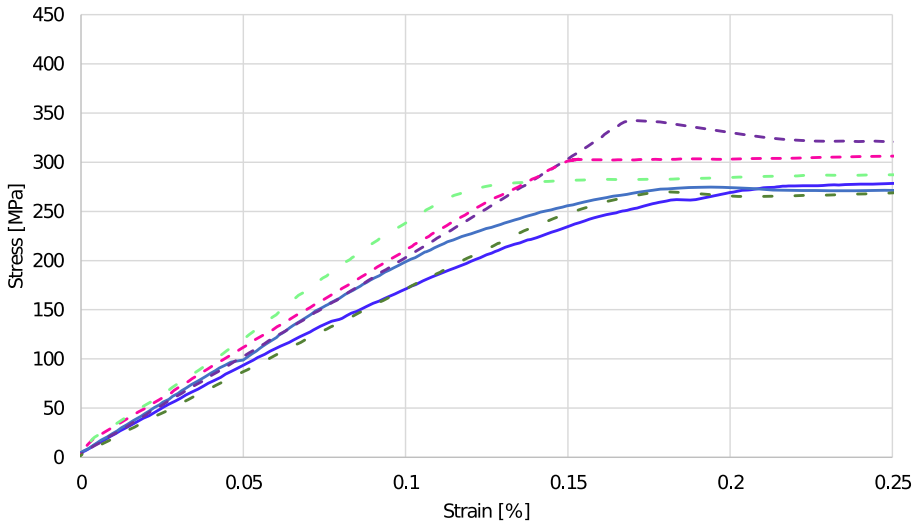

(b) Linear elastic part

Figure 4.2: Stress-strain diagram thick as-printed specimens

Table 4.1: Overview main results thin milled tensile coupon tests

Printing direction	**f_y [MPa]**	**V_{fy} [-]**	**f_u [MPa]**	**V_{fu} [-]**	**ε_u [%]**	**$V_{\varepsilon u}$ [-]**	**E [GPa]**	**V_E [-]**
Transversal	416	0.00980	511	0.0240	18.06	0.0765	197	0.0592
Longitudinal	400	0.0134	499	0.0106	16.28	0.162	197	0.0746
Diagonal 45°	393	0.297	484	0.0312	16.88	0.0308	205	0.0365

robot.

The behaviour of the transversal specimens is marked blue in the graphs, as can be seen in figure 4.1. Every sample is represented by another colour blue. The stress-strain curve of the transversal specimens does not have such a yield plateau as the longitudinal specimens have, as can be seen in figure 4.2b. The linear elastic phase merges gradually into the plastic phase. There is a kind of yield plateau, but not as horizontal as for the longitudinal specimens.

One of the transversal coupons broke outside the measuring area of the extensometer. Therefore, only the linear elastic part of this specimen is taken into account, so no ultimate strength or deformation

Table 4.2: Overview main results thick milled tensile coupon tests

Printing direction	f_y [MPa]	V_{fy} [-]	f_u [MPa]	V_{fu} [-]	ε_u [%]	$V_{\varepsilon u}$ [-]	E [GPa]	V_E [-]
Transversal	326	0.0203	466	0.00694	16.69	0.0486	207	0.0157
Longitudinal	318	0.0212	463	0.0119	20.63	0.0463	211	0.0316
Diagonal 45°	359	0.0157	468	0.00725	19.51	0.0639	212	0.0417

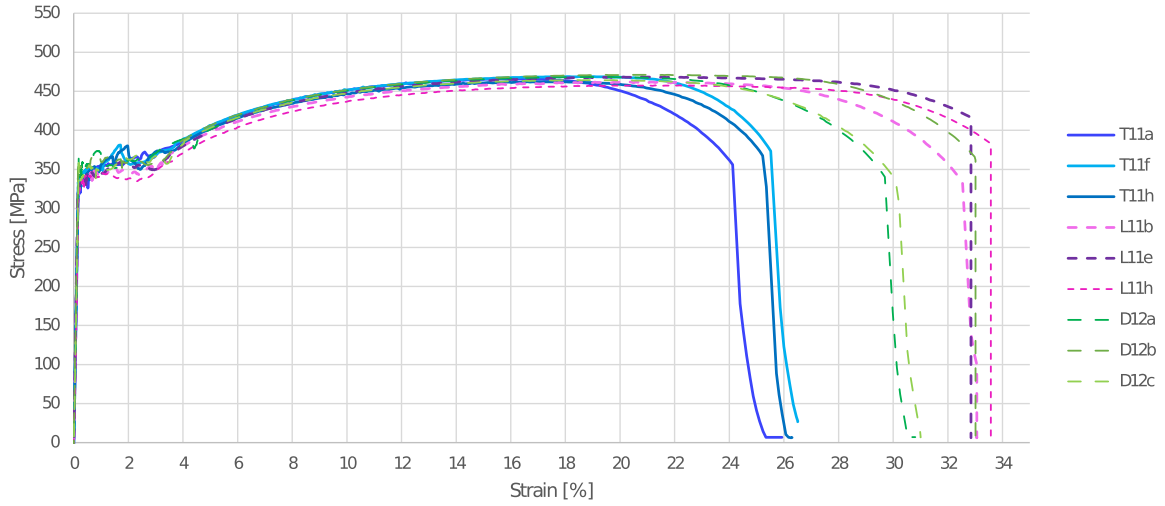

Figure 4.3: Stress-strain diagram thick milled specimens

4

is measured.

The behaviour of the longitudinal specimens is marked pink in the graphs, see figure 4.1. When tearing the longitudinal as-printed specimens apart in the axial direction, so parallel to the weld beads, a large elongation (deformation δ or strain) was seen. Necking appeared in the last stadium before the specimen broke in the part that had become smaller. It seemed as if the welds started elongating and stretching one by one, improving the strength and ductility of the specimen.

The stress-strain curve of the longitudinal specimens consist of a linear elastic part, a yield plateau and a plastic deformation phase, until the specimen breaks, as can be seen in figure 4.2a.

When tearing the diagonal as-printed specimens apart in the axial direction, so with an angle of 45 degrees to the weld beads, the green graphs are produced (figure 4.1).

Initially, five as-printed specimens are tested of every printing direction, transversally, longitudinally and diagonally (with an angle of 45°) and every thickness. In appendix F in figures F.1 and F.2 the stress-strain diagrams for the three printing directions can be seen. Figure F.1 that represents the thin as-printed samples, has a smaller variety in ultimate strain (the strain at ultimate strength f_u) than figure F.2 that shows the as-printed thick specimens. The thicker specimens have a lower yield and ultimate tensile strength than the thin samples. This could be due to the surface roughness or the different printing parameters. In chapter 5 the probable causes of these differences will be elaborated.

In tables 4.3 and 4.4 the yield f_y and ultimate tensile strength f_u can be found, together with the coefficients of variation V_{f_y} and V_{f_u}. Next to this, the strain at ultimate strength ε_u and the Young's modulus E are shown, with their coefficients of variation V_{ε_u} and V_E.

4.2.4. Extra as-printed tensile coupon tests

To have a value for the strength of the WAAM plates that can be used for the tear-out strength, extra tensile coupons are waterjet cut out of the plates of the tear-out samples, as can be seen in figure 3.4 and 3.5. The plates were printed in the same way as objects 7, 8, 11 and 12, but to be sure that the same material properties are relevant, these extra tests were performed. Three coupons in the three directions were cut out of plate 9.1, 10.1, 13.1 and 14.1. The results of these tensile tests (the

Table 4.3: Overview main results thin as-printed tensile coupon tests

Printing direction	f_y [MPa]	V_{fy} [-]	f_u [MPa]	V_{fu} [-]	ε_u [%]	$V_{\varepsilon u}$ [-]	E [GPa]	V_E [-]
Transversal	342	0.0417	464	0.0110	16.32	0.0551	216	0.123
Longitudinal	385	0.0355	478	0.0240	17.67	0.0599	201	0.0376
Diagonal 45°	340	0.0314	456	0.0258	16.69	0.0960	200	0.0454

Table 4.4: Overview main results thick as-printed tensile coupon tests

Printing direction	f_y [MPa]	V_{fy} [-]	f_u [MPa]	V_{fu} [-]	ε_u [%]	$V_{\varepsilon u}$ [-]	E [GPa]	V_E [-]
Transversal	268	0.0206	402	0.0263	14.03	0.169	178	0.0743
Longitudinal	316	0.0630	430	0.0245	19.16	0.0839	195	0.0579
Diagonal 45°	282	0.0299	410	0.0178	17.54	0.176	197	0.0114

continuous curves) are compared to the tests that were performed earlier (dotted curves); graphs are shown in figure 4.4a and 4.4b.

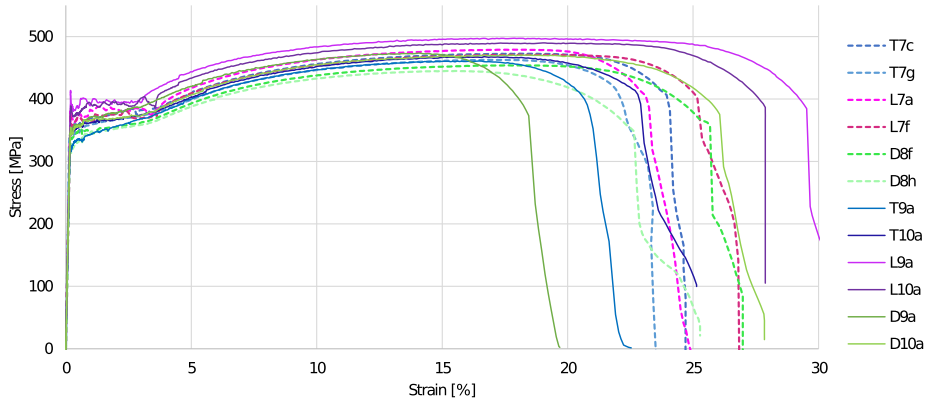

(a) Thin extra specimens

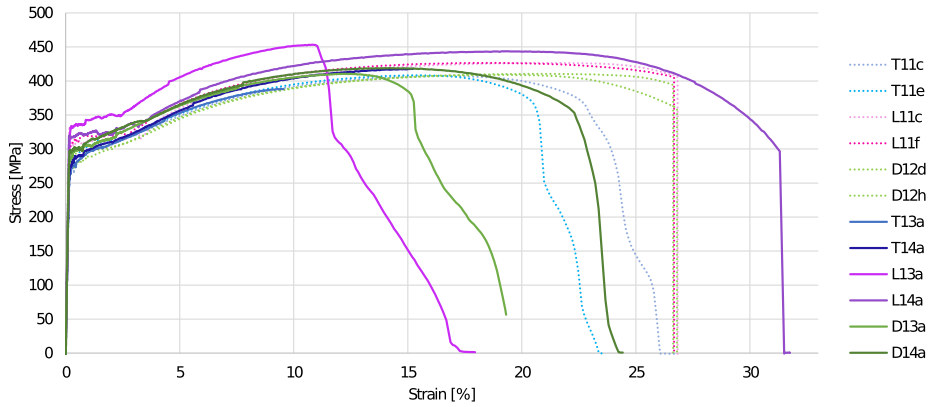

(b) Thick extra specimens

Figure 4.4: Extra tensile tests including first tests

4.2.5. Milled specimens compared with as-printed

A comparison of the results is showed in boxplots; in figure 4.5 the yield stresses are compared, in figure 4.6 the ultimate tensile stresses and in figure 4.7 the Young's moduli. All milled specimens have a higher yield and ultimate tensile strength than the as-printed samples. This difference is lowest for the longitudinal specimens; around 5% with a maximum of 8%. The differences of the milled versus as-printed specimens are comparable for the transversal and longitudinal samples; an average of around 15%. The biggest difference is of the yield strength of the thick diagonal specimens; 25%.

It can be stated that the more rough the surface of the specimen is, so the thicker the specimen, the smaller the strength. It must be said that an average thickness was taken for the as-printed samples to determine the strength. But, this decrease in strength also holds for the milled specimens, although the surface was smoothed and the thickness was determined more exact, namely with a calliper.

4.2.6. Influence of printing direction on results

This printing direction compared to the applied force could also be the reason for the difference in yield and ultimate tensile strength of the as-printed samples. This can be seen in figure 4.5a, 4.5b, 4.6a and 4.6a. The thin samples have the highest yield and ultimate strength in the following order:

I Longitudinal
II Transversal
III Diagonal

As for the 6 mm thick specimens the following holds:

I Longitudinal
II Diagonal
III Transversal

The differences between the transversal and diagonal values are not significant enough to state that the indicated order always holds.

4.2.7. Deformation capacity

It can be seen in tables 4.1 and 4.2 that the strain at ultimate tensile strength ε_u has a minimum of 16%. This is higher than 15%, which is one of the so called **Ductility requirements**: equation 4.3. **Deformation capacity** is another name and it is an important subject when it comes to the design of structures. A certain amount of ductility is needed before failure of the steel (or the whole structure), so some deformation takes place as a warning before total collapse, as can be read in Eurocode 3-1-1, part 3.2.2 [10]. In the next equations 4.2, 4.3 and 4.4 the recommended values are revealed.

$$\frac{f_u}{f_y} > 1.10 \tag{4.2}$$

$$\Delta L_{fracture} \geq 15\% \tag{4.3}$$

$$\varepsilon_u > 15\varepsilon_y \tag{4.4}$$

Two samples in figure E.1a failed earlier than the others; sample L7b and T7a, so the deformation capacity was lower for those two specimens specifically and therefore also lower for these two printing directions as a whole. Namely; the mean value of those samples is taken as the value for the deformation capacity. In figure E.2a it can be seen that all the transversal specimens, the blue lines, failed before an ultimate strain ε_u of 20% was reached.

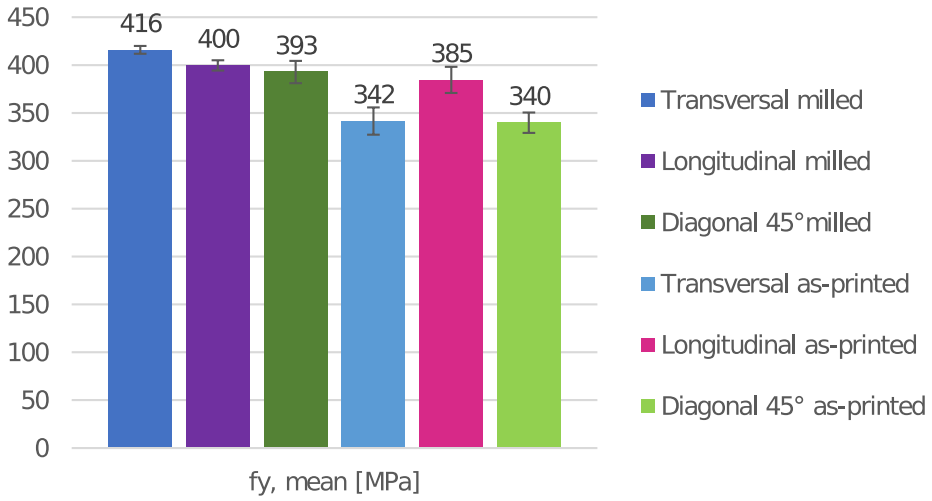

(a) Thin specimens

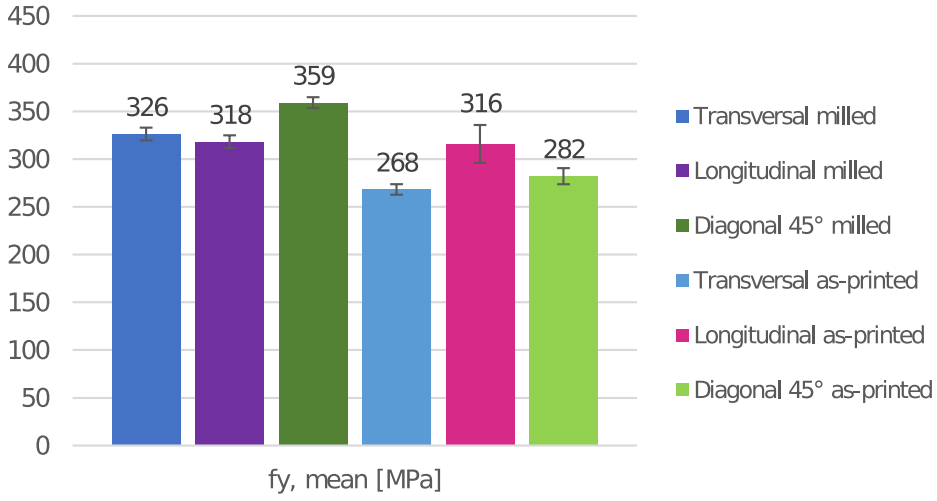

(b) Thick specimens

Figure 4.5: Yield strength

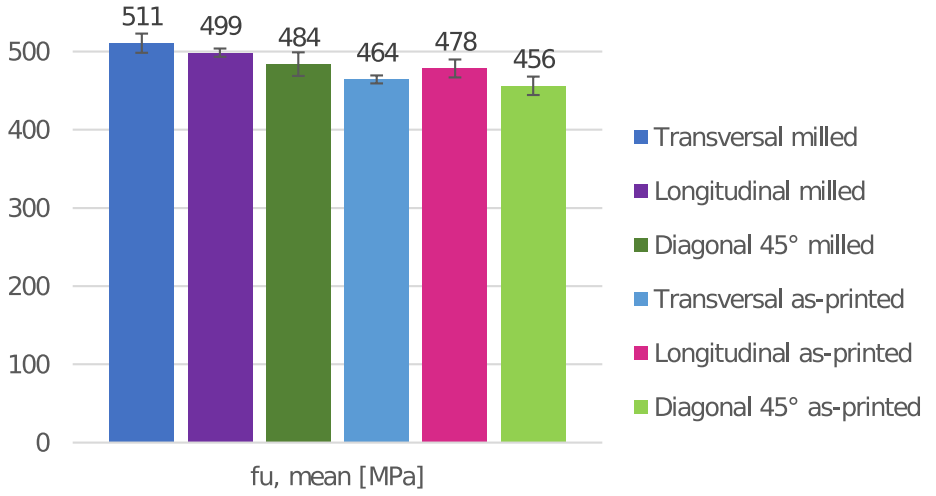

(a) Thin specimens

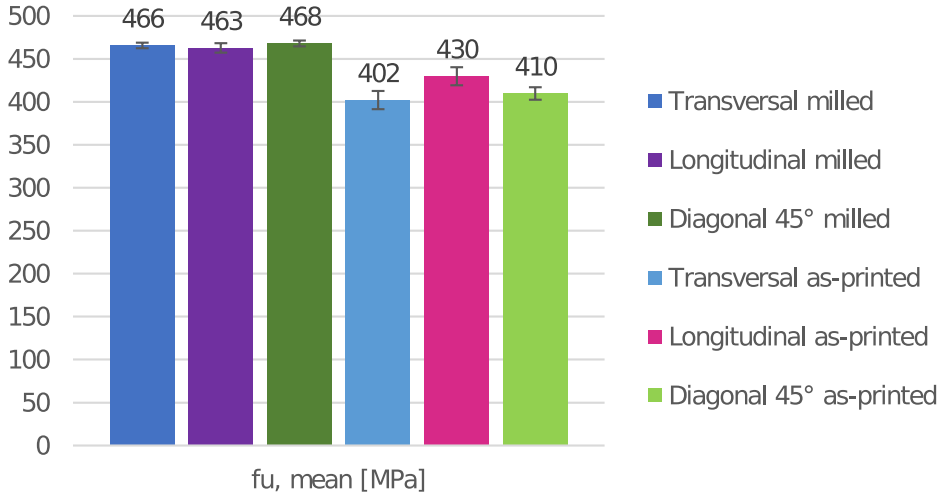

(b) Thick specimens

Figure 4.6: Tensile ultimate strength

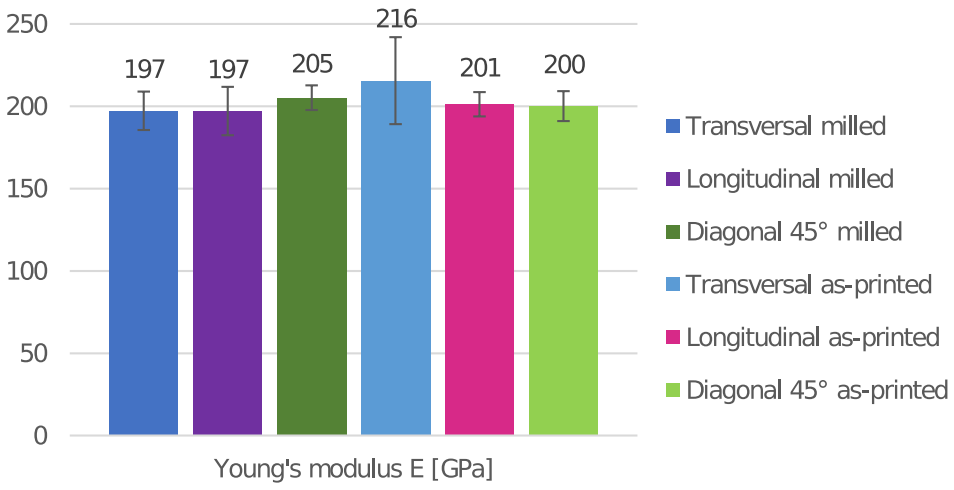

(a) Thin specimens

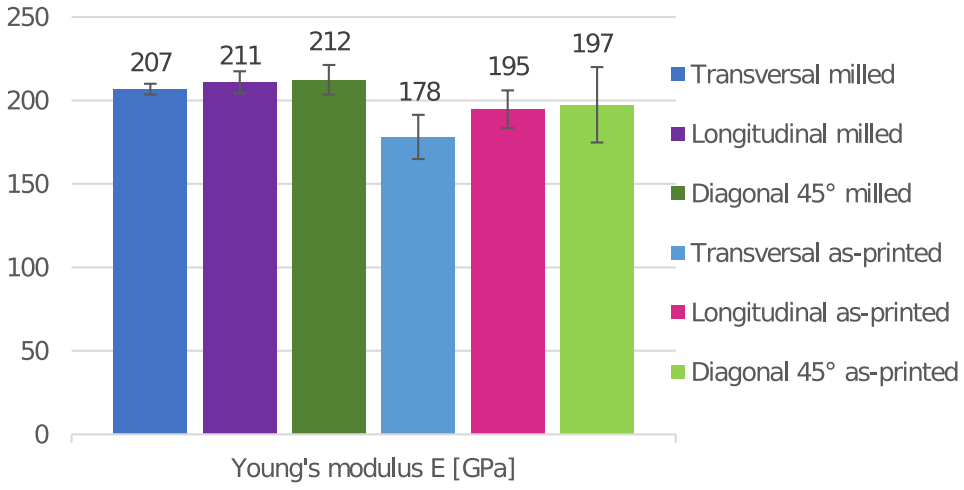

(b) Thick specimens

Figure 4.7: Young's modulus

Summary results tensile tests

One third (20 specimens) of the tensile tests is done on specimens with the printing transversally to the direction of the force. Ten of those 20 were thin and ten were thick specimens. Seven of those ten were tested as-printed and three were milled.
The deformation capacity of the milled specimens has an average of 18%; 17% for the thin and 19% for the thick samples. The highest value of ε_u is found for the longitudinal thick specimens. The thick specimens have a lower yield and ultimate tensile strength than the thin samples for both the milled and the as-printed specimens. The milled samples have a higher yield and ultimate tensile strength than the as-printed specimens.
An average Young's modulus of $200\ GPa$ is obtained.

4.3. Results tear-out strength

Different types of tear-out tests are performed; the same variables as for the tensile coupon tests are used; two different thicknesses, three printing directions (perpendicular, parallel and with an angle of 45° to the force direction), as can be seen in figure 4.8. Additionally, two connection types were used; a bolt and a pin.

The sample name is built up as follows: first a letter that indicates the direction of the welds compared to the direction of the applied force. Secondly, a number is shown, that is the number of the printed object it originates from. The third spot is occupied by an uppercase letter that indicates the specific sample in the object and lastly a dash followed by a number, which is the number of the test on the same sample.

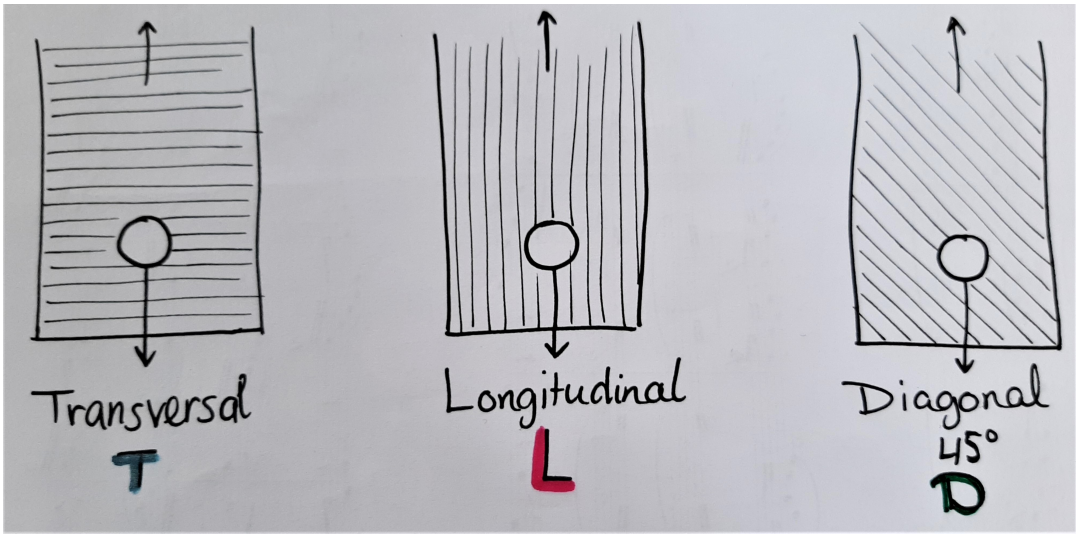

Figure 4.8: Printing directions of tear-out specimens

To make an estimation of the maximum force that is reached during the tear-out test, equation 4.5 is used. More on the effective thickness t_{eff} can be read in section 5.1.4 and about the end distance e_3 in section 2.5.4. The distance that is named e_1' by Kamtekar [38] is in this study called e_3. The experiments of Kamtekar were performed on rolled steel, but it is expected that the same equation for the tear-out strength will hold for WAAM low carbon steel.

$$F_{max} = 2t_{eff}\, e_3\, \frac{f_u}{\sqrt{3}} \tag{4.5}$$

$$e_3 = e_1 - \frac{d_0}{2}\cos(\sin^{-1}(\frac{d}{d_0})) \tag{4.6}$$

4.3.1. Tear-out failure

In figure 3.17a the test set-up for the tear-out test with the bolted connection can be seen. The bolted tests are performed without DIC, as the printed plate is not visible due to the side plates that clamp the printed plate by the bolted connection. In figure 3.17b and 3.18c the test set-up for the tear-out test with the pinned connection can be seen.

In appendix I the force-deformation diagrams of the thick and thin plates can be seen for tear-out failure. The continuous curves show the bolted and the dashed the pinned connections. It should be mentioned that the end distances e_3 of all the plates varied, as can be seen in the tables in appendix H. In figure 4.9 a few tear-out curves are displayed and their end distances can be seen in table 4.5. In figure 3.16 it can be seen that e_1 is the length from the end of the plate till the middle of the bolt hole d_0. In chapter 5, section 5.3, a manner to overcome this inconcise comparison is displayed.

In tables 4.6a and 4.6b the tear-out results of the thin and thick specimens can be seen. The second column shows the ultimate deformation δ in mm, measured by the tensile testing machine. This is the deformation at maximum force, so when the plate has reached the ultimate tear-out strength. The

third column shows the maximum measured tear-out force during the experiment and the fourth the theoretical maximum tear-out force.

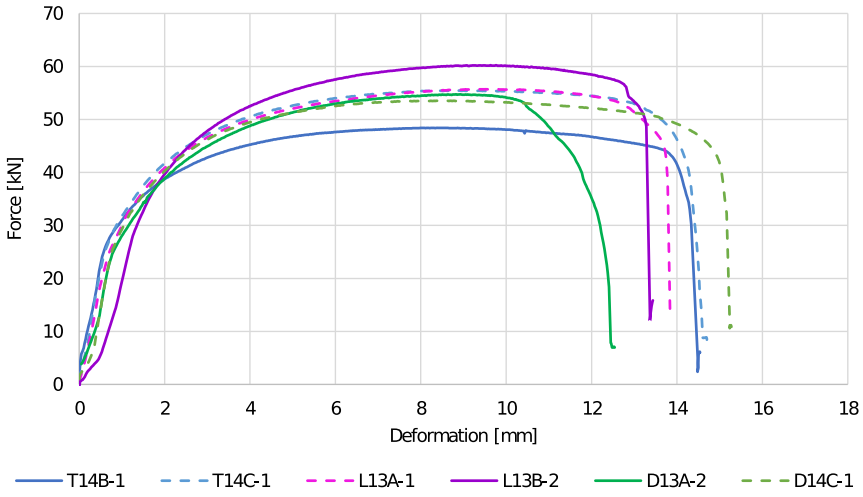

Figure 4.9: Force-deformation curves tear-out thick plates

Table 4.5: End distances e_3 of certain samples

Connection	Sample name	End distance e_3 [mm]
bolt	T14B-1	15.5
pin	T14C-1	18.4
pin	L13A-1	20.0
bolt	L13B-2	20.0
bolt	D13A-2	17.7
pin	D14C-1	17.9

4.3.2. Results connections large end distances

49 connection tests are performed with bolts and pins, of which 45 have an end distance e_1 of $1.2d_0$. Three of the remaining tests are performed on thin plates with a larger end distance of $2.2d_0$. One of these tests is executed on a thin plate with a pin. This plate deformed out-of-plane, so this result is disregarded. The last test is conducted on a thick bolted plate with an end distance of $2.0d_0$. The results can be found in the tables in appendix H in the light grey highlighted rows.

(a) Thin specimens

Sample name	Ultimate deformation δ [mm]	F max experiment [kN]	F max theory [kN]
T10A-1	8.66969	32.1666	28.59
T10A-2	8.89955	31.9365	27.63
T10A-3	8.42298	32.7234	29.54
T10B-1	9.37882	31.6013	29.37
T10C-1	9.32828	29.1966	27.63
T10C-2	10.7068	32.9640	29.11
T10C-3	11.2125	35.8278	31.06
L9A-2	8.25478	29.7283	26.61
L9B-1	7.75658	29.4582	27.34
L9B-2	8.98492	29.3978	26.08
L9B-3	7.33329	30.0813	26.66
L9C-1	8.40262	29.2931	27.13
L9C-2	7.92406	30.3379	28.39
L9C-3	8.62010	30.2516	27.76
D9A-1	9.15846	31.0597	27.01
D9B-1	10.1963	30.1651	27.63
D9B-2	8.64551	30.3408	26.92
D10C-1	8.26009	31.7674	28.06
D10C-2	9.91323	34.5113	29.77

(b) Thick specimens

Sample name	Ultimate deformation δ [mm]	F max experiment [kN]	F max theory [kN]
T14A-1	8.48573	49.4519	43.01
T14A-2	9.00663	52.9956	48.89
T14A-3	11.9481	51.2982	42.35
T14B-1	8.50553	48.4101	41.05
T14B-2	9.16931	49.8093	41.53
T14B-3	9.69718	49.4673	41.23
T14C-1	8.81661	55.4638	50.64
T14C-2	9.78998	59.7189	52.26
T14C-3	9.69494	59.6093	52.01
L13A-1	9.51979	55.6993	57.04
L13A-2	9.67749	54.3446	56.99
L13A-3	9.61024	58.7566	58.44
L13B-1	10.1493	57.4629	57.98
L13B-2	9.63383	60.2450	60.15
L13B-3	10.9418	60.7908	58.52
L13C-1	8.84236	56.4671	49.67
L13C-2	5.23830	48.8929	46.24
L13C-3	5.88919	53.8750	48.83
D13A-1	8.32731	50.4739	48.54
D13A-2	10.7854	54.7412	49.02
D13A-3	9.12628	61.8135	51.07
D13B-1	8.75483	49.6693	50.98
D13B-2	10.8171	53.2843	50.28
D13B-3	8.46637	62.5542	53.47
D14C-1	8.60992	53.5493	49.04
D14C-2	10.7454	58.0253	47.01
D14C-3	9.22768	60.6965	52.34

Table 4.6: Tear-out results: maximum force

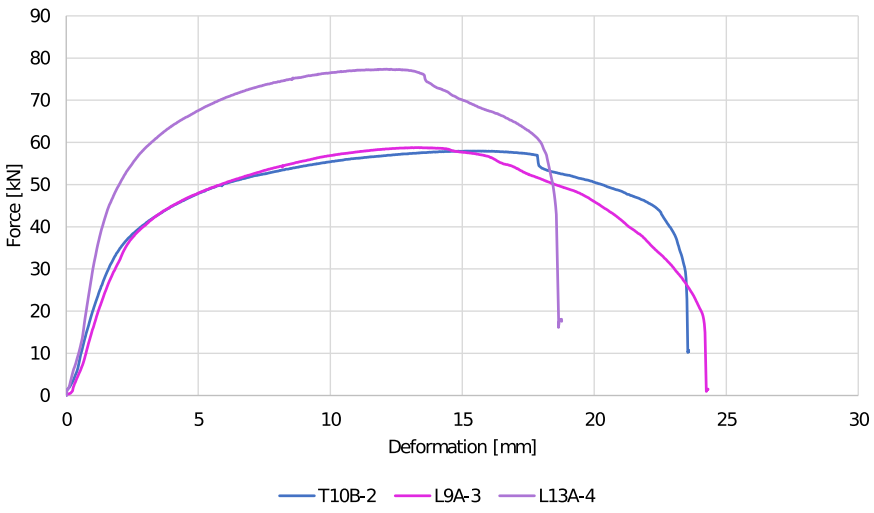

Figure 4.10: Force-deformation curves tear-out with large end distances

Table 4.7: Large end distances e_3 and their maximum force

Thickness	Sample name	End distance e_3 [mm]	$F_{max,\ experiment}$ [kN]	$F_{max,\ theory}$ [kN]
Thin	T10B-2	35.5	57.56	57.84
Thin	L9A-3	45.8	58.78	55.66
Thick	L13A-4	30.2	77.38	86.05

Summary results tear-out tests

The results of the tear-out tests are force-deformation curves. The maximum force of these curves differs due to the printing direction compared to the applied force, the end distance e_3 and the effective thickness of the plate. The ultimate tensile strength of the as-printed tear-out plates depends on the printing direction and deviates from the milled tensile coupons.
The model of Kamtekar is used to calculate the end distance e_3 for the engineering method for the maximum tear-out force F_{max}. The maximum experimental tear-out values are displayed, together with the theoretical and the ultimate deformation.
The three results of the large end distances are shown separately from the small end distances.

5

Analysis of results

5.1. Analysis tensile test results

In this section the results of the tensile coupon tests will be analysed; the results will be compared and the reasons for the behaviour of the WAAM carbon steel will be described. An effective thickness is derived by taking the results of the milled specimens as the basis.

5.1.1. Analysis stress-strain diagram results

The stress-strain diagrams that resulted from the tensile coupon tests follow the same trend as conventionally produced carbon steel; it starts with a linear elastic part, then a pronounced yield plateau can be seen, whereafter the strain hardening starts and the plastic deformation with the increase and then decrease in stress after the ultimate stress is reached until failure of the cross section. This development can be seen in figure 5.1.

The upper yield stress of every specimen is determined as follows: the peak after the linear elastic part in the stress-strain curve, so the upper yield point after which a decrease in stress can be seen, is taken as the upper yield stress and noted as f_y. Not all specimens have such a clear peak, as can be seen in section 4.2 and figure 4.2b. The longitudinal had a distinguishable peak and the diagonal specimens had a gently decreasing slope. The highest point of this part of the curve was taken as yield strength. For the transversal specimens a very round transition from the linear elastic to the yielding part was observed. The value after the linear elastic part was taken where the increase in value was close to zero.

The ultimate tensile stress is determined by noting the highest stress f_u in the region where plastic deformation occurs, which is also the highest overall stress. As the engineering stress is measured and not the true stress, there is a decrease in stress after the highest point f_u.

From the linear elastic part of the stress-strain curve, the Young's modulus E can be resolved by equation 5.1. The lower and upper part of the linear curve are not taken into account, as some irregular parts are measured at the beginning and end of this curve. As an example the graph of figure E.2b is taken; the Young's modulus is determined by a line at the stress part between 50 and $300\ MPa$. The a in the equation for this line $y = ax + b$ indicates the value for the Young's modulus, as this is the inclination of the line.

$$E = \frac{f_E}{\varepsilon} \tag{5.1}$$

The amount of deformation is expressed on the x-axis, as is explained in section 4.2.1. In figure 5.1 this is indicated with a δ.

The results of the extra tensile tests are compared to the tests that were performed earlier; graphs are shown in figure 4.4a and 4.4b. They show good agreement.

The deformation capacity (strain at rupture) of the extra samples is more scattered than was the case for the first tests.

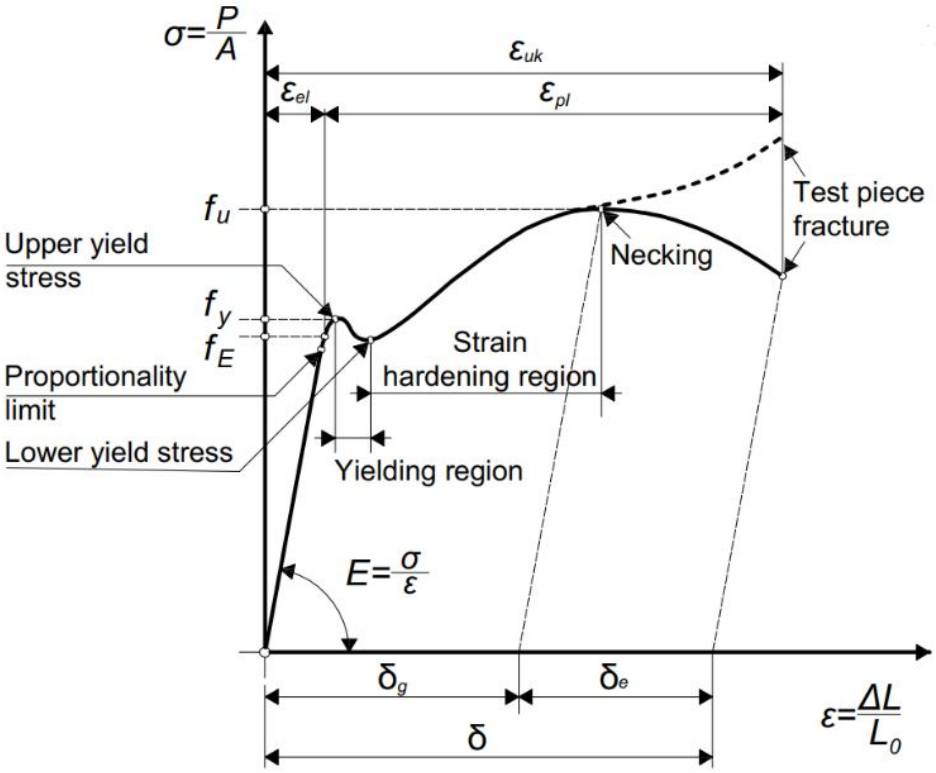

Figure 5.1: General stress-strain diagram with yield plateau [28]

5.1.2. Analysis milled versus as-printed results

As can be seen in the boxplots in figures 4.5, 4.6 and 4.7 the yield, ultimate tensile strength and Young's modulus are higher for the milled samples than for the as-printed, except for the Young's modulus of the thin samples. This can be due to the surface roughness, as the surface of the milled specimens is smooth; no waviness can be seen by the naked eye, so the whole area is used to distribute the applied force. In contrary to the as-printed samples; the outer area for the force distribution exists of wavy parts, that are partly used, so the force is not distributed optimally.

Another fact can be noticed; the yield and ultimate tensile strength are higher for the thinner specimens. This can be caused by the high surface roughness for the thick specimens, compared to the thinner specimens.

This is not the only reason for the difference in strength, as this difference is also seen in the milled coupon results. The printing parameters also have an influence. When the travel speed is high and/or when the wire speed is low, low arc power is needed and a small amount of material is deposited. This means that the object is cooling down quite fast, as there is less heat that needs to travel from the molten pool into the object and down to the substrate. The smaller the heat input, the finer the grains of the microstructure and the more the hardness increases [73]. A high hardness value causes a lower ductility, so a more brittle fracture. More on this subject can be read in section 2.3.2.

Therefore the thicker specimens are expected to be more brittle than the thin samples. The ductility is expressed in the amount of strain which is shown in percentage in the stress-strain diagrams. When comparing the thin as-printed curves F.1 with the thick curves F.2, it can be seen that the ultimate strain (ε_u), so the strain at ultimate tensile strength f_u, for the thin samples is equally spread around $17 \pm 5\%$. For the thick milled samples however, this spread is not that even: $19 \pm 12\%$. This is due to the transversal specimens that have a significantly lower ultimate strain ε_u than the longitudinal and diagonal samples. This last observation also holds for the as-printed specimens.

This could be due to the fact that the transversal welds are more susceptible to strains. Only one weld bead, which is also a short bead, needs to be the weakest in order to let the whole specimen collapse. The welds of the longitudinal samples "cooperate"; they are parallel to the direction of the force. A weak weld in this specimen does not cause a total failure.

It can be stated that all tests, thin, thick, milled and as-printed, fulfil the ductility requirements in equations 4.2, 4.3 and 4.4, as explained in section 4.2.7.

5.1.3. Minimum thickness analysis and roughness indication

As explained before; the roughness of the specimens has an influence on the strength of the carbon steel. The yield strength of a sample that consists of weld beads on top of each other is lower when compared to only one weld bead made of the same rod. In Appendix A a yield strength of at least $460\ N/mm^2$ is one of the mechanical properties of the as-welded rod. This low value for the yield strength is explained in section 2.3.2 by the microstructural influence.

This observation means that another value for the design calculations of WAAM low carbon steel must be used. A reduction factor is a way to incorporate this decreased strength of the material.

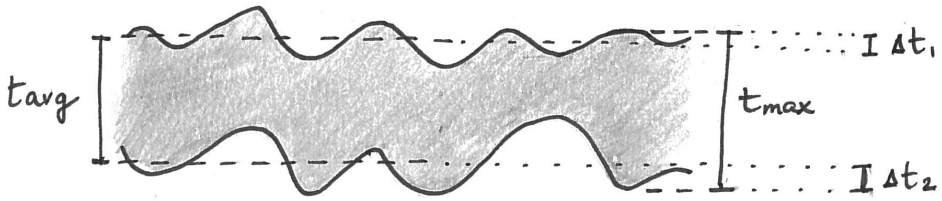

Figure 5.2: Dimensions of thickness for calculations

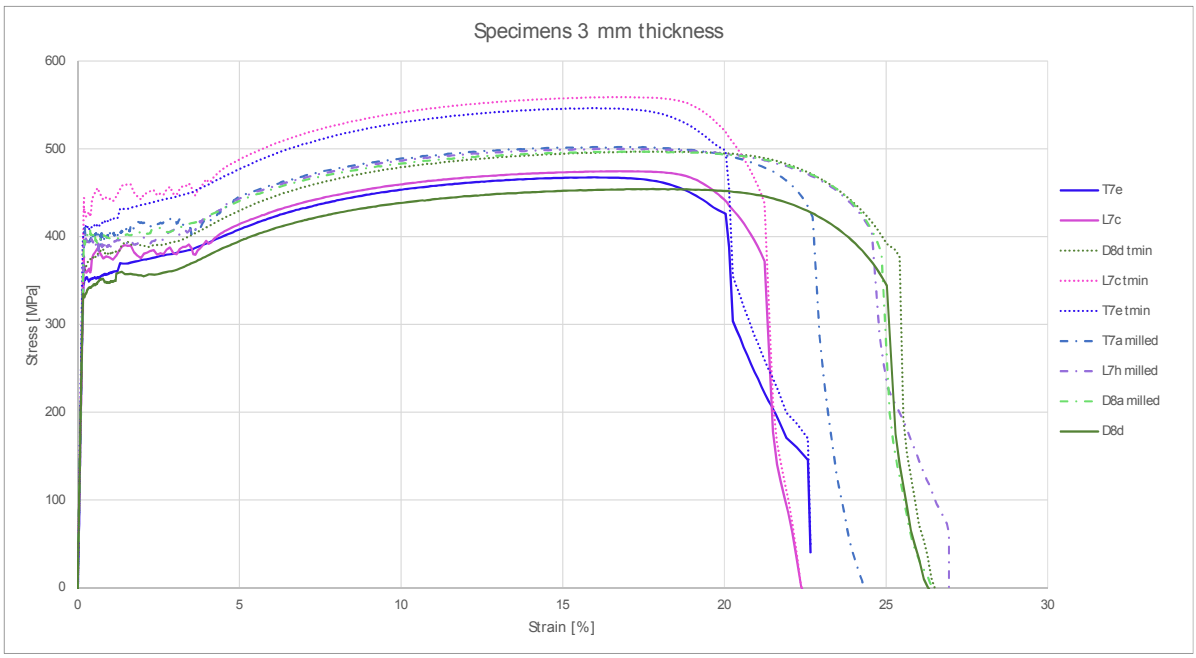

Figure 5.3: Stress strain curves for thin as-printed t_{min}, milled and as-printed t_{avg} specimens

When the surface roughness of the as-printed specimens is eliminated, as is done by milling, higher stress values are found. Those values are lower than a single weld by the same material, Carbofil 1A. A second check is done on the influence of the roughness by not only comparing the stress-strain diagrams of the milled with the as-printed specimens, but also by using a the minimum thickness t_{min} of the as-printed specimens. How t_{min} is calculated can be found in equation 5.2. t_{avg} is measured by the Archimedes' principle, about which can be read in section 3.4.1. t_{max} is measured by a calliper, this is an average value of the maximum thicknesses. These two outcomes mean that the printing process produces a material of weld beads that has irregularities and imperfections.

When the minimum thickness t_{min} is used to calculate the stress of the as-printed tensile coupons, instead of the average thickness t_{avg}, an increase in stress can be seen, as the area reduces (equation 3.7). These values of the stress are even higher than the values of the milled specimens for

the transversal T and longitudinal L specimens, as can be seen in figure 5.3. For the diagonal D specimens the milled curve is similar to the curve of t_{min}.

$$t_{min} = t_{avg} - \Delta t \tag{5.2}$$

$$\Delta t = \Delta t_1 + \Delta t_2 = t_{max} - t_{avg} \tag{5.3}$$

$$\zeta = \frac{t_{avg}}{\mu_{\Delta t}} \tag{5.4}$$

So, not only a reduction of the material strength due to the roughness by the limited effective thickness must be taken into account, but the strength must also be reduced due to the material built-up; layer by layer, that causes a surface roughness.

This is the reason that in the next section (5.1.4) an effective thickness is determined, that takes into account the surface roughness and difference in strength for multiple types of specimens.

To have an idea about the difference in surface roughness between the thin and thick specimens, a roughness indication is given in tables 5.1 and 5.2. More in-depth theory on the surface roughness is explained in section 2.4.3. Δt calculated according to equation 5.3. In appendix G the full tables are shown; the standard deviation σ, coefficient of variation V and Standard Error of the Mean (SEM) of Δt are determined. In tables 5.1 and 5.2 the mean value of Δt, the average thickness t_{avg} and in the last column ζ is shown; the mean value of Δt as a function of the average thickness, according to equation 5.4.

It can be seen that the roughness for the thick specimens is bigger than for the thin specimens, as was expected. Even if the thickness is eliminated, so when ζ is regarded, a higher value for the thick samples is found. No conclusion can be drawn from the different factors for the three printing directions, as the variation is not constant between the two thicknesses.

Table 5.1: Thickness variation for roughness indication thin specimens

Printing direction	$\mu_{\Delta t}$ **[mm]**	t_{avg} **[mm]**	ζ **[-]**
Transversal	0.331	2.64	0.125
Longitudinal	0.392	2.63	0.149
Diagonal 45°	0.272	3.03	0.0898

Table 5.2: Thickness variation for roughness indication thick specimens

Printing direction	$\mu_{\Delta t}$ **[mm]**	t_{avg} **[mm]**	ζ **[-]**
Transversal	1.28	5.890	0.218
Longitudinal	1.11	5.936	0.187
Diagonal 45°	1.09	6.013	0.181

5.1.4. Effective thickness and reduction factor determination

There is a difference in effective cross-sectional area between the milled and as-printed samples. This is caused by the surface roughness of the as-printed specimens. For the milled samples the area is determined easily, where for the as-printed, this is difficult due to the irregular surface. Therefore, the milled samples are taken as base for the determination of the effective thickness of the as-printed samples.

Equation 3.7 for stress is taken as origin to determine the effective thickness t_{eff} in equation 5.5.

$$t_{eff} = \frac{F_{max,as-printed}}{f_{u,milled}\, w_{as-printed}} \tag{5.5}$$

An effective thickness is determined for the three different directions of the welds and for the two different thicknesses; see table 5.3 for the thin and table 5.4 for the thick specimens. The values for $F_{max,as-printed}$, $w_{as-printed}$ and $f_{u,milled}$ are the average values of the tests. For the as-printed values, this consists of five results and for the milled of three, as this was the amount of samples tested.

Table 5.3: Effective thickness t_{eff} thin specimens

Printing direction	**$F_{max,\ as\text{-}printed}$ [kN]**	**$w_{as\text{-}printed}$ [mm]**	**$f_{u,\ milled}$ [MPa]**	**t_{eff} [mm]**
Transversal	14.63	12.57	511	2.28
Longitudinal	14.82	12.47	499	2.38
Diagonal 45°	17.29	12.56	484	2.84

Table 5.4: Effective thickness t_{eff} thick specimens

Printing direction	**$F_{max,\ as\text{-}printed}$ [kN]**	**$w_{as\text{-}printed}$ [mm]**	**$f_{u,\ milled}$ [MPa]**	**t_{eff} [mm]**
Transversal	29.84	12.57	466	5.05
Longitudinal	31.55	12.31	463	5.54
Diagonal 45°	30.76	12.56	468	5.23

An adequate analysis on the effective thickness of the different specimens can be performed when this is compared with the average thickness, measured by the Archimedes' principle, on which everything is explained in section 3.4.1. This is due to the fact that not all samples have the same thickness. This can be seen in the last column of table 5.3; the effective thickness of the diagonal sample is 20% higher than the other two. The average thickness of these samples is also 20% higher, as can be seen in table 5.5.

The number for the difference between the effective and average thickness, shown in the last column of these tables (5.5 and 5.6), can also be regarded as a **reduction factor**; the reduction in thickness that has to be made when the effective thickness is considered instead of the measured average thickness. With the comparison made in tables 5.5 and 5.6 the following can be concluded:

I The thicker the specimen, the bigger the reduction factor, due to the high surface roughness.

II The transversal specimens have the larger reduction in thickness, then the 45 ° and lastly the longitudinal specimens. This is the same sequence as the surface roughness for the different printing directions; the transversal specimens have the largest surface roughness.

III The longitudinal specimens have the same reduction factor for the two different thicknesses. A reason can be that they have the smallest surface roughness of the three printing directions.

Table 5.5: Effective and average thickness thin specimens

Printing direction	**t_{eff} [mm]**	**$t_{average,\ as\text{-}printed}$ [mm]**	**t difference [%]**	**Reduction factor [-]**
Transversal	2.28	2.51	9.51	0.90
Longitudinal	2.38	2.52	5.42	0.95
Diagonal 45°	2.84	3.06	7.29	0.93

The reduction factors are used to determine the effective thicknesses of the tear-out plates, as those have another thickness than the tensile coupons, as they originate from other printed objects. To determine the tear-out strength, as is done in section 5.3, this effective thickness is needed for the calculation, as well as the ultimate strength f_u. This is now the same for the milled as for the as-printed specimens.

Table 5.6: Effective and average thickness thick specimens

Printing direction	t_{eff} [mm]	$t_{average,\ as\text{-}printed}$ [mm]	t difference [%]	Reduction factor [-]
Transversal	5.05	5.83	14.1	0.86
Longitudinal	5.54	5.88	5.92	0.94
Diagonal 45°	5.23	6.01	13.8	0.86

5.1.5. Analysis stress drop at failure

A sudden drop in stress can be seen when the specimen fails, at the stress-strain diagrams of the milled samples in the figures in appendix F, especially the curves in figure F.2b. This sudden drop caused by the failure of the whole cross section. When a more gradual line is seen, the specimens cross section is failing part by part; at some spots the upper part stays connected with the lower part, most of the time this involves the edges. As the as-printed specimens decrease gradually after failure and the milled do not, in particular for the thick samples, this indicates that a high surface roughness has an influence on this behaviour.

The thicker the weld beads, the thicker the local cross section, so the more force and therefore the more stress can be applied on this cross sectional spot in a later stadium, such as after failure, but before the whole specimen collapses. Necking before failure happens more visibly at the longitudinal specimens, as they have a larger elongation before failure for example.

The displayed stress-strain curves are the engineering curves. This means that in practice, the material fails differently; when the maximum stress is reached. The tests are displacement-controlled, so the displacement is constant during testing. A structure or connection failure is force-driven in reality. So, these engineering curves with their sudden drop are for designing purposes only.

5.1.6. Results DIC tensile specimens

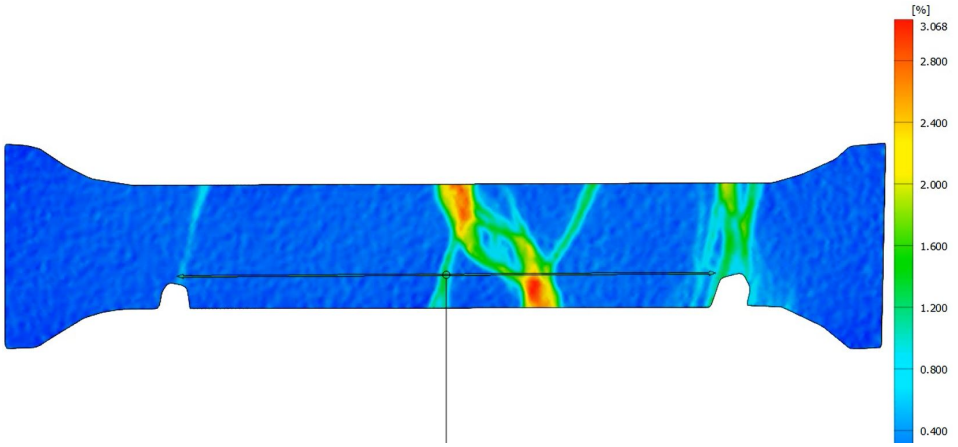

(a) First stage

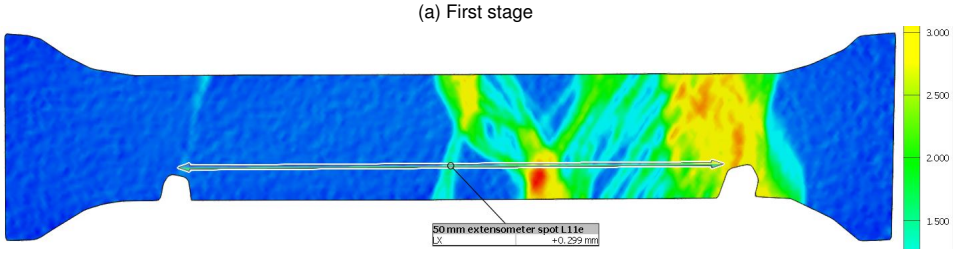

(b) Second stage

Figure 5.4: DIC image milled longitudinal tensile coupon: major strains

In section 3.5.4 the purpose of Digital Image Correlation is explained. In this section the milled WAAM tensile coupons are compared with the as-printed. As can be seen in figure 3.2 two as-printed

tensile samples per printing direction are measured by DIC; these are orange coloured.

In figure 5.4 the major strain development in a milled longitudinal tensile coupon can be seen. The scale indicates the strain in percentage. The force is applied in horizontal direction, so parallel to the printing direction. The strains develop perpendicular to the direction of the welds.

Two small areas are left out of the analysis. This is due to the clamps of the extensometer, combined with their shadows caused by the flash that was needed for clear and accurate photos. In this way the small black dots could be easily distinguished from the white background by the GOM correlate software.

Halfway the test, the strains are displayed in figure 5.4b and the development is at an angle of 45°. This is due to the shear forces, as explained in the section concerning the microstructural behaviour; in the part about slip 2.3.2. The red dot in the lower part of the specimen indicates high strains. The specimen will fail in between the two strain concentrations (red spots), seen in figure 5.4a. A rolled carbon steel specimen shows a very homogeneous strain distribution, with only maximum strains at the spot where failure will occur.

In figure 5.5 a longitudinal as-printed tensile coupon is seen. The spots indicate typical local strains on the surface of the welds. The as-printed tensile coupons show different DIC results from the milled. The original idea was to localise the strains and the failure area which could be compared to the 3D scans that were made. More on 3D scanning can be read in section 3.4.2 and some scans can be seen in section 5.2.1. Via the 3D scans one could see if the sample failed in a spot where the thickness was minimal. If this hypothesis would not hold, an irregularity might have been the cause for the failure location. The made 3D scans were not sufficient for this analysis, so the DIC data can be used for follow-up research.

The difference in results of the milled and as-printed tensile coupons showed that the as-printed DIC results are not usable, because the as-printed do not display the strains correctly. Therefore, the DIC results of the as-printed tear-out specimens are not further analysed than in appendix K.2. A manner to overcome this problem is to mill the tear-out specimens when DIC is used.

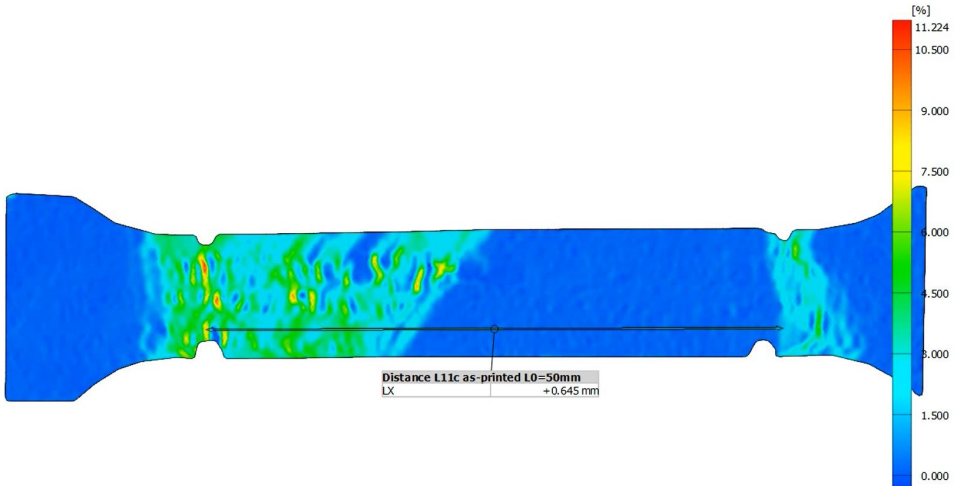

Figure 5.5: DIC image as-printed longitudinal tensile coupon: major strains

Three specimens, of all three printing directions, are displayed in figure 5.6 to compare the displacements measured by the extensometer (more on this can be read in section 3.5.3) and DIC. The time is in seconds, as the photo count of the DIC was also calculated in seconds. The y-axis shows the strain, according to equation 3.8; for the extensometer the initial length L_0 equals $50mm$ and for the DIC this is a value of $50 \pm 2mm$, depending on the measured length inserted in GOM correlate. As can be seen, the dashed DIC curves have a good fit with the continuous extensometer curves.

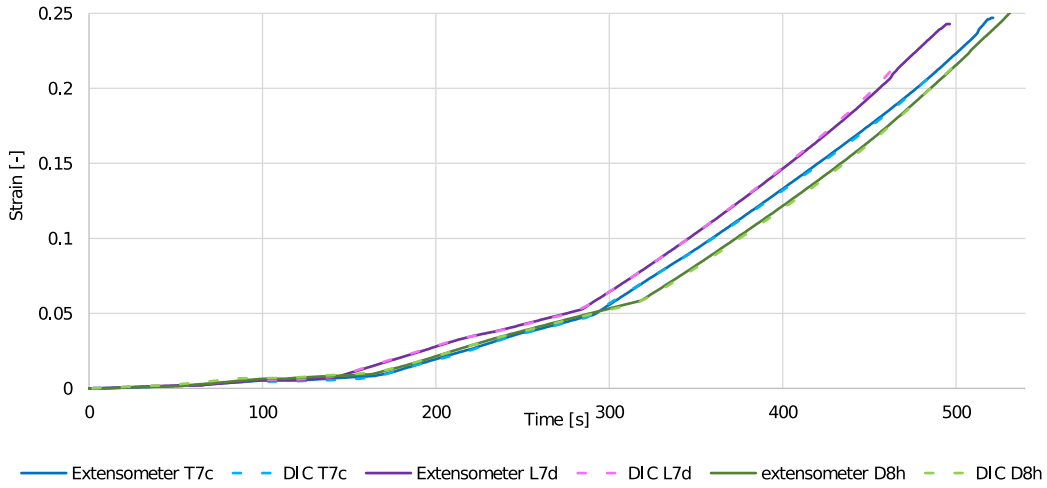

Figure 5.6: Comparison DIC with extensometer results of thin as-printed specimens

Summary analysis results tensile tests

The stress-strain curves of the tensile tests are very similar to the stress-strain curves of conventionally produced carbon steel. A high ductility is observed; ultimate strains ε_u with an average of 17% for the milled samples. Furthermore, the printing direction has a small influence on the strength of the WAAM steel. The surface roughness has an influence on the strength as well. This effect is bigger when the printed plate is thicker.
Reduction factors are determined via effective thickness computations to make proper design calculations for as-printed carbon steel objects; for thin and thick plates and for the three printing directions. The results of the milled tensile coupons are taken as the basis for this determination.
The DIC results have good agreement with the extensometer results. However, the strain developments that are observed via DIC of the as-printed tensile coupons differ from the milled samples; very local strains on the irregular surface are detected as spots. Therefore, the DIC results are not further evaluated.

5.2. Analysis 3D scans

To make an analysis of the surface roughness, 3D scans are made with the Artec Spider hand scanner. More on this scanning method can be read in section 3.4.2. A scan of one of the plates for the tear-out test can be seen in figure 5.7a; this is a thick plate with the welds horizontally, so in transversal direction.

5.2.1. 3D scan analysis for roughness different printed thick objects

The tear-out specimens were cut out of other printed objects than the tensile coupons, as can be seen in figures 3.2, 3.3, 3.4 and 3.5. The same print process parameters were used to make the thick objects and the thin objects. However, the surface roughness might differ, so this is studied by comparing the 3D scans of thick samples.

The material properties that were discovered by doing the tensile tests, as can be read in section 5.1, are needed for the analysis of the tear-out tests, specifically the ultimate strength f_u and the effective thickness t_{eff}.

In 3.4.2 it can be read how sections in the sample are made. The perimeter is calculated by the Artec Studio software by the x-, y- and z-coordinates of the sections. In figure 5.7 the tear-out plate and tensile coupon can be seen with their transversal sections, so parallel to the printing direction. The mean perimeter P_{mean} is calculated with these 40 sections.

To be able to compare the two plates, the width w_{sr} that includes the surface roughness, so all the highs and lows, is determined by equation 5.6. This width w_{sr} is different from the average width w, measured by the calliper. The average thickness t_{avg}, obtained by the Archimedes principle (section 3.4.1), is used. The w_{sr} differs for both plates; for the tear-out the value very near the value of w of the tear-out sample; $65\,mm$. And for the tensile coupon this is $12.6\,mm$.

$$P_{mean} = 2t_{avg} + 2w_{sr} \tag{5.6}$$

This difference in length is compensated by the **width factor**, as can be seen in table 5.7 in the fourth column; the wider the section of the tear-out sample $w_{tear-out,mean}$, the higher this factor. The width of the tensile specimen $w_{tensile,mean}$ was for every sample around $12\,mm$, as can be seen in the third column.

$w_{tensile,mean}$ is multiplied by the width factor, so a new width of the tensile coupon is obtained. This new width is compared with $w_{tear-out,mean}$ and the last column of table 5.7 is calculated; the difference in surface roughness between the samples that originate from different printed objects.

This calculation is also done for the other two printing directions; longitudinal and diagonal (45°). For the first three comparisons in table 5.7 the same tear-out plate is used. Only different perimeter lines are drawn, as can be seen in figure 5.8a and 5.8b. The last result, called "Diagonal 2 45°", is a different plate (figure 5.8c), where the welds itself are under an angle of 45°, instead of the drawn perimeter lines.

The deviation in roughness of the samples from different objects, as can be seen in the last column of table 5.7, has a maximum of 8%, which is significantly low, that it can be stated that the different printed objects have the same roughness. This means that the same reduction factor, as calculated by the tensile coupon tests (section 5.1.4), can be applied for the determination of the effective thickness for the tear-out samples.

Table 5.7: Roughness different printed objects

Printing direction	$w_{tear-out,\,mean}$ [mm]	$w_{tensile,\,mean}$ [mm]	Width factor [-]	Deviation roughness objects [%]
Transversal	64.88	11.88	5.193	4.916
Longitudinal	206.3	12.61	15.84	3.236
Diagonal 1 45°	96.23	12.03	7.356	8.035
Diagonal 2 45°	62.28	12.03	5.177	5.327

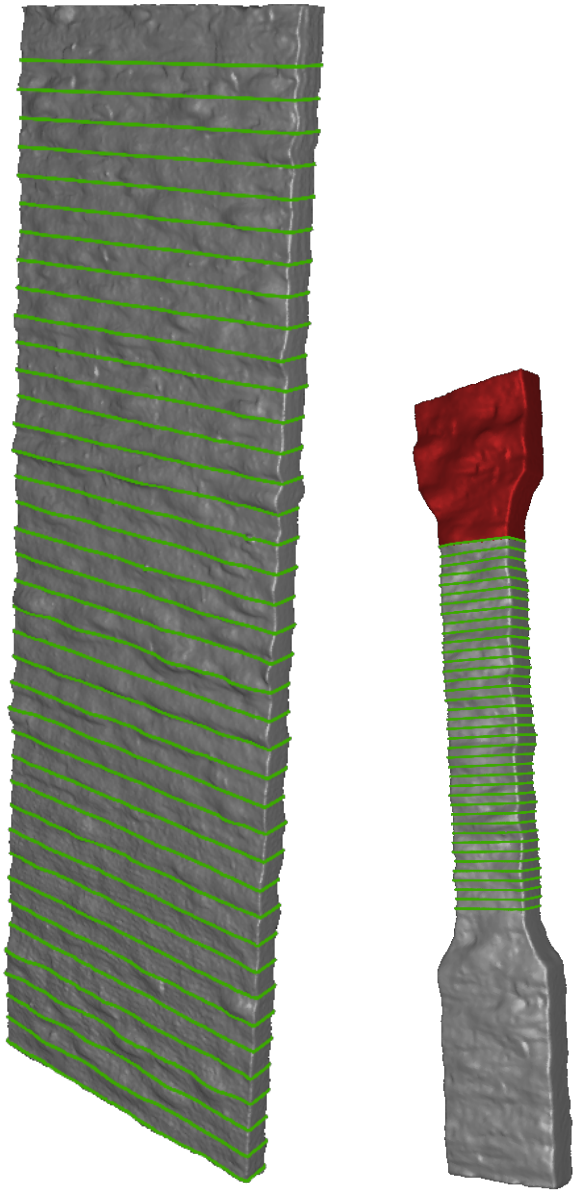

(a) Tear-out plate (b) Tensile coupon

Figure 5.7: 3D scans with sections to measure perimeter of transversal plates

5.2.2. 3D scan analysis for surface roughness determination

A surface roughness could be determined by the 3D scans. This appeared a more difficult than expected. Especially with the limited amount of scans that was made. A better indication on the surface roughness is given by the effective thickness, as is determined in section 5.1.4. The difference in average and effective thickness is a indication of the surface roughness, as can be read in last part of section 5.1.4.

In practice, the determination of the thickness, average, maximum, minimum or effective, is difficult, due to the surface roughness. One of the methods is 3D scanning, others are taking measurements of the surface by a profilometer or using a Scanning Electron Miscroscope (SEM). When 3D scanning, measurements can be done, such as perimeter (as in section 5.2.1) or area measurements by taking sections of the scanned sample.

A profilometer uses a stylus or laser to measure the profile of the surface. The average roughness profile R_a can be measured by equation 5.7. The unit of R_a is μm and it classifies the surface of objects of the same material that are produced similarly [20].

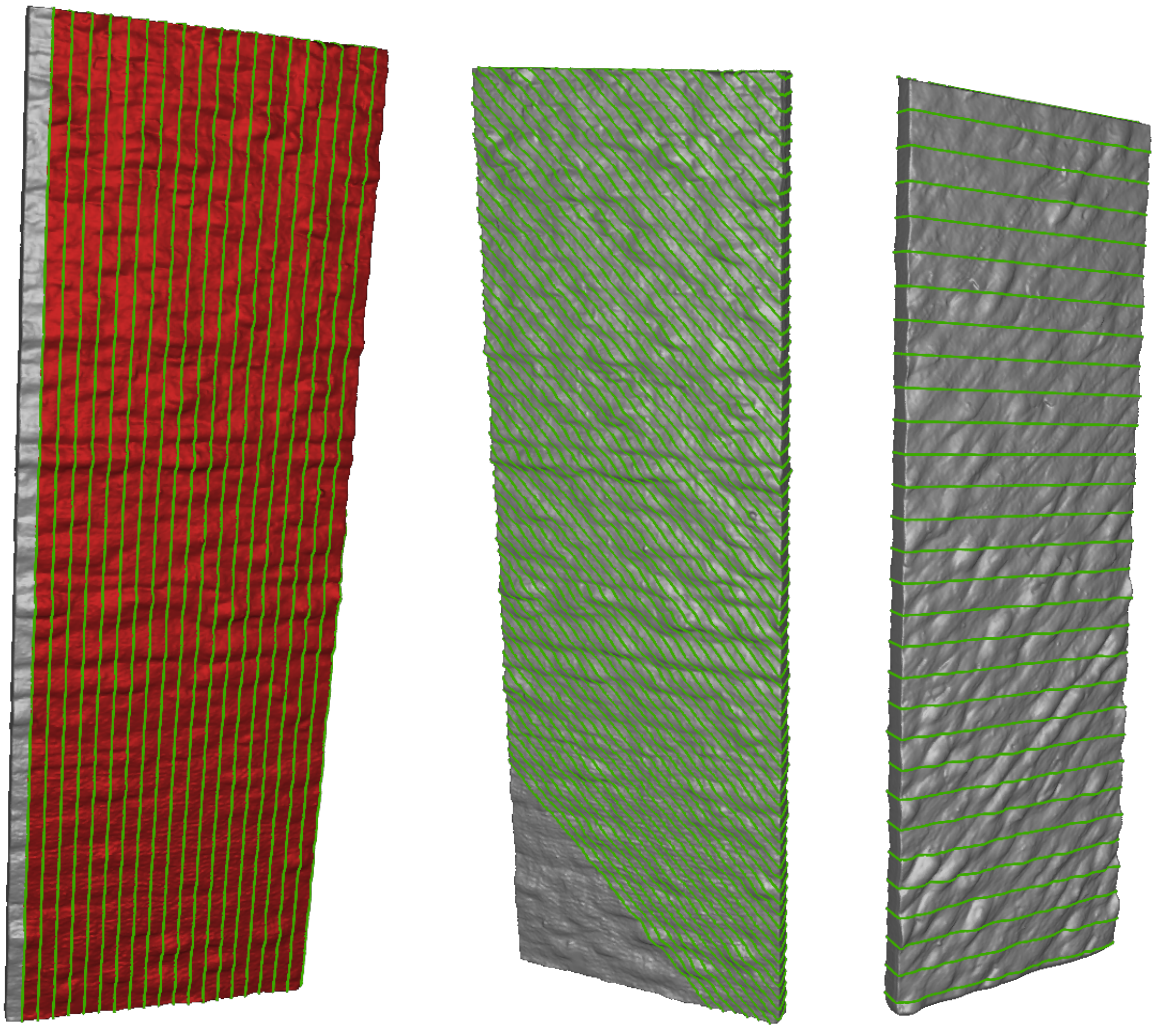

(a) Longitudinal (b) Diagonal 1 (c) Diagonal 2

Figure 5.8: 3D scans of tear-out plates with sections to measure perimeter

$$R_a = \frac{1}{n}\sum_{i=1}^{n}|y_i| \tag{5.7}$$

Where:
n = number of measurements
y_i = measured height

Summary analysis results 3D scans

The reduction factor, calculated by the effective thickness determination from the tensile coupons tests, can also be applied on the tear-out samples to determine their effective thickness. The 3D scan analysis pointed out that the roughness of the different printed objects was similar. Thus, the obtained reduction factors for the effective thickness can be also applied to the tear-out samples.

5.3. Analysis tear-out tests

In this section the results of the tear-out tests are analysed; mutually, so the three printing directions and the two thicknesses are compared. This is done by normalisation. The bolt and pin tests are combined and a statistical evaluation is done to come up with a design factor γ.

5.3.1. Normalisation tear-out tests

The outcome of the tear-out tests are force-displacement curves, as can be seen in chapter 4, section 4.3. In order to compare the outcomes of the tests, normalised curves are made, to eliminate the variables.

The force and the deformation are normalised, as can be seen in equation 5.8 and 5.10. The equation for the normalised force comes from the shear planes as shown in figure 2.13. According to Huber-Hancky, equation 5.9 holds, when normal stresses are set to zero.

$$F_{normalised} = \frac{F_{measured}}{2t_{eff}\, e_3\, \frac{f_u}{\sqrt{3}}} \tag{5.8}$$

$$\tau_u = \frac{f_u}{\sqrt{3}} \tag{5.9}$$

Where:
$F_{measured}$ = Force measured by the Instron machine [N]
$t_{average}$ = Thickness measured by the Archimedes' principle [mm]
e_3 = End distance [mm]
f_u = Ultimate strength [MPa]; material property determined by milled tensile coupon tests
τ_u = Shear stress [MPa]

$$\delta_{normalised} = \frac{\delta_{measured}}{d} \tag{5.10}$$

Where:
$\delta_{measured}$ = Deformation measured
d = Diameter of the bolt or pin [mm] = 16

In appendix J the normalised graphs for the tear-out failure can be seen.

For both thicknesses and connection types, bolted and pinned, it can be said that the transversal specimens T can resist the highest force. The longitudinal samples are weakest, compared to the transversal and diagonal. This can be seen in the normalised graphs (in appendix J); the normalised force on the y-axis is lowest for the longitudinal samples.

This distinction in maximum force can be explained as follows: the welds of the transversal specimens are cooperating. All the welds are pressed together and act as one. Whereas the welds of the opposite, the longitudinal specimen, are not collaborating; when a weak weld is discovered near the shear plane underneath the bolt or pin, the connection is likely to fail in this spot. Another reason could be that the longitudinal specimen fails at one of the valleys in between the welds, as the shear surface is limited in this area. Pictures of failed transversal and longitudinal plates can be seen in 5.9.

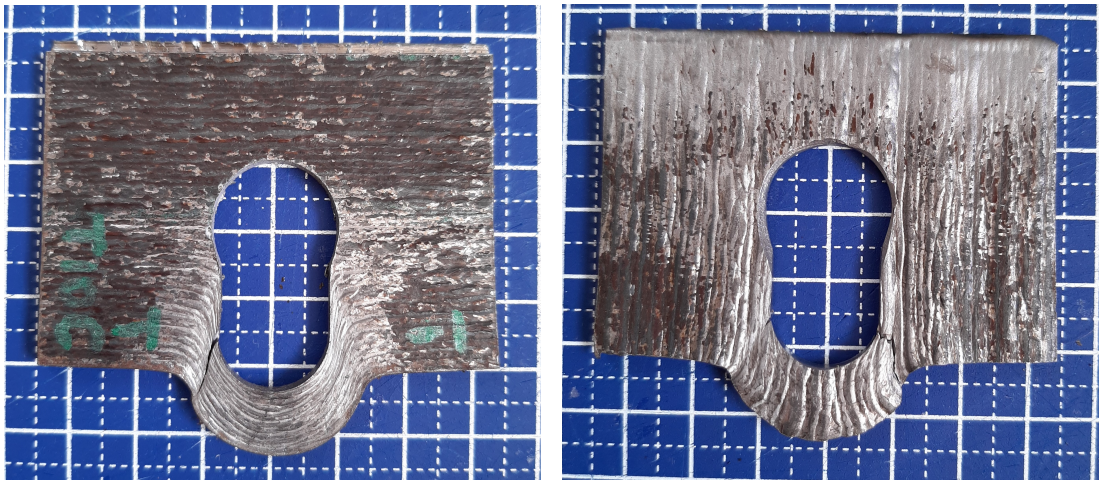

(a) Transversal pin (b) Longitudinal bolt

Figure 5.9: Tear-out failure thin plates

5.3.2. Tear-out experiments; bolt and pin agreement

Normally, when tear-out tests are performed, a bolted connection is used. This time, not only bolted, but also pinned connections are used, for reasons named in section 3.6.1. As little is known on the behaviour of pinned connections, a comparison of these results with the tear-out results of bolts is made when the diagrams are normalised, as explained in section 5.3.1. No significant difference can be seen in the curves between the pinned and bolted connection, as can be seen in the diagrams in appendix J; the continuous curves indicate the bolted connections and the dashed the pinned.

In the tables in appendix H.2 or table 5.8, where the summarised values are displayed, the bolted connection results are compared with the pinned. A maximum difference Δ of 5.34% is seen. This is a positive value, so the mean normalised force of the bolted connection is higher than the pinned. The bolted connection is namely taken as the basis, as tear-out tests are normally performed with bolts instead of pins.

The nut of the bolt was not tightened such that a large force was applied on the three plates, in order to exclude the friction forces. This is a reason that the bolted connection was very similar to the pinned, as was intended. The small differences Δ indicate that the results of bolted and pinned connection can be regarded similarly and are therefore displayed in the same diagram.

Table 5.8: Bolt pin agreement

Printing direction	**Δ thin bolt versus pin [%]**	**Δ thick bolt versus pin [%]**
Transversal	4.65	5.34
Longitudinal	-1.81	-2.81
Diagonal 45°	1.16	-1.09

5.3.3. Statistical evaluation tear-out tests

The maximum force of the experiment F_e of every tear-out sample is compared with the expected outcome, according to the theory, for the maximum force F_t. F_e is measured by the tensile testing machine and F_t is calculated by equation 4.5. The values of the tear-out test samples can be found in appendix H.

To visualise the deviation of the experimental from the theoretical results, diagrams with F_t on the x-axis and F_e on the y-axis are plotted. When these results would be exactly the same, they would lie in the middle; on the dashed line with an angle of 45° to the origin.

The following equations are used to calculate the deviation $\bar{b}$ of the experimental from the theoretical results [49].

$$b_i = \frac{F_{e,i}}{F_{t,i}} \tag{5.11}$$

$$\bar{b} = \frac{\sum_{i=1}^{n} b_i}{n} \tag{5.12}$$

$\bar{b}$ in equation 5.12 is more than 1 for every tested type (thin, thick, transversal, longitudinal, diagonal), as is displayed in table 5.9, which means that the used model, according to the theory, is conservative, compared to the experimental tests. In the graphs in figure 5.10 and 5.11 this can be seen by the fact that the majority of the results is above the 45° dashed line. A slightly conservative model means that it is on the safe side, which is desired.

Table 5.9: Deviation $\bar{b}$

Printing direction	**Thickness**	b
Transversal	thin	1.12
Longitudinal		1.10
Diagonal 45°		1.13
Transversal	thick	1.16
Longitudinal		1.03
Diagonal 45°		1.12

• indicates bolted connections in figure 5.10 and 5.11
○ indicates pinned connections in figure 5.10 and 5.11

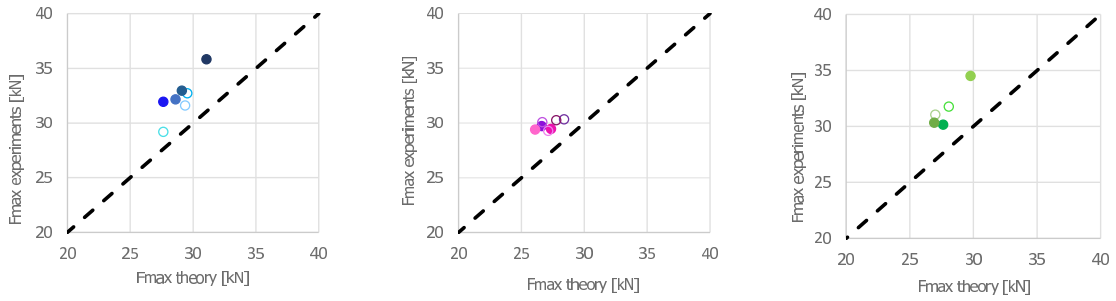

(a) Transversal (b) Longitudinal (c) Diagonal

Figure 5.10: Thin tear-out theoretical versus experimental results. • indicates bolted and ○ pinned connections

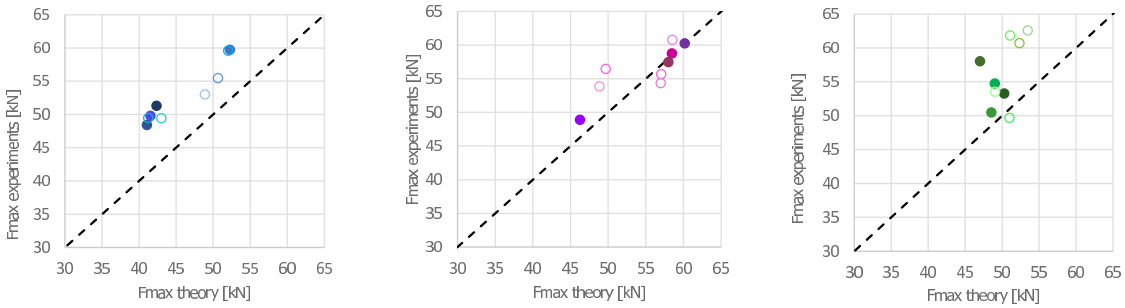

(a) Transversal (b) Longitudinal (c) Diagonal

Figure 5.11: Thick tear-out theoretical versus experimental results. • indicates bolted and ○ pinned connections

The theory-experiment plots of rolled carbon steel, when the same model is used to calculate the end distance e_3, show similar results, as shown in figure 5.12. The data of figures 5.10 and 5.11 is also plotted in this graph. It should be noted that the values of van Looveren seem to be more spread than the results of this research, of Kotteman. This is only due to the larger tear-out strengths that are obtained by van Looveren; when zooming in on the results of Kotteman, as in figures 5.10 and 5.11, an ostensibly larger spread is observed. The conformity between WAAM and rolled carbon steel might indicate that the used end distance in the model is still too conservative, as the Eurocode is even more conservative with its used end distance e_1.

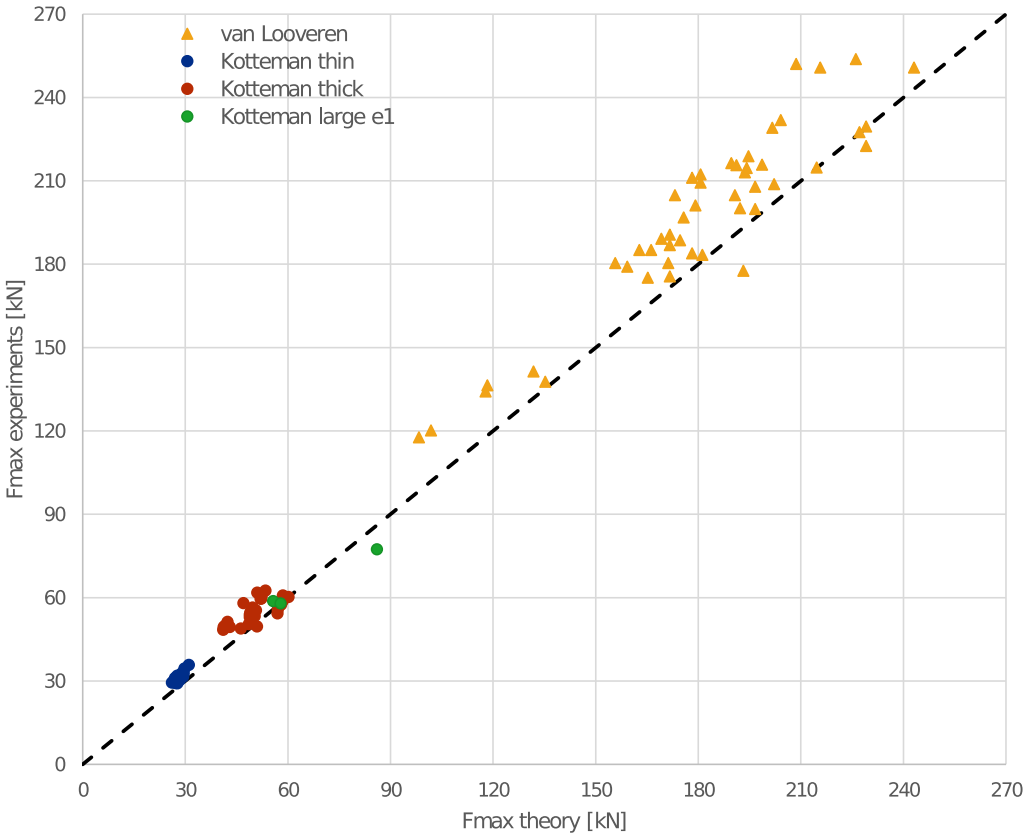

Figure 5.12: Experimental results compared with theoretical rolled carbon steel van Looveren [63] and WAAM carbon steel Kotteman

Not only the graphs show the level of agreement of the used model for the theoretical result with the experimental result, but factor $\bar{b}$ is also an indication. $\bar{b}$ has a value higher than 1, so the model for the tear-out strength is conservative. Another reason for this conservativeness might be that the assumption of the stresses that occur when the load is applied to the bolt or the pin are just shear stresses τ, is incorrect. It might be that other stresses occur as well, as normal stresses σ, according to Von Mises equation 5.13.

$$f_y = \sqrt{\sigma^2 + 3\tau^2} \tag{5.13}$$

It is assumed that the effective thickness t_{eff} and the ultimate tensile strength f_u are constant, as a reduction factor is applied to determine t_{eff}, as can be read in section 5.1.4, and f_u is determined by the milled tensile coupons. The correction that must be taken into account for the tear-out model equals $\bar{b}$ in table 5.9. From this table it can be seen that an average $\bar{b}$ of 1.1 for all specimens can be taken. The maximum theoretical tear-out force, according to the engineering model, $F_{tear-out}$ (equation 4.5), must be multiplied by this **modification factor** of **1.1** to obtain a value for the maximum tear-out force that is closer to the experimental value. This factor increases the values of the variables t_{eff}, f_u and e_3.

Design factor γ tear-out

The next step, when the diagrams of figures 5.10 and 5.11 are made, is to calculate the design factor γ with equation 5.18, which indicates the spread in tear-out results of the variables t_{eff}, f_u and e_3 in the tear-out model. The values for δ are shown in equation 5.14, 5.15, 5.16 and 5.17. The equations 3.4, 3.5 and 3.6 also hold for the calculation of the mean values μ and Coefficient of Variation V of the effective thickness t_{eff}, end distance e_3 and ultimate tensile strength f_u. The values can be found in appendix H.

$$\delta_i = \frac{F_{e,i}}{\bar{b} F_{t,i}} \tag{5.14}$$

$$\mu_\delta = \frac{\sum_{i=1}^{n} \delta_i}{n} = 1 \tag{5.15}$$

$$\sigma_\delta = \sqrt{\frac{1}{N} \sum_{i=1}^{n} (\delta_i - \mu_\delta)} \tag{5.16}$$

$$V_\delta = \frac{\sigma_\delta}{\mu_\delta} = \sigma_\delta \tag{5.17}$$

$$\gamma = \frac{R_{nom}}{R_d} = \frac{2 t_{eff}\, e_3\, \frac{f_u}{\sqrt{3}}}{\bar{b}\, \mu_{t_{eff}}\, \mu_{e_3}\, \mu_{f_u} (1 - \alpha_R\, \beta \sqrt{V_{t_{eff}}^2 + V_{e_3}^2 + V_{f_u}^2 + V_\delta^2})} \tag{5.18}$$

Where:
α_R = 0.8
β = 3.8 (RC2)

The reliability class (RC) of a building determines the factor β. Here, RC2 is assumed [8].

For the nominal values of t_{eff}, e_3 and f_u in the numerator of equation 5.18, the mean values are taken. The outcome of the design factors for every printing direction and the two thicknesses is displayed in table 5.10.

Table 5.10: Design factor γ

Printing direction	**Thickness**	γ
Transversal	thin	1.09
Longitudinal		1.03
Diagonal 45°		1.07
Transversal	thick	1.29
Longitudinal		1.54
Diagonal 45°		1.21

A larger design factor γ is seen for the thick than for the thin specimens. This is caused by a large spread in results, probably due to the larger surface roughness. It is concluded that the number of tested specimens is too low to have a good evaluation of the results for γ.

5.3.4. Large end distances bolted connections

49 connection tests are performed with bolts and pins, of which 45 have an end distance e_1 of $1.2d_0$. The remaining tests are performed on plates with a larger end distances of $2.0d_0$ to $2.2d_0$, as can be read in section 4.3.2. The results can be found in figure 5.12 and in the tables in appendix H in the light grey highlighted rows. It can be seen in these tables that the factor b_i, according to equation 5.11 for these samples is very close to the $\bar{b}$ in equation 5.12. Especially the thin samples have a value for b_i that is closer to the value of 1 than the other samples with the smaller end distances.

The failure mode of the specimens with the large end distances is bearing, instead of tear-out, as can be seen in figure 5.13. However, the used model appears to be reliable for this bearing failure of WAAM low carbon steel as well.

It should be mentioned that out-of-plane deformation is likely to occur when large end distances are applied, so a bolted connection set-up is more suitable, as the side plates are solid and out-of plane deformation is restrained. This in contrast to when a pinned connection set-up, applied in favour of the DIC, with side plates with holes, as in figure 3.17b, would be used.

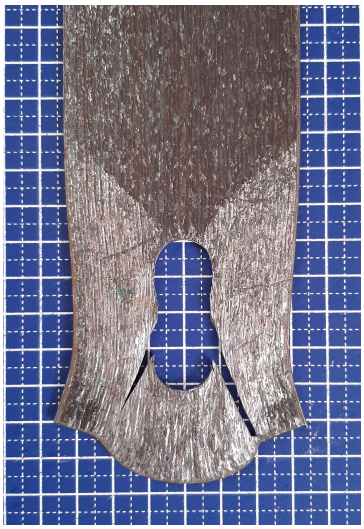

Figure 5.13: Bearing failure of bolted connection with large end distance

5.3.5. Fracture lines tear-out specimens

The fracture line of the tear-out specimens after failure might be different for the three printing directions, as the welds of the transversal samples are pressed together and the welds of the longitudinal are pushed away from each other as can be seen in figure 5.9. This can be a measure of anisotropy. The fracture lines were measured with a calliper. They appeared not to be straight, so not perpendicular to the load direction, as can be seen in a transversal thick sample in figure 5.14. The start of the failure in the bolt hole is diagonal and the direction of the shear face continued to be perpendicular either. The reason might be that not only shear stresses appear, but also tensile stresses. A typical tensile fracture line can be seen in figure L.1. The fracture line depends on the end distance e_3, so this dependence must be eliminated by dividing the e_3 by the fracture line length L_f, as can be seen in equation 5.19.

$$\xi = \frac{e_3}{L_f} \tag{5.19}$$

The results of this analysis are displayed in tables 5.11 and 5.12. In appendix L the measurements and results per specimen can be seen. From table 5.11 it can be concluded that the differences in factor ξ are small between the different printing directions. The differences with table 5.12 are not consistent per direction either. Therefore, no conclusion can be drawn from these results.

Table 5.11: Fracture line length thin tear-out specimens

Printing direction	L_f **[mm]**	ξ **[-]**	**SEM [-]**
Transversal	10.9	1.64	0.0563
Longitudinal	9.86	1.75	0.0705
Diagonal 45°	11.5	1.58	0.100

Figure 5.14: Fracture line thick transversal tear-out specimen

Table 5.12: Fracture line length thick tear-out specimens

Printing direction	L_f **[mm]**	ξ **[-]**	**SEM [-]**
Transversal	9.94	1.72	0.0676
Longitudinal	11.7	1.60	0.0465
Diagonal 45°	11.2	1.63	0.0630

Summary analysis results tear-out tests

The normalised force-displacement graphs of the tear-out tests point out that the transversal specimens resist the highest forces and the longitudinal the lowest. This can be due to "cooperation" of the welds, which is best for the transversal samples.
No significant difference in the results of the bolted versus the pinned connections is observed, so these are combined.
The statistical evaluation of the tear-out tests shows that the used model is slightly conservative, compared to the experimental outcome. However, the results are similar to conventionally produced carbon steel.
A modification factor $\bar{b} = 1.1$ is produced for the tear-out behaviour of WAAM low carbon steel, that needs to be multiplied with the theoretical maximum tear-out force from the used model $F_{max,tear-out} = 2t_{eff}\, e_3\, \frac{f_u}{\sqrt{3}}$.
The same model used for tear-out might also be applicable for bearing failure, so when large end distances are used.

6

Conclusions

6.1. Answer main research question

The following main research question was formulated:

'What are the design rules that need to be determined to assess the tear-out strength of a bolt or pin in a wire and arc additively manufactured carbon steel plate?'

A general answer can be given on this question, based on the literature study and the obtained experimental results on WAAM low carbon steel:
The tear-out strength of a single bolt or pin in a WAAM low carbon steel plate is dependent on material properties, as ultimate tensile strength and effective thickness, that both include the inhomogeneities of the material. It also depends on geometric properties, as end distance, bolt or pin and hole diameter and printing direction compared to the direction of the applied force.

6.1.1. Conclusions elaborated

In this section a more elaborated answer on the main research question is given by answering the sub questions, stated in section 1.3.

The following conclusions regarding the material properties are drawn from experiments on milled tensile coupons, as the surface roughness was eliminated and accurate cross-sectional measurements were possible. These outcomes were compared with the as-printed experimental results.

- The yield strength f_y of the milled **thin** specimens, with an intended as-printed thickness of 3 mm, is very similar for the three printing directions; an average of 403 MPa $\pm$ 3% was reached. The yield strength f_y of the milled **thick** diagonal 45° specimens, with an intended as-printed thickness of 6 mm, is highest; 359 MPa. The average of the thick samples was 334 MPa $\pm$ 7%, which is a lower strength than for the thin specimens. A cause might be the difference in printing process parameters between the two thicknesses. These average yield strength values are low, compared to the low carbon wire material properties, where a minimum value of 460 MPa is obtained normally. For the **thin** samples there is a difference of 12% and for the **thick** 27%;

- The ultimate tensile strength f_u of the milled **thin** specimens is very similar as well for the three printing directions; an average of 498 MPa $\pm$ 3% was reached. For the milled **thick** specimens this also holds; an average of 466 MPa $\pm$ 1% was observed. Like the yield strength, the thin specimens have a higher value. For the longitudinal as-printed samples, so when the applied force acts parallel to the printing direction, the highest yield and ultimate tensile strength is observed for both the thin and thick specimens. This is probably due to the difference in surface roughness. For design purposes, the material anisotropy, which is the difference in strength observed for the various printing directions, is discounted by the proposed reduction factors;

- The maximum value for the ultimate strain ε_u of the milled samples is achieved by the thick specimens; an average of 17% is observed. The deviation from the thin samples is only 1%. The transversal as-printed specimens have the lowest ultimate strain, when the force is applied

perpendicular to the printing direction. For the longitudinal samples, with the force parallel to printing direction, this value is highest and the diagonal had an ultimate strain in between. This has to do with orientation of the welds, compared to the applied force. The transversal specimens fail at the weakest weld, whereas the welds of the longitudinal sample cooperate, as they are stretched. Most importantly; the ductility requirements of the Eurocode are met for all printing directions;

- The Young's modulus E of all samples, thin, thick and every printing direction, has a value that is equivalent to conventionally produced carbon steel. An average of 205 GPa with a low standard deviation of 12% is obtained. E is on average higher for the thick samples; 5%;
- To account for the inhomogeneous material and its surface roughness, a reduction factor based on the effective thickness of the milled versus the as-printed experimental coupon results is proposed. The reduction factor is closest to 1 for the thin longitudinal specimens; 0.95. The smallest reduction factor belongs to the thick, especially the transversal and diagonal specimens; 0.86. This factor can be used when designing an as-printed object, such as a bolted connection of WAAM low carbon steel plates.

  It can be concluded that, the thicker the specimen, the higher the surface roughness and therefore the lower the reduction factor. The factor is highest for the longitudinal samples and lowest for the transversal. The diagonal specimens have a value in between.

  From statistical evaluation the following reduction factors are proposed:

  - Thin transversal: 0.90
  - Thin longitudinal: 0.95
  - Thin diagonal (45°): 0.93
  - Thick transversal: 0.86
  - Thick longitudinal: 0.94
  - Thick diagonal (45°): 0.86

The following can be concluded regarding the tear-out strength of single bolts and pins in a WAAM low carbon steel plate:

- Single pinned and bolted connections with small end distances e_1, with an average of $1.2d_0$, have similar tear-out failure behaviour when the bolt does not exert a frictional force on the plates. The maximum difference Δ of the normalised force between bolted and pinned connections is on average 5% for the transversal samples, thin and thick. The longitudinal samples have a difference of maximum 2.8% and the diagonal are the most consistent with a maximum of 1.2% difference between the bolted and pinned connections;
- The tear-out strength of a WAAM low carbon steel can be calculated similarly to conventionally produced carbon steel. However, this conclusion only holds if:

  Firstly, the ultimate tensile strength of a milled tensile coupon, which is lower than the material properties of the carbon steel wire, is known and taken as basis.

  Secondly, a reduction factor for the determination of the effective thickness of as-printed samples is considered, based on the milled tensile coupon tests.

  Then, the tear-out model used $F_{max,tear-out} = 2t_{eff}\, e_3\, \frac{f_u}{\sqrt{3}}$ has good agreement with both WAAM and rolled carbon steel, but is slightly conservative. The Eurocode method is even more conservative;
- A modification factor for the tear-out strength of WAAM carbon steel plates is produced, based on the deviation of the experimental and theoretical tear-out strength. The tear-out model has to be multiplied by this modification factor of 1.1 to obtain a more realistic value for the design of tear-out connections, so a better match with the experimental values is achieved.

7

Recommendations

In this section the results and conclusions are discussed and recommendations for future research are given, based on the performed experiments. Also, the relevance of this research as a whole is discussed:

- The WAAM low carbon steel has a low strength, compared to the material properties of the carbon steel wire. So, the wire properties are not a guideline for the material properties of the WAAM carbon steel, due to the influence of the printing process and printing parameters. This is observed by the lower strength values for the milled thick, compared to the thin samples. An improvement of the ultimate strength might be achieved by lowering the heat input for example. Less printing cycles is also an option to improve the strength, as this causes thermal damage of the microstructure. However, it should be mentioned that a higher strength goes hand in hand with a lower ductility, which is another important factor when designing steel structures;

- Further research should be undertaken by investigating the microstructure of WAAM low carbon steel to expand the knowledge of the influence of the grain structure and orientation on the material properties, as the ultimate tensile strength. By changing printing parameters, such as the heat input, printing speed or cooling rate, the strength or ductility might increase, which leads to more favourable properties for a certain structural design;

- The advantages of WAAM low carbon steel over other types of WAAM steel, as stainless, are the low price and the high ductility. The Young's modulus of WAAM low carbon steel is consistent with conventionally produced steel, where experimental results of researches on WAAM stainless steel (type 308) show significantly lower values for the E-modulus. The only drawbacks of WAAM carbon steel are the low strength, which can be taken into account easily by reduction factors, and that the material is susceptible to corrosion. A protective coating is a solution to this last problem. However, further research on resistance against corrosion of WAAM low carbon steel is recommended;

- To determine the material properties, the milled tensile coupons were taken as basis. Only three coupons were taken for every type of specimen. The standard variation of the material properties, especially for the Young's modulus was quite high. When more coupons would be used, a more realistic value will be the result and it could be checked if a lower spread in results would be obtained. A lower variation in material properties is observed for the as-printed coupons, where seven samples were tested;

- In this study the lower boundary of end distance e_1 is tested mostly; $1.2d_0$. A more elaborate study must be done on the tear-out of WAAM carbon steel; additional tests must be performed and more variation in end distances e_1 must be tested; until the upper boundary $3d_0$, when bearing becomes the governing failure mode;

- It is suggested to build WAAM connections and structures such that the strongest printing direction corresponds with the direction of the expected force that will be applied. For tear-out connections this is when the applied force is perpendicular to the printing direction and for pure tensile connections parallel. This are the first steps in optimising the topology;
- The data from the 3D scans of the WAAM samples and from the photos that are made during the tear-out experiments can be used for more in-depth investigations on the roughness of this material. A roughness parameter might be determined that holds for a certain type of WAAM plate, when the wire material and printing parameters are kept constant. This roughness parameter can be checked by a 3D scan and determines the effective thickness;
- It is recommended to do a Finite Element Analysis (FEA), so the strain distributions in the as-printed plate of the WAAM tear-out experiments can be compared with rolled carbon steel. This can give insights in the behaviour of the WAAM material. A good model can be made if the structure of the irregular surface can be modelled exactly. Best is to perform tear-out experiments with DIC on milled WAAM plates, so the surface roughness is not of influence on the strain distributions. This WAAM DIC model can be compared with the FE model and rolled steel tear-out tests;
- In future investigations the use of different printed thicknesses is recommended, to explore the influence of the printing parameters on the surface roughness and on the strength. When more roughnesses are investigated, a more accurate conclusion about the design factors might be the result. A thin material is preferred over a thick material due to the low surface roughness and the higher yield and ultimate tensile strength. However, a thick WAAM material consisting of several thin welds might be an option too.

Bibliography

[1] 247 watersnijden. URL https://www.247watersnijden.nl/.

[2] Artec 3D, Professional 3D scanners. URL https://www.artec3d.com.

[3] MX3D. URL https://mx3d.com/.

[4] SKF. URL www.skf.com.

[5] Go welding. URL http://gowelding.org.

[6] Nieuwstraten Proefstaven B.V. URL http://www.proefstaven.nl/.

[7] Training Ciricular - Welding Theory and Application, 1993.

[8] NEN-EN 1090-2 Execution of steel structures and aluminium structures - Part 2: Technical requirements for Execution of steel structures, 2008.

[9] NEN-EN 1993-1-8. Eurocode 3: Design of steel structures - Part 1-8: Design of joints, 2011.

[10] NEN-EN 1993-1-1. Eurocode 3: Design of steel structures - Part 1-1: General rules and rules for buildings., 2016.

[11] NEN-EN-ISO 6892-1 Metallic materials - Tensile testing - Part 1: Method of test at room temperature., 2016.

[12] RAMLAB unveils world's first class approved 3D printed ship's propeller, 2017. URL https://ramlab.com/updates/ramlab-unveils-worlds-first-class-approved-3d-printed-ships-propeller/.

[13] Zygo corporation - Surface Texture Parameters, 2018. URL www.zygo.com.

[14] British Stainless Steel Association, 2018. URL https://www.bssa.org.uk/topics.php?article=125.

[15] R. Aceti, G. Ballio, A. Capsoni, and L. Corradi. A limit analysis study to interpret the ultimate behavior of bolted joints. Journal of Constructional Steel Research, 60(9):1333–1351, 2004. ISSN 0143974X. doi: 10.1016/j.jcsr.2003.12.003.

[16] A. Akkurt. Surface properties of the cut face obtained by different cutting methods from AISI 304 stainless steel materials. Indian Journal of Engineering and Materials Sciences, 16(6):373–384, 2009. ISSN 09714588.

[17] M. Ashby, H. Shercliff, and D. Cebon. Materials - engineering, science, processing and design. Elsevier Ltd, Oxford, United Kingdom, 2nd edition, 2010. ISBN 978-1-85617-895-2.

[18] M. Attaran. The rise of 3-D printing: The advantages of additive manufacturing over traditional manufacturing. Business Horizons, 60(5):677–688, 2017. ISSN 00076813. doi: 10.1016/j.bushor.2017.05.011. URL http://dx.doi.org/10.1016/j.bushor.2017.05.011.

[19] A.C.M. Bekker, J.C. Verlinden, and G. Galimberti. Challenges in Assessing the Sustainability of Wire + Arc Additive Manufacturing for Large Structures. Solid Freeform Fabrication, 27(January 2017):406–416, 2016. ISSN 02763915. doi: 10.13140/RG.2.2.10258.86727.

[20] B. Bhushan. Modern Tribology book - Chapter 2 - Surface roughness analysis and measurement techniques. CRC Press LLC, 2001. ISBN 9780849377877. doi: 10.1201/9780849377877.ch2.

[21] K. Binon. Uw nieuwe gereedschapskist. Lastechniek vakblad, (juli):8–10, 2018.

[22] L.G. Blok, M.L. Longana, H. Yu, and B.K.S. Woods. An investigation into 3D printing of fibre reinforced thermoplastic composites. Additive Manufacturing, 22(November 2017):176–186, 2018. ISSN 22148604. doi: 10.1016/j.addma.2018.04.039.

[23] W.D. Callister. Materials Science and Engineering - An Introduction. John Wiley & Sons, Incorporated, New York, United States, 8th edition, 2007. ISBN 978-0-471-73696-7. URL https://www.academia.edu/32372808/Materials{_}Science{_}and{_}Engineering{_}An{_}Introduction.

[24] C.R. Cunningham, S. Wikshåland, F. Xu, N. Kemakolam, A. Shokrani, V. Dhokia, and S.T. Newman. Cost Modelling and Sensitivity Analysis of Wire and Arc Additive Manufacturing. Procedia Manufacturing, 11(June):650–657, 2017. ISSN 23519789. doi: 10.1016/j.promfg.2017.07.163.

[25] C.R. Cunningham, J.M. Flynn, A. Shokrani, V. Dhokia, and S.T. Newman. Invited review article: Strategies and processes for high quality wire arc additive manufacturing. Additive Manufacturing, 22(June):672–686, 2018. ISSN 22148604. doi: 10.1016/j.addma.2018.06.020. URL https://doi.org/10.1016/j.addma.2018.06.020.

[26] D. Ding, Z. Pan, D. Cuiuri, and H. Li. Robotics and Computer-Integrated Manufacturing - A practical path planning methodology for wire and arc additive manufacturing of thin-walled structures. Robotics and Computer Integrated Manufacturing, 34:8–19, 2015. ISSN 0736-5845. doi: 10.1016/j.rcim.2015.01.003. URL http://dx.doi.org/10.1016/j.rcim.2015.01.003.

[27] D. Ding, Z. Pan, D. Cuiuri, and H. Li. Wire-feed additive manufacturing of metal components : technologies , developments and future interests. pages 465–481, 2015. doi: 10.1007/s00170-015-7077-3.

[28] T. Doksanovic, H. Draganić, I. Radić, and D. Damjanovic. Stress – Strain Relationships and Influence of Testing. (16):50–63, 2018.

[29] A. Dolsma. 3D-printen van staalconstructies. Innovatiecatalogus, pages 90–95, 2019. URL https://www.slideshare.net/booosting/innovatiecatalogus-2019.

[30] H. Draganić, T. Dokšanović, and D. Markulak. Investigation of bearing failure in steel single bolt lap connections. Journal of Constructional Steel Research, 98:59–72, 2014. ISSN 0143974X. doi: 10.1016/j.jcsr.2014.02.011.

[31] D. Duerr and G. Pincus. Deformation behavior of pinned connections with large clearance. 1988.

[32] S. Galjaard, S. Hofman, N. Perry, and S. Ren. Optimizing Structural Building Elements in Metal by using Additive Manufacturing. International Association for Shell and Spatial Structures, (August), 2015. ISSN 10895639 15205215. doi: 10.1021/jp4029535.

[33] L. Gardner and D. Nethercot. Bearing failure in stainless steel bolted connections. (February), 2011. doi: 10.1016/j.engstruct.2010.11.013.

[34] I. Harms. Pinned connections. PhD thesis, TU Delft, 2015.

[35] A. Hayward, F. Weare, and A.C. Oakhill. Steel Detailers' Manual. John Wiley & Sons, Incorporated, 3 edition, 2011. ISBN 9781405175210. URL https://ebookcentral-proquest-com.tudelft.idm.oclc.org/lib/delft/reader.action?docID=675184{&}ppg=23.

[36] B. Hekker. Facade elements for 3DCP. Technical report, TU Delft, 2018.

[37] S. Joosten. Printing a Stainless Steel Bridge - An exploration of structural properties of stainless steel additive manufactures for civil engineering purposes. Technical report, TU Delft, 2015.

[38] A.G. Kamtekar. On the bearing strength of bolts in clearance holes. Journal of Constructional Steel Research, 79:48–55, 2012. ISSN 0143974X. doi: 10.1016/j.jcsr.2012.07.008. URL http://dx.doi.org/10.1016/j.jcsr.2012.07.008.

[39] S. Kiakidis. Mechanical and corrosion behaviour of 3D printed aluminium bronzes produced by wire+arc additive manufacturing. Technical report, TU Delft, 2017.

[40] H.J. Kim and J.A. Yura. The effect of ultimate-to-yield ratio on the bearing strength of bolted connections. Journal of Constructional Steel Research, 49(3):255–269, 1999. ISSN 0143974X. doi: 10.1016/S0143-974X(98)00220-X.

[41] V. Laghi, M. Palermo, G. Gasparini, S. Silvestri, and T. Trombetti. The application of weld-based additive manufacturing steel to structural engineering. ISEC, pages 1–5, 2019.

[42] J. Lange and T. Feucht. 3D-Printing with Steel : Additive Manufacturing of Connection Elements and Beam Reinforcements. IABSE Symposium 2019 Guimaraes, (March):1–7, 2019.

[43] McKinsey Global Institute (MGI). A future that works - Executive summary. (January):1–28, 2017. URL https://www.mckinsey.com/{~}/media/mckinsey/featuredinsights/DigitalDisruption/Harnessingautomationforafuturethatworks/MGI-A-future-that-works-Executive-summary.ashx.

[44] P. Može. Bearing strength at bolt holes. Presentation of latest test results and proposal of amendments on EN 1993-1-8, 2015.

[45] P. Može. Bearing strength at bolt holes in connections with large end distance and bolt pitch. Journal of Constructional Steel Research, 147:132–144, 2018. ISSN 0143974X. doi: 10.1016/j.jcsr.2018.04.006.

[46] P. Može and D. Beg. A complete study of bearing stress in single bolt connections. Journal of Constructional Steel Research, 95:126–140, 2014. ISSN 0143974X. doi: 10.1016/j.jcsr.2013.12.002.

[47] NEN. Eurocode 3 - Design of Steel Structures - Part 1-4, 2006.

[48] NEN. Eurocode 3 - Design of steel structures - Part 1-1, 2011.

[49] M.P. Nijgh. Capita Selecta - Lecture S3 - Introduction to the Reliability of Steel Structures, 2019.

[50] Oerlikon. CARBOFIL 1A. URL https://www.oerlikon-welding.com/nl/carbofil-1a-elite.

[51] J.F. Pagotto, F.J. Recio, A.J. Motheo, and P. Herrasti. Multilayers of PAni/n-TiO2and PAni on carbon steel and welded carbon steel for corrosion protection. Surface and Coatings Technology, 289:23–28, 2016. ISSN 02578972. doi: 10.1016/j.surfcoat.2016.01.046. URL http://dx.doi.org/10.1016/j.surfcoat.2016.01.046.

[52] Royal HaskoningDHV. Shaded Dome technologies, 2019.

[53] H. Snijder, D. Ungermann, J. Starkt, G. Sedlacek, F. Bijlaard, and A. Hemmert-Halswick. Evaluation of test results on bolted connections in order to obtain strength functions and suitible model factors - part a: Results. v: Eurocode no.3 - part 1 - background documentation, 1988.

[54] H.H. Snijder, R.W.A. Dekker, and P.A. Teeuwen. Net cross-section failure of steel plates at bolt holes: Numerical work and statistical assessment of design rules. Ce/Papers, 1(2-3):3679–3688, 2017. doi: 10.1002/cepa.424.

[55] M. Srinivas and B. Sridhar Babu. A Critical Review on Recent Research Methodologies in Additive Manufacturing. Materials Today: Proceedings, 4(8):9049–9059, 2017. ISSN 22147853. doi: 10.1016/j.matpr.2017.07.258. URL https://doi.org/10.1016/j.matpr.2017.07.258.

[56] H. Strauß and U. Knaack. Additive Manufacturing for Future Facades: The potential of 3D printed parts for the building envelope. Journal of Facade Design and Engineering, 3(3-4):225–235, 2015. ISSN 2213302X. doi: 10.3233/fde-150042.

[57] A. Tamboli. Handbook of Structural Steel Connection Design and Details. McGraw-Hill Companies, Inc., New York, 2nd edition, 2010. ISBN 9780071550055.

[58] T.H.C. Tebbens. 3D Printing a Stainless Steel Pedestrian Bridge - Safe Design by Experiments. Technical report, TU Delft, 2018.

[59] M.K. Thompson, G. Moroni, T. Vaneker, G. Fadel, R.I. Campbell, I. Gibson, A. Bernard, J. Schulz, P. Graf, B. Ahuja, and F. Martina. Design for Additive Manufacturing: Trends, opportunities, considerations, and constraints. CIRP Annals - Manufacturing Technology, 65(2):737–760, 2016. ISSN 17260604. doi: 10.1016/j.cirp.2016.05.004.

[60] A. Ureña, E. Otero, M.V. Utrilla, and C.J. Múnez. Weldability of a 2205 duplex stainless steel using plasma arc welding. Journal of Materials Processing Technology, 182(1-3):624–631, 2006. ISSN 09240136. doi: 10.1016/j.jmatprotec.2006.08.030.

[61] G.S. van Bolderen. Exploration of Stability of 3D-Printed Steel Members - A study to buckling behaviour of wire and arc additively manufactured stainless steel tubular columns. Technical report, TU Delft, 2017.

[62] L.P.L. van der Linden. Innovative Joints For Gridshells. Technical report, TU Delft, 2015.

[63] H.L.B. van Looveren. Stuikweerstand van boutverbindingen Eurocode versus nieuwe methode. Technical report, 2019.

[64] M. Veljkovic. Fatigue, CIE5126, lecture 5, bolted joints., 2016.

[65] A. Verbart, F. van Keulen, and M. Langelaar. Topology Optimization with Stress Constraints. PhD thesis, TU Delft, 2015. URL http://www2.dbd.puc-rio.br/pergamum/tesesabertas/1512532{_}2017{_}completo.pdf.

[66] Dura Vermeer and Autodesk. Is this the future of construction sites?, 2018. URL https://www.deingenieur.nl/artikel/is-this-the-future-of-construction-sites.

[67] M. Vogt, K. Dilger, and M. Kassner. Investigations on different fatigue design concepts using the example of a welded crossbeam connection from the underframe of a steel railcar body. International Journal of Fatigue, 34(1):47–56, 2012. ISSN 01421123. doi: 10.1016/j.ijfatigue.2011.01.017. URL http://dx.doi.org/10.1016/j.ijfatigue.2011.01.017.

[68] Y. B. Wang, Y. F. Lyu, G. Q. Li, and J. Y. R. Liew. Behavior of single bolt bearing on high strength steel plate. Journal of Constructional Steel Research, 137(December 2016):19–30, 2017. ISSN 0143974X. doi: 10.1016/j.jcsr.2017.06.001. URL https://doi.org/10.1016/j.jcsr.2017.06.001.

[69] S. W. Williams, F. Martina, A. C. Addison, J. Ding, G. Pardal, and P. Colegrove. Wire + Arc Additive Manufacturing. Materials Science and Technology, 32(7):641–647, 2016. ISSN 0267-0836. doi: 10.1179/1743284715Y.0000000073. URL http://www.tandfonline.com/doi/full/10.1179/1743284715Y.0000000073.

[70] B. Wu, Z. Pan, D. Ding, D. Cuiuri, H. Li, J. Xu, and J. Norrish. A review of the wire arc additive manufacturing of metals: properties, defects and quality improvement. Journal of Manufacturing Processes, 35(August):127–139, 2018. ISSN 15266125. doi: 10.1016/j.jmapro.2018.08.001. URL https://doi.org/10.1016/j.jmapro.2018.08.001.

[71] J. Xiong, Y. Li, R. Li, and Z. Yin. Influences of process parameters on surface roughness of multi-layer single-pass thin-walled parts in GMAW-based additive manufacturing. Journal of Materials Processing Technology, 252(February 2017):128–136, 2018. ISSN 09240136. doi: 10.1016/j.jmatprotec.2017.09.020. URL http://dx.doi.org/10.1016/j.jmatprotec.2017.09.020.

[72] P. Young. What is slag in welding, 2019. URL https://weldingheadquarters.com/what-is-slag-in-welding/.

[73] W. Zhang, A. De, A. Wilson-Heid, A.M. Beese, J.W. Elmer, J.S. Zuback, T. Mukherjee, J.O. Milewski, T. DebRoy, and H.L. Wei. Additive manufacturing of metallic components – Process, structure and properties. In Progress in Materials Science, volume 92, pages 112–224. 2017. doi: 10.1016/j.pmatsci.2017.10.001.

[74] X. Zhang, S. Yang, W. Zhang, H. Guo, and X. He. Influence of outer rust layers on corrosion of carbon steel and weathering steel during wet-dry cycles. Corrosion Science, 82:165–172, 2014. ISSN 0010938X. doi: 10.1016/j.corsci.2014.01.016. URL http://dx.doi.org/10.1016/j.corsci.2014.01.016.

A

Appendix wire material Carbofil

CARBOFIL 1A

OERLIKON

MIG-MAG Wires
C-Mn and low-alloy steels

Carbofil 1A is a copper coated solid wire used with CO2 or mixed Ar/CO2 shielding gases. Suited for welding a wide range of structural steels, earthmoving and construction site work. Suitable for high strength carbon-manganese steels, types Fe 490 Fe 510.

Classification	
AWS	A5.18: ER 70S-6
EN	440: G 46 3 M G4 Si1

Approvals	Grades
ABS	
BV	
DB	
DNV	
GL	
LRS	

see Appendix, Classification Society Approvals, for details pag. 521

Analysis of all-weld metal (Typical values in %)

C	Mn	Si	P	S	Cr	Ni	Mo	Nb	V	N	Cu
0.06	1.70	0.90	≤ 0.020	≤ 0.030	-	-	-	-	-	-	-

All-weld metal Mechanical Properties

Heat Treatment	Yield Strength N/mm²	Tensile Strength N/mm²	Elongation A5 (%)	Impact Energy ISO - V (J) -30°C	Hardness
As Welded	≥ 460	550-630	≥ 24	≥ 47	-

Gas test: Acc. To EN 439: M21(Arcal 21-Atal 6)

Shielding Gas: Acc. To EN 439: M21(Arcal21-Atal6) or C1(Arcal 2)

Materials

S(P)235 to S(P)460; GP240; GP280

Storage
Keep dry and avoid condensation

Current condition and welding position
DC+

Packaging data: K300 Kg. 16

Diameters	0,8	1,0	1,2	1,6		

Figure A.1: Composition Carbofil 1A [50]

B

Appendix overview tensile coupon values

(a) Thin specimens

	Average width middle part [mm]	Standard deviation width	Average thickness middle part [mm] calliper	Standard deviation thickness	Average dry weight [g]	Standard deviation dry weight	Average weight in water [g]	Standard deviation weight in water	Mean thickness t [mm] Archimedes	Deviation t Archimedes versus calliper [%]
T7a	12.37	0.05902	1.52	0.01282	30.88	0.005774	26.91	0.005774	1.67	9.79
T7f	12.31	0.05553	1.50	0.03196	30.16	0.005774	26.28	0.01000	1.63	9.18
T7h	12.37	0.07924	1.70	0.01553	33.40	0.000000	29.11	0.01155	1.81	6.39
L7b	11.60	0.1731	1.65	0.02816	29.87	0.010000	26.02	0.005774	1.66	0.78
L7e	12.34	0.08228	1.76	0.01126	32.55	0.000000	28.36	0.01155	1.77	0.32
L7h	12.43	0.06364	1.72	0.01195	32.20	0.000000	28.07	0.01000	1.74	0.90
D8a	12.40	0.07573	1.72	0.02357	32.09	0.000000	27.98	0.02082	1.84	6.77
D8b	12.37	0.1107	1.78	0.01773	32.36	0.005774	28.20	0.02082	1.86	4.54
D8c	12.45	0.05976	1.72	0.01959	30.97	0.000000	26.98	0.02082	1.78	3.34
	12.29		**1.67**							

(b) Thick specimens

	Average width middle part [mm]	Standard deviation width	Average thickness middle part [mm] calliper	Standard deviation thickness	Average dry weight [g]	Standard deviation dry weight	Average weight in water [g]	Standard deviation weight in water	Mean thickness t [mm] buoyancy	Deviation t Archimedes versus calliper [%]
T11a	12.49	0.06739	3.52	0.007440	67.96	0.000000	59.25	0.005774	3.65	2.38
T11f	12.58	0.07150	3.57	0.006409	68.39	0.005774	59.64	0.005774	3.66	2.09
T11h	12.69	0.06964	3.59	0.008864	68.59	0.000000	59.82	0.005774	3.66	2.92
L11b	12.48	0.08648	3.55	0.007071	67.89	0.005774	59.19	0.005774	3.65	2.45
L11e	12.45	0.07520	3.56	0.01195	67.99	0.005774	59.27	0.010000	3.66	2.84
L11h	12.48	0.05890	3.56	0.01356	67.94	0.000000	59.24	0.000000	3.65	2.27
D12a	12.36	0.1113	3.57	0.01885	65.38	0.005774	57.01	0.005774	3.75	5.03
D12b	12.37	0.07667	3.57	0.007440	65.41	0.000000	57.05	0.005774	3.74	4.56
D12c	12.48	0.04809	3.58	0.004629	65.45	0.007071	57.06	0.005774	3.74	4.88
	12.49		**3.56**							

Table B.1: Milled tensile coupon measured dimensions

(a) Thin specimens

	Average width middle part	Standard deviation	Average dry weight [g]	Standard deviation	Average weight in water [g]	Standard deviation	Mean thickness t [mm] Archimedes
T7b	12.49	0.1278	46.19	0.007071	40.20	0.007071	175.888
T7c	12.55	0.07539	45.98	0.000000	40.03	0.007071	176.635
T7d	12.52	0.08124	46.38	0.007071	40.35	0.000000	0.000
T7e	12.57	0.09051	46.03	0.007071	40.07	0.000000	0.000
T7g	12.70	0.1235	46.66	0.01414	40.62	0.007071	174.070
L7a	12.46	0.1016	45.53	0.000000	39.63	0.000000	0.000
L7c	12.32	0.1569	46.09	0.007071	40.11	0.01414	352.460
L7d	12.49	0.08288	46.59	0.007071	40.55	0.000000	0.000
L7f	12.53	0.06653	46.13	0.007071	40.16	0.007071	176.063
L7g	12.54	0.1063	46.99	0.007071	40.89	0.01414	345.738
D8d	12.51	0.09161	52.68	0.007071	45.85	0.01414	308.348
D8e	12.59	0.1360	53.26	0.007071	46.36	0.000000	0.000
D8f	12.59	0.1194	53.04	0.000000	46.16	0.007071	153.179
D8g	12.56	0.1130	53.06	0.007071	46.18	0.007071	153.113
D8h	12.56	0.1129	53.47	0.007071	46.54	0.007071	151.929

(b) Thick specimens

	Average width middle part	Standard deviation	Average dry weight [g]	Standard deviation	Average weight in water [g]	Standard deviation	Mean thickness t [mm] Archimedes
T11b	12.52	0.1190	108.11	0.000000	94.12	0.04950	5.863
T11c	12.69	0.1079	107.775	0.007071	93.87	0.007071	5.797
T11d	12.58	0.1610	108.555	0.007071	94.54	0.01414	5.861
T11e	12.65	0.0960	107.65	0.000000	93.78	0.007071	5.789
T11g	12.60	0.1334	108.54	0.000000	94.53	0.007071	5.858
L11a	12.45	0.1506	106.57	0.000000	92.82	0.007071	5.775
L11c	12.53	0.1816	110.335	0.007071	96.05	0.02121	5.985
L11d	12.63	0.1716	110.48	0.000000	96.21	0.007071	5.959
L11f	12.66	0.1512	106.705	0.007071	92.93	0.01414	5.745
L11g	12.60	0.1741	109.34	0.000000	95.19	0.007071	5.916
D12d	12.56	0.1718	104.465	0.007071	90.99	0.02121	5.991
D12e	12.50	0.1771	105.725	0.007071	92.09	0.007071	6.075
D12f	12.54	0.1778	104.36	0.000000	90.91	0.007071	5.985
D12g	12.52	0.1540	104.43	0.000000	90.98	0.007071	5.987
D12h	12.67	0.1882	105.05	0.000000	91.50	0.000000	6.001

Table B.2: As-printed tensile coupon measured dimensions

Table B.3: Extra specimens

	Average width middle part	Standard deviation	Average dry weight [g]	Standard deviation	Average weight in water [g]	Standard deviation	Mean thickness t [mm] Archimedes
T9a	12.29	0.1250	54.09	0.000000	47.08	0.01414	2.959
L9a	12.28	0.1441	52.53	0.007071	45.73	0.007071	2.871
D9a	12.24	0.1170	53.00	0.007071	46.13	0.007071	2.904
T10a	12.25	0.1400	55.00	0.000000	47.87	0.007071	3.015
L10a	12.22	0.1110	54.20	0.000000	47.17	0.007071	2.976
D10a	12.30	0.1317	55.23	0.007071	48.08	0.007071	3.017
T13a	12.32	0.1620	110.76	0.000000	96.36	0.007071	6.074
L13a	12.38	0.1671	108.54	0.000000	94.30	0.007071	5.995
D13a	12.47	0.1528	111.05	0.000000	96.59	0.02121	6.071
T14a	12.48	0.2337	110.35	0.007071	96.08	0.02121	5.987
L14a	12.45	0.2016	113.21	0.000000	98.51	0.007071	6.174
D14a	12.51	0.1975	110.19	0.000000	95.92	0.02121	5.983

C

Appendix overview tensile coupon results

Table C.1: Milled thin tensile coupon results

Weld direction	Sample name	Mean thickness t [mm] calliper	Mean width w middle part [mm]	Yield strength fy [MPa]	Ultimate tensile strength fu [MPa]	Young's modulus E [MPa]	Ultimate strain εu [%]
Transversal	T7a	1.52	12.37	412.2880	501.9967	205163	17.08042
	T7f	1.50	12.31	415.0687	-	202737	-
	T7h	1.70	12.37	420.3169	519.3602	183846	19.03468
	μ	1.573	12.351	416	511	197249	18.06
	σ	0.1097	0.0323	4.0772	12.2778	11670	1.382
	V	0.06974	0.002613	0.0098	0.0240	0.059	0.0765
Longitudinal	L7b	1.65	11.60	403.7299	492.7076	183179	13.33626
	L7e	1.76	12.34	393.5681	502.9201	195623	18.39980
	L7h	1.72	12.43	401.6472	500.1006	212468	17.10498
	μ	1.710	12.123	400	499	197090	16.28
	σ	0.0576	0.4562	5.3677	5.2742	14700	2.631
	V	0.03368	0.03763	0.01343	0.01058	0.07458	0.162
Diagonal	D8a	1.72	12.40	399.9807	469.8802	210248	17.18328
	D8b	1.78	12.37	379.2898	482	208785	16.28402
	D8c	1.72	12.45	398.8972	499.8703	196609	17.18394
	μ	1.741	12.406	393	484	205214	16.88
	σ	0.0339	0.0376	11.6457	15.0867	7488	0.519
	V	0.01948	0.00303	0.02965	0.03118	0.03649	0.0308

Table C.2: Milled thick tensile coupon results

Weld direction	Sample name	Mean thickness t [mm] calliper	Mean width w middle part [mm]	Yield strength fy [MPa]	Ultimate tensile strength fu [MPa]	Young's modulus E [MPa]	Ultimate strain εu [%]
Transversal	T11a	3.65	12.49	320.1168	465.856	209266	15.91722
	T11f	3.66	12.58	333.3133	468.743	207966	17.53550
	T11h	3.66	12.69	325.5420	462.288	203102	16.62250
	μ	3.658	12.586	326.324	466	206778	16.69
	σ	0.0044	0.0972	6.6329	3.2335	3249	0.811
	V	0.00120	0.00773	0.02033	0.00694	0.01571	0.0486
Longitudinal	L11b	3.65	12.48	319.2325	462.193	212342	20.84307
	L11e	3.66	12.45	324.3484	468.516	216625	19.59287
	L11h	3.65	12.48	310.9770	457.552	203570	21.46760
	μ	3.652	12.470	318	463	210846	20.63
	σ	0.0066	0.0141	6.7469	5.5035	6655	0.955
	V	0.00181	0.0011	0.0212	0.0119	0.032	0.0463
Diagonal	D12a	3.75	12.36	365.3900	468.411	210120	19.37826
	D12b	3.74	12.37	354.3174	471.119	222205	20.81566
	D12c	3.74	12.48	357.9172	464.375	204926	18.33434
	μ	3.741	12.402	359.208	468	212417	19.51
	σ	0.0049	0.0647	5.6481	3.3937	8866	1.246
	V	0.00131	0.0052	0.0157	0.0073	0.042	0.0639

Table C.3: As-printed thin tensile coupon results

Weld direction	Sample name	Mean thickness t [mm] buoyancy	Mean width w middle part [mm]	Yield strength fy [MPa]	Ultimate tensile strength fu [MPa]	Young's modulus E [MPa]	Ultimate strain εu [%]
Transversal	T7b	2.512	12.49	327.0000	460.4920	189070	15.41866
	T7c	2.493	12.55	359.3567	472.5986	217721	17.91858
	T7d	2.524	12.52	341.8190	458.3473	225092	15.33936
	T7e	2.491	12.57	352.0240	467.5217	224740	15.79076
	T7g	2.518	12.70	342.8797	462.7249	264127	16.62994
	T9a	2.959	12.29	318.6955	460.9225	190740	16.48396
	T10a	3.015	12.25	348.9134	467.8570	197400	16.67528
	μ	2.645	12.48	341.5269	464	215556	16.32
	σ	0.2346	0.1583	14.241	5.094	26414	0.900
	V	0.08872	0.01268	0.0417	0.0110	0.123	0.0551
Longitudinal	L7a	2.477	12.46	374.7745	479.0614	205117	17.66400
	L7c	2.519	12.32	376.8496	474.4808	200306	16.75808
	L7d	2.531	12.49	382.2315	464.4620	192924	15.95238
	L7f	2.500	12.53	376.5198	470.9760	195873	18.58448
	L7g	2.552	12.54	379.4157	472.4021	195473	17.73148
	L9a	2.871	12.28	413.8126	497.3682	214240	17.87840
	L10a	2.976	12.22	388.0374	489.8305	204560	19.10452
	μ	2.632	12.41	384.5202	478	201213	17.67
	σ	0.2025	0.1301	13.660	11.486	7384.0	1.059
	V	0.0769	0.01048	0.03552	0.0240	0.037	0.0599
Diagonal	D8d	3.039	12.51	335.0803	454.2173	206520	17.79172
	D8e	3.062	12.59	328.1384	442.5398	190861	16.00710
	D8f	3.057	12.59	336.4011	453.8294	207908	18.12200
	D8g	3.057	12.56	345.7138	453.9742	184889	16.90580
	D8h	3.080	12.56	328.0233	444.8692	208393	15.42748
	D9a	2.904	12.24	350.7392	473.5980	199270	14.07584
	D10a	3.017	12.30	354.5678	470.3517	202810	18.47890
	μ	3.031	12.48	339.8091	456	200093	16.69
	σ	0.0593	0.1442	10.656	11.779	9090	1.602
	V	0.01958	0.01155	0.0314	0.0258	0.0454	0.0960

Table C.4: As-printed thick tensile coupon results

Weld direction	Sample name	Mean thickness t [mm] buoyancy	Mean width w middle part [mm]	Yield strength fy [MPa]	Ultimate tensile strength fu [MPa]	Young's modulus E [MPa]	Ultimate strain εu [%]
Transversal	T11b	5.863	12.52	263.7305	389.604	182699	12.18900
	T11c	5.797	12.69	276.1036	407.078	153961	16.48432
	T11d	5.861	12.58	261.4628	399.452	189025	14.87934
	T11e	5.789	12.65	269.1375	408.327	168940	15.43708
	T11g	5.858	12.60	274.6304	403.555	189763	14.42432
	T13a	6.074	12.32	267.915	388.3036	174840	9.551340
	T14a	5.987	12.48	264.5714	418.0176	187930	15.24816
	μ	5.890	12.55	268.2216	402	178165	14.03
	σ	0.1038	0.1232	5.527	10.587	13231	2.374
	V	0.01762	0.00982	0.0206	0.0263	0.074	0.169
Longitudinal	L11a	5.775	12.45	342.5718	440.95	200189	16.53802
	L11c	5.985	12.53	333.3650	426.672	208718	20.73260
	L11d	5.959	12.63	307.0252	425.018	173020	18.63956
	L11f	5.745	12.66	303.7062	426.58	193252	18.85680
	L11g	5.916	12.60	289.0151	415.826	192233	20.94800
	L14a	6.174	12.45	319.4908	443.5972	202310	19.21988
	L13a	5.995	12.38	-	-	193760	10.79928
	μ	5.936	12.53	315.8624	430	194783	19.16
	σ	0.1448	0.1054	19.897	10.516	11281	1.607
	V	0.0244	0.00841	0.06299	0.0245	0.058	0.0839
Diagonal	D12d	5.991	12.56	280.3515	408.927	185365	19.11546
	D12e	6.075	12.50	270.0141	396.551	167183	18.49280
	D12f	5.985	12.54	276.8578	406.212	184344	18.80096
	D12g	5.987	12.52	282.6630	410.48	239171	20.75220
	D12h	6.001	12.67	283.8815	416.507	198975	19.18868
	D13a	6.071	12.47	283.4415	410.4557	205960	12.23686
	D14a	5.983	12.51	297.7579	418.9098	200990	14.20894
	μ	6.013	12.54	282.138	410	197427	17.54
	σ	0.0412	0.0640	8.4366	7.2800	22590	3.089
	V	0.00686	0.00510	0.0299	0.0178	0.1144	0.176

D

Appendix tensile coupon force-deformation curves

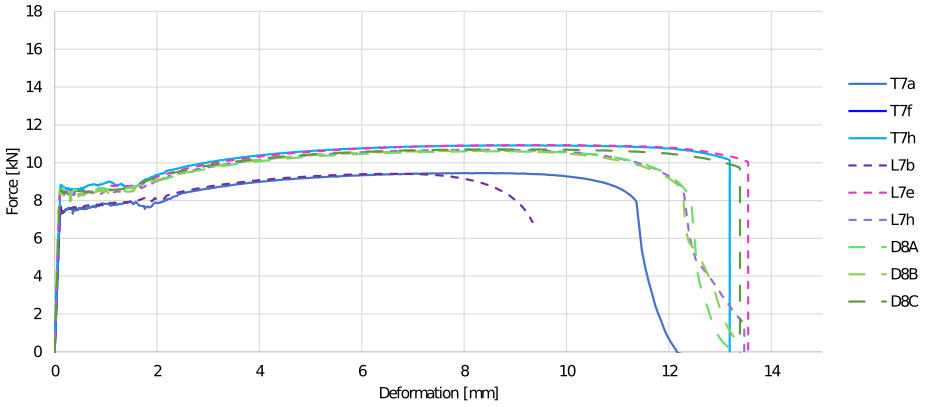

(a) Thin

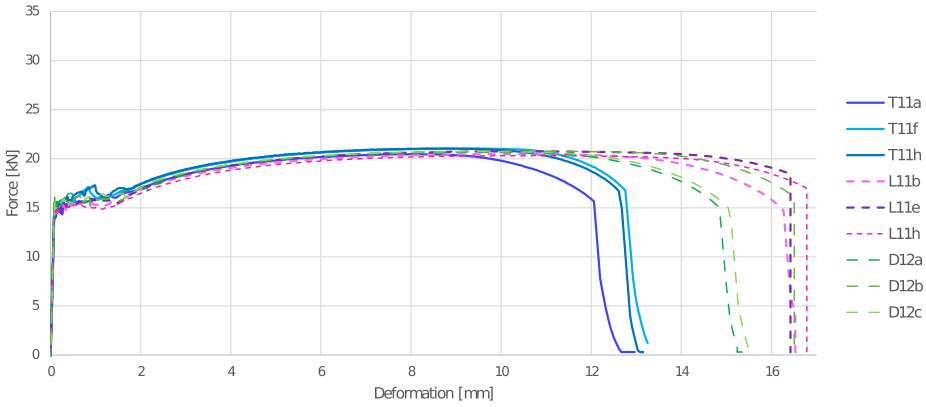

(b) Thick

Figure D.1: Force-deformation curves milled specimens

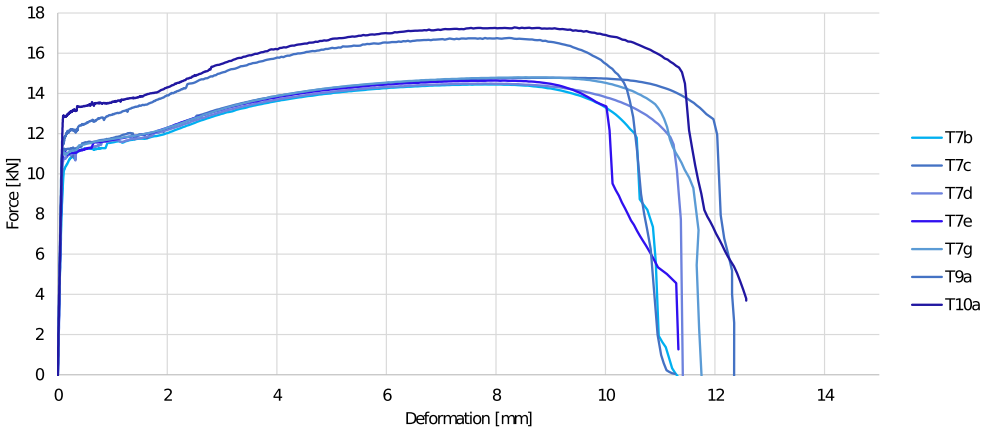

(a) Transversal

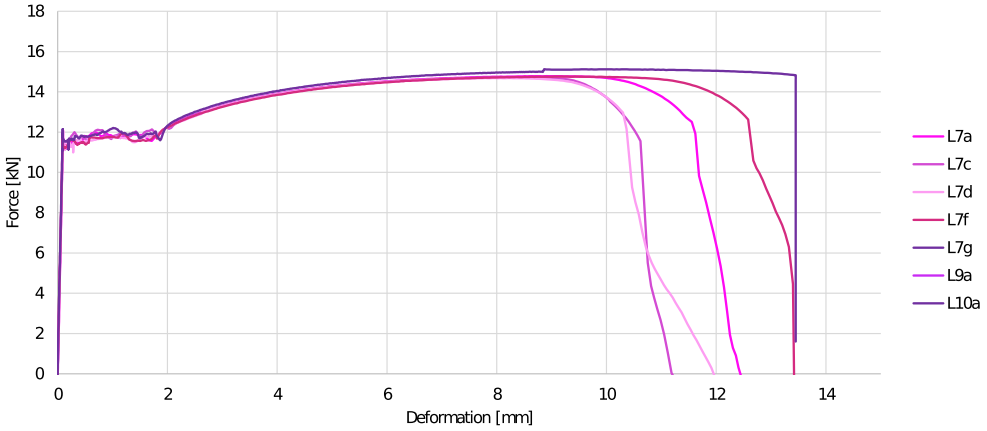

(b) Longitudinal

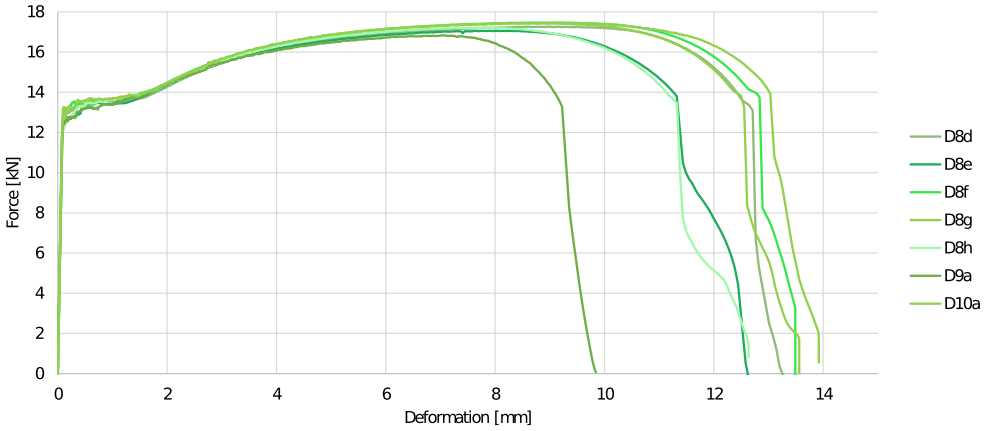

(c) Diagonal

Figure D.2: Force-deformation curves thin as-printed specimens

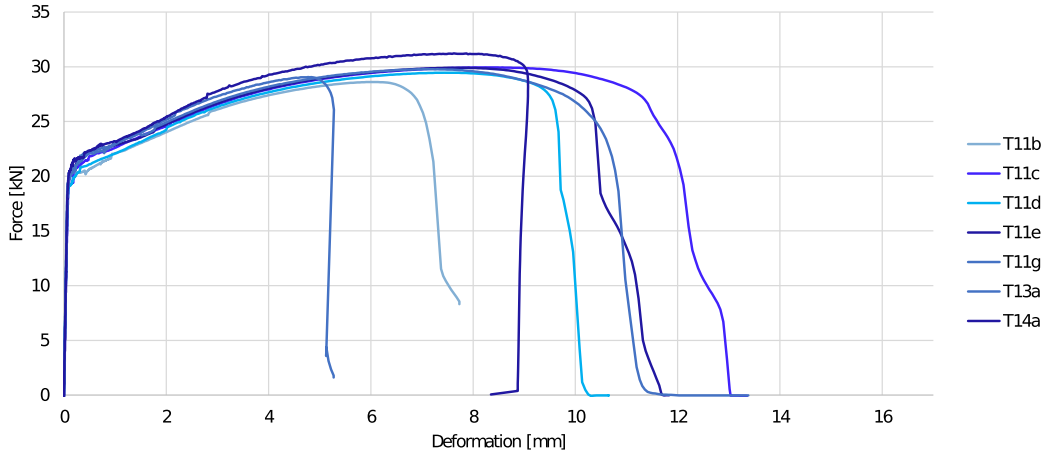

(a) Transversal

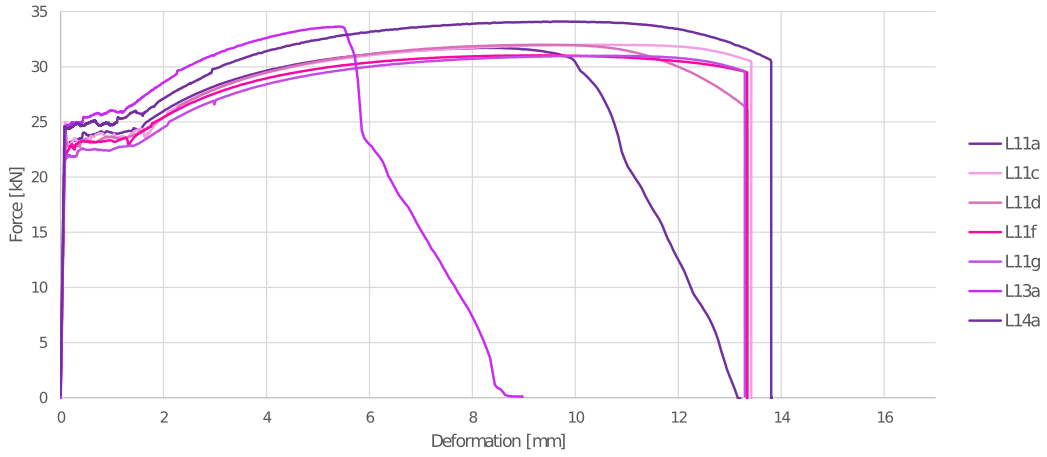

(b) Longitudinal

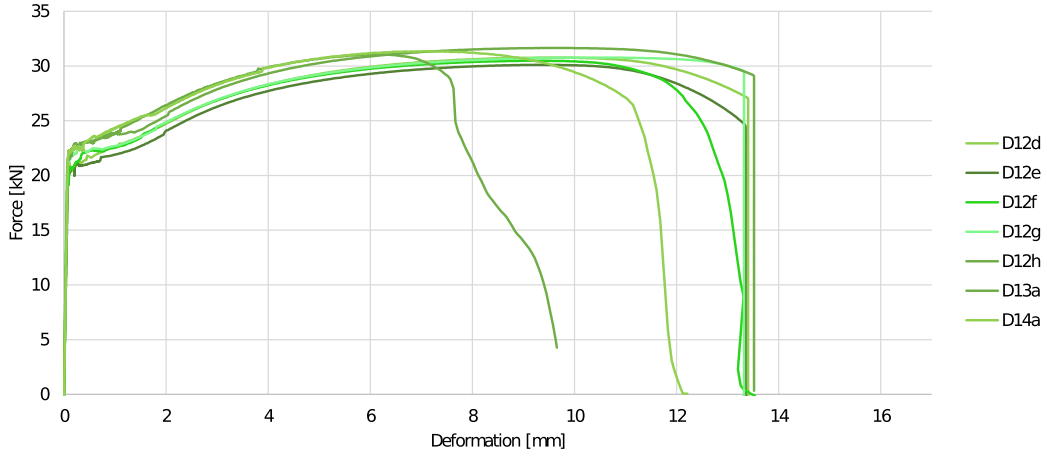

(c) Diagonal

Figure D.3: Stress-strain curves thick as-printed specimens

E

Appendix milled tensile coupon stress-strain curves

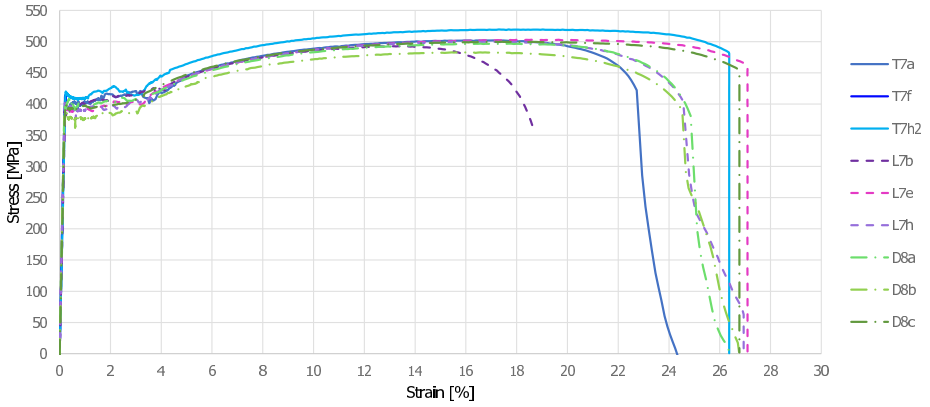

(a) Stress-strain diagram

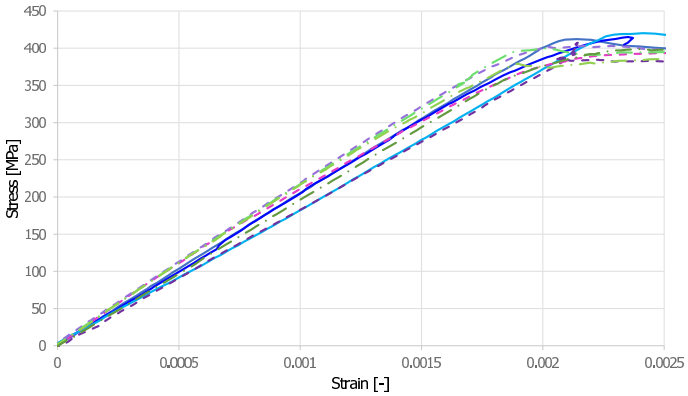

(b) Linear elastic part

Figure E.1: Stress-strain curves milled thin specimens

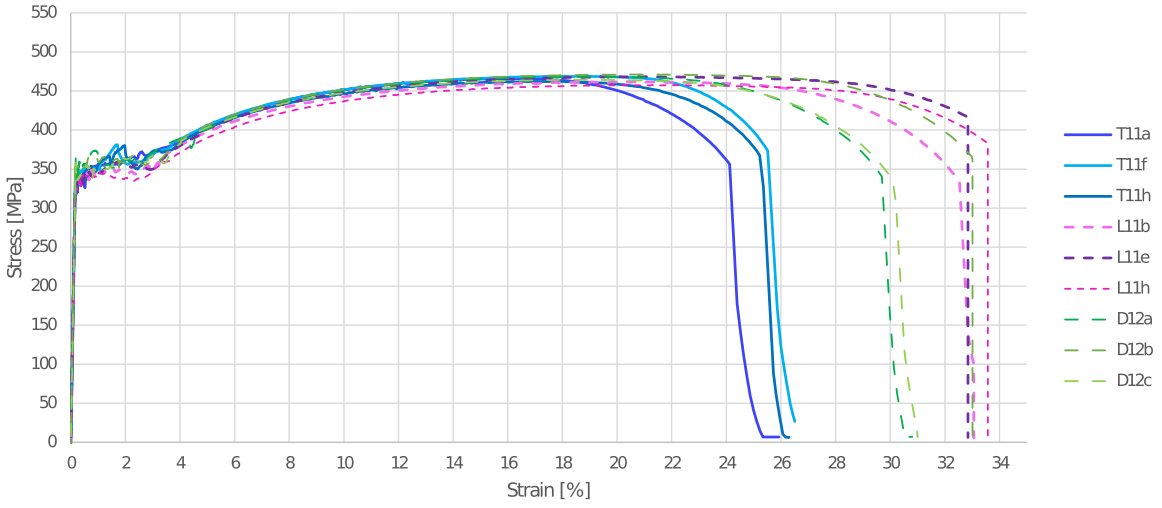

(a) Stress-strain diagram

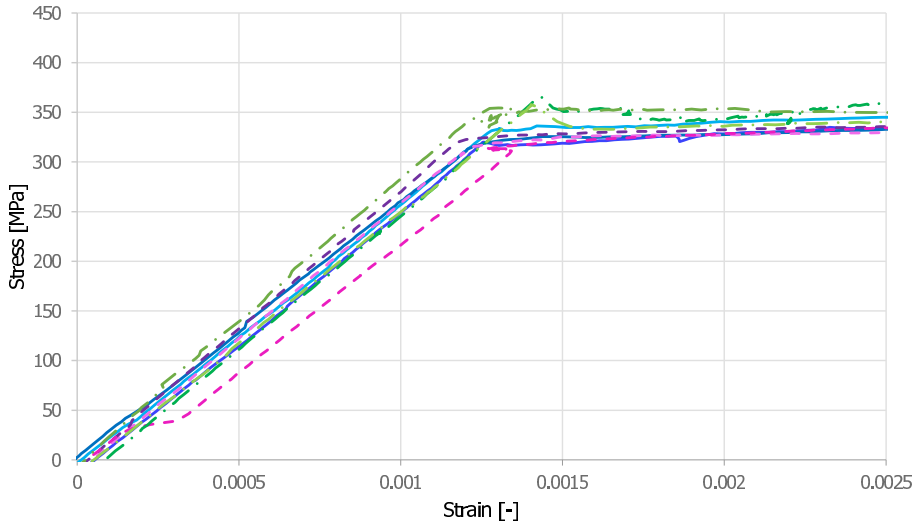

(b) Linear elastic part

Figure E.2: Stress-strain diagram milled thick specimens

F

Appendix as-printed tensile coupon stress-strain curves

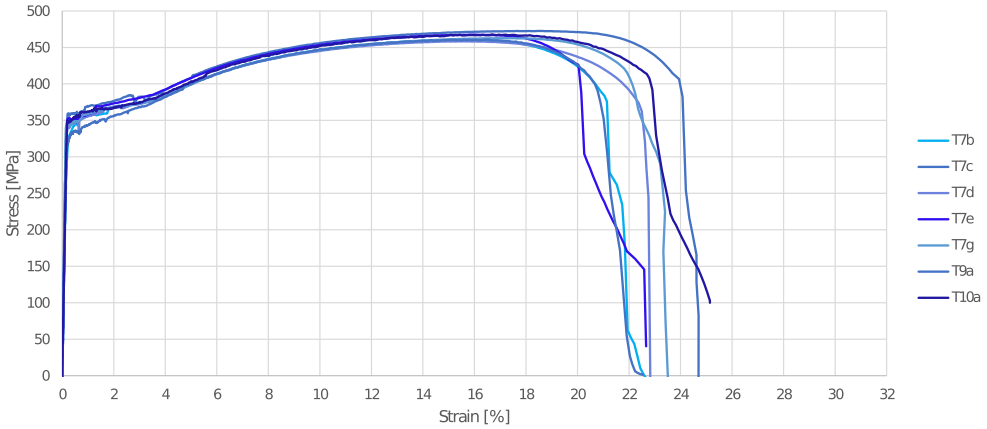

(a) Transversal

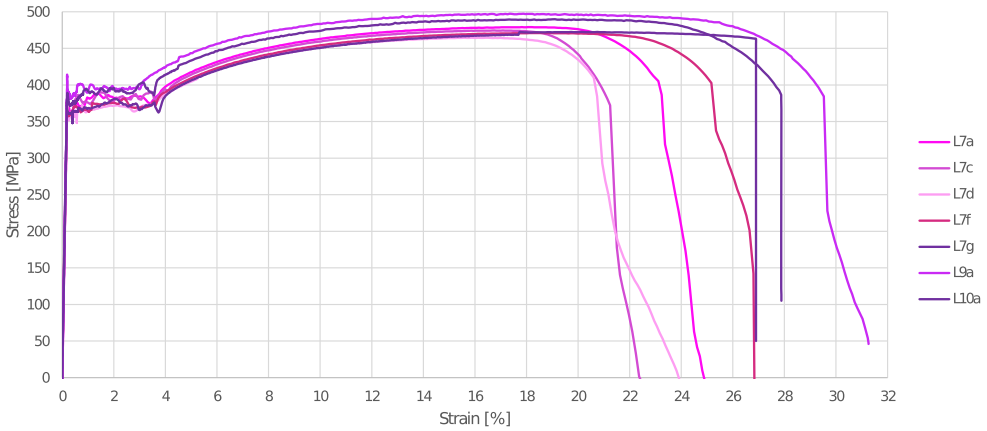

(b) Longitudinal

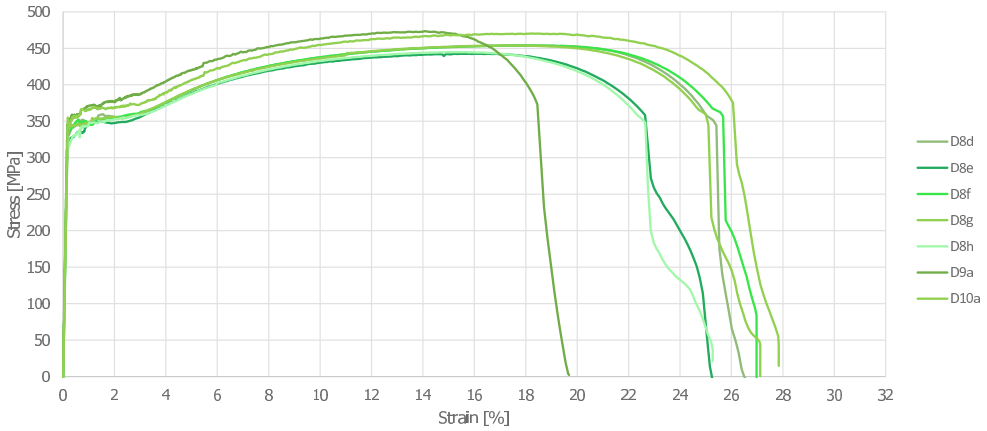

(c) Diagonal

Figure F.1: Stress-strain curves thin as-printed specimens

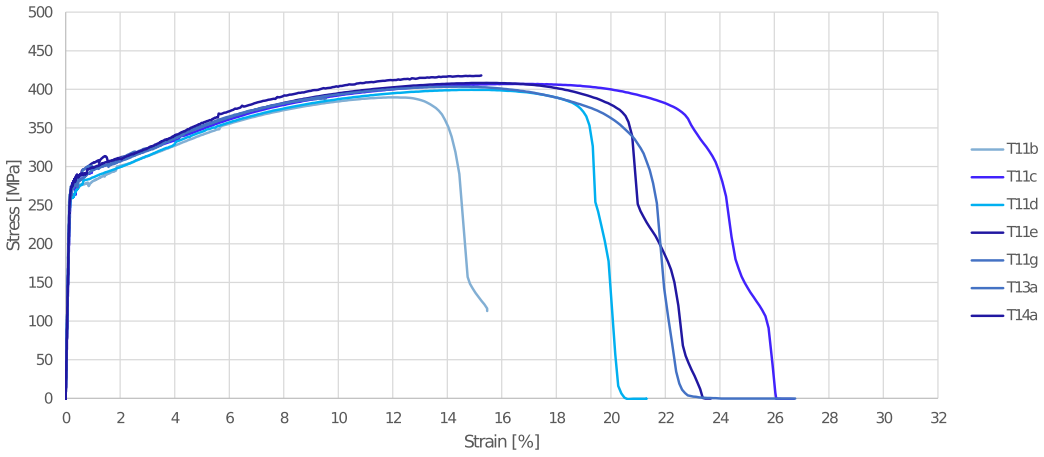

(a) Transversal

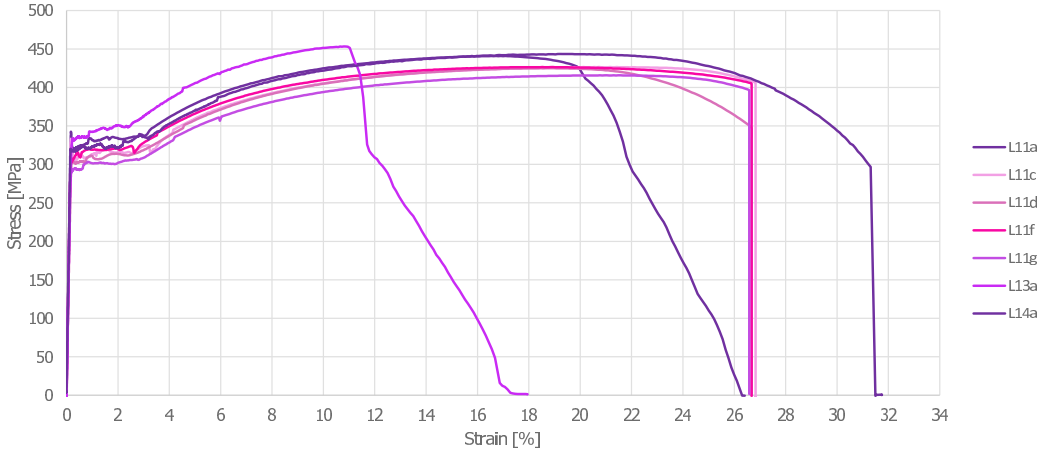

(b) Longitudinal

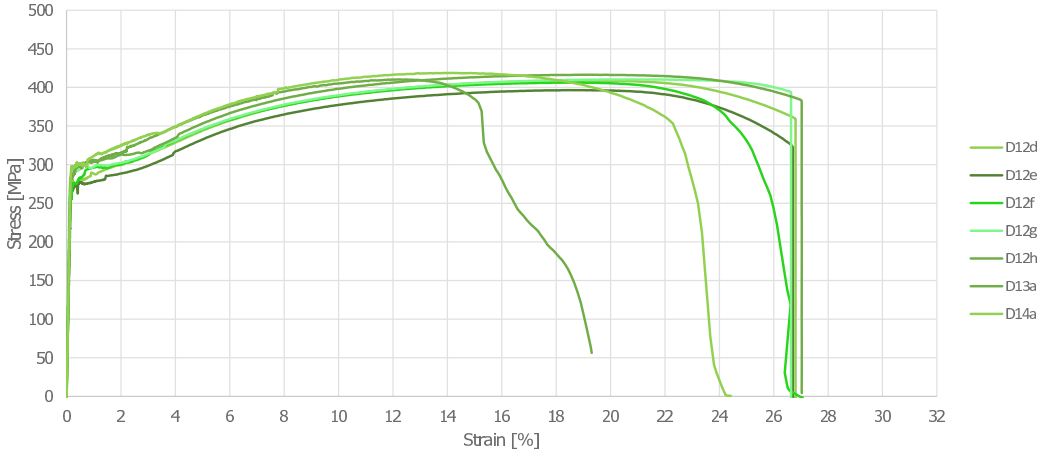

(c) Diagonal

Figure F.2: Stress-strain curves thick as-printed specimens

G

Appendix surface roughness indication as-printed samples

Table G.1: Thickness variation for roughness indication thin specimens

Printing direction	$\mu_{\Delta t}$ **[mm]**	$\sigma_{\Delta t}$ **[mm]**	$V_{\Delta t}$ **[-]**	$SEM_{\Delta t}$ **[mm]**	$SEM_{\Delta t}$ **[%]**	t_{avg} **[mm]**	$\zeta = \mu_{\Delta t} / t_{avg}$ **[-]**
Transversal	0.331	0.0550	0.166	0.0208	6.27	2.645	0.125
Longitudinal	0.392	0.0886	0.226	0.0335	8.54	2.632	0.149
Diagonal 45°	0.272	0.0293	0.108	0.0111	4.07	3.031	0.0898

Table G.2: Thickness variation for roughness indication thick specimens

Printing direction	$\mu_{\Delta t}$ **[mm]**	$\sigma_{\Delta t}$ **[mm]**	$V_{\Delta t}$ **[-]**	$SEM_{\Delta t}$ **[mm]**	$SEM_{\Delta t}$ **[%]**	t_{avg} **[mm]**	$\zeta = \mu_{\Delta t} / t_{avg}$ **[-]**
Transversal	1.281	0.3518	0.275	0.1330	10.4	5.890	0.218
Longitudinal	1.107	0.2476	0.224	0.0936	8.45	5.936	0.187
Diagonal 45°	1.087	0.2626	0.242	0.0993	9.13	6.013	0.181

H

Appendix overview tear-out sample values

H.1. Experimental results tear-out

Table H.1: Tear-out values thin transversal specimens

Weld direction	Sample name	Connection type	e1-d0/2 measured lab	F max experiment [kN]	F max theory [kN]	fu [MPa]	t average [mm]	reduction factor [-]	t effective [mm]	e1 [mm]	e3 [mm]	b [-]	δ
Transversal	T10A-1	Bolt	12.70	32.1666	28.59	511	3.047	0.90	2.757	21.70	17.58	1.125	1.009
	T10A-2	Bolt	12.11	31.9365	27.63	511	3.047	0.90	2.757	21.11	16.99	1.156	1.036
	T10A-3	Pin	13.28	32.7234	29.54	511	3.047	0.90	2.757	22.28	18.16	1.108	0.993
	T10B-1	Pin	13.13	31.6013	29.37	511	3.054	0.90	2.764	22.13	18.01	1.076	0.965
	T10C-1	Pin	12.00	29.1966	27.63	511	3.066	0.90	2.775	21.00	16.88	1.057	0.947
	T10C-2	Bolt	12.90	32.9640	29.11	511	3.066	0.90	2.775	21.90	17.78	1.133	1.015
	T10C-3	Bolt	14.09	35.8278	31.06	511	3.066	0.90	2.775	23.09	18.97	1.154	1.034
	T10B-2	Bolt	30.59	57.9553	57.84	511	3.054	0.90	2.764	39.59	35.47	1.002	0.898
	Average/mean μ					511	3.056		2.766		17.76	1.115	1.000
	Standard deviation σ					12.27785			0.008941		0.71721		0.034
	Coefficient of Variation V					0.024027			0.003233		0.040374		0.034

Table H.2: Tear-out values thin longitudinal specimens

Weld direction	Sample name	Connection type	e1-d0/2 measured lab	F max experiment [kN]	F max theory [kN]	fu [MPa]	t average [mm]	reduction factor [-]	t effective [mm]	e1 [mm]	e3 [mm]	b [-]	δ
Longitudinal	L9A-2	Bolt	12.25	29.7283	26.61	499	2.851	0.95	2.696	21.25	17.13	1.117327	1.001794
	L9B-1	Bolt	12.70	29.4582	27.34	499	2.855	0.95	2.700	21.7	17.58	1.077312	0.965917
	L9B-2	Bolt	11.89	29.3978	26.08	499	2.855	0.95	2.700	20.89	16.77	1.127041	1.010504
	L9B-3	Pin	12.26	30.0813	26.66	499	2.855	0.95	2.700	21.26	17.14	1.128345	1.011673
	L9C-1	Pin	11.90	29.2931	27.13	499	2.967	0.95	2.806	20.9	16.78	1.079763	0.968114
	L9C-2	Pin	12.68	30.3379	28.39	499	2.967	0.95	2.806	21.68	17.56	1.068594	0.9581
	L9C-3	Pin	12.29	30.2516	27.76	499	2.967	0.95	2.806	21.29	17.17	1.089761	0.977079
	L9A-3	Bolt	30.95	58.7835	55.66	499	2.851	0.95	2.696	39.95	35.83	1.056173	0.946963
	Average/mean μ					499			2.745		17.16	1.098306	0.98474
	Standard deviation σ					5.27417			0.05745		0.325137		0.022654
	Coefficient of Variation V					0.010569			0.02093		0.018949		0.023005

Table H.3: Tear-out values thin diagonal specimens

Weld direction	Sample name	Connection type	e1-d0/2 measured lab	F max experiment [kN]	F max theory [kN]	fu [MPa]	t average [mm]	reduction factor [-]	t effective [mm]	e1 [mm]	e3 [mm]	b [-]	δ
Diagonal	D9A-1	Pin	13.02	31.0597	27.01	484	2.913	0.93	2.700	22.02	17.90	1.150	1.031
	D9B-1	Bolt	12.69	30.1651	27.63	484	3.035	0.93	2.814	21.69	17.57	1.092	0.979
	D9B-2	Bolt	12.24	30.3408	26.92	484	3.035	0.93	2.814	21.24	17.12	1.127	1.011
	D10C-1	Pin	13.03	31.7674	28.06	484	3.025	0.93	2.804	22.03	17.91	1.132	1.015
	D10C-2	Bolt	14.12	34.5113	29.77	484	3.025	0.93	2.804	23.12	19.00	1.159	1.039
	D9A-2	Pin	31.64	35.5727	55.11	484	2.913	0.93	2.700	40.64	36.52	0.645	0.579
	Average/mean μ					484			2.787		17.89689	1.132	1.015
	Standard deviation σ					15.08666			0.04883		0.694154		0.023
	Coefficient of Variation V					0.031171			0.01752		0.038786		0.023

Table H.4: Tear-out values thick transversal specimens

Weld direction	Sample name	Connection type	e1-d0/2 measured lab	F max experiment [kN]	F max theory [kN]	fu [MPa]	t average [mm]	reduction factor [-]	t effective [mm]	e1 [mm]	e3 [mm]	b [-]	δ
Transversal	T14A-1	Pin	10.92	49.4519	43.01	466	5.911	0.86	5.059	19.92	15.80	1.14991	0.994367
	T14A-2	Pin	13.08	52.9956	48.89	466	5.911	0.86	5.059	22.08	17.96	1.084079	0.937441
	T14A-3	Bolt	10.68	51.2982	42.35	466	5.911	0.86	5.059	19.68	15.56	1.211244	1.047405
	T14B-1	Bolt	10.61	48.4101	41.05	466	5.755	0.86	4.926	19.61	15.49	1.17935	1.019824
	T14B-2	Bolt	10.79	49.8093	41.53	466	5.755	0.86	4.926	19.79	15.67	1.199495	1.037245
	T14B-3	Pin	10.68	49.4673	41.23	466	5.755	0.86	4.926	19.68	15.56	1.199682	1.037407
	T14C-1	Pin	13.51	55.4638	50.64	466	5.979	0.86	5.118	22.51	18.39	1.09533	0.94717
	T14C-2	Bolt	14.10	59.7189	52.26	466	5.979	0.86	5.118	23.10	18.98	1.142695	0.988128
	T14C-3	Pin	14.01	59.6093	52.01	466	5.979	0.86	5.118	23.01	18.89	1.146033	0.991014
	Average/mean μ					466	5.882		5.034		16.92	1.156424	1
	Standard deviation σ					3.233			0.085322		1.578288		0.039346
	Coefficient of Variation V					0.006938			0.016948		0.093284		0.039346

Table H.5: Tear-out values thick longitudinal specimens

Weld direction	Sample name	Connection type	e1-d0/2 measured lab	F max experiment [kN]	F max theory [kN]	fu [MPa]	t average [mm]	reduction factor [-]	t effective [mm]	e1 [mm]	e3 [mm]	b [-]	δ
Longitudinal	L13A-1	Pin	15.14	55.6993	57.04	463	5.666	0.94	5.330	24.14	20.02	0.976458	0.94857
	L13A-2	Pin	15.12	54.3446	56.99	463	5.666	0.94	5.330	24.12	20.00	0.953662	0.926425
	L13A-3	Bolt	15.63	58.7566	58.44	463	5.666	0.94	5.330	24.63	20.51	1.005443	0.976727
	L13B-1	Bolt	14.40	57.4629	57.98	463	5.980	0.94	5.626	23.40	19.28	0.991051	0.962746
	L13B-2	Bolt	15.12	60.245	60.15	463	5.980	0.94	5.626	24.12	20.00	1.001623	0.973016
	L13B-3	Pin	14.58	60.7908	58.52	463	5.980	0.94	5.626	23.58	19.46	1.038748	1.00908
	L13C-1	Pin	11.77	56.4671	49.67	463	5.932	0.94	5.581	20.77	16.65	1.136899	1.104428
	L13C-2	Bolt	10.62	48.8929	46.24	463	5.932	0.94	5.581	19.62	15.50	1.057452	1.027251
	L13C-3	Pin	11.49	53.875	48.83	463	5.932	0.94	5.581	20.49	16.37	1.103267	1.071757
	L13A-4	Bolt	25.32	77.384	86.05	463	5.666	0.94	5.330	34.32	30.20	0.899269	0.873585
	Average/mean μ					463	5.859		5.512		18.64	1.0294	1
	Standard deviation σ					5.503461			0.137962		1.909025		0.058732
	Coefficient of Variation V					0.011887			0.025028		0.102414		0.058732

Table H.6: Tear-out values thick diagonal specimens

Weld direction	Sample name	Connection type	e1-d0/2 measured lab	F max experiment [kN]	F max theory [kN]	fu [MPa]	t average [mm]	reduction factor [-]	t effective [mm]	e1 [mm]	e3 [mm]	b [-]	δ
Diagonal	D13A-1	Bolt	12.60	50.4739	48.54	468	5.962	0.86	5.140	21.60	17.48	1.039748	0.930503
	D13A-2	Bolt	12.77	54.7412	49.02	468	5.962	0.86	5.140	21.77	17.65	1.11679	0.999451
	D13A-3	Pin	13.51	61.8135	51.07	468	5.962	0.86	5.140	22.51	18.39	1.21032	1.083154
	D13B-1	Pin	13.15	49.6693	50.98	468	6.071	0.86	5.233	22.15	18.03	0.974244	0.871882
	D13B-2	Bolt	12.90	53.2843	50.28	468	6.071	0.86	5.233	21.90	17.78	1.059849	0.948493
	D13B-3	Pin	14.03	62.5542	53.47	468	6.071	0.86	5.233	23.03	18.91	1.169868	1.046952
	D14C-1	Pin	13.00	53.5493	49.04	468	5.889	0.86	5.077	22.00	17.88	1.091859	0.977139
	D14C-2	Bolt	12.26	58.0253	47.01	468	5.889	0.86	5.077	21.26	17.14	1.234212	1.104536
	D14C-3	Pin	14.20	60.6965	52.34	468	5.889	0.86	5.077	23.20	19.08	1.15974	1.037889
	Average/mean μ					468	5.974		5.150		18.03	1.117403	1
	Standard deviation σ					3.393722			0.06828		0.64517		0.075748
	Coefficient of Variation V					0.007252			0.013258		0.035774		0.075748

H.2. Bolt pin agreement tear-out tests

(a) Thin specimens

Weld direction	Normalised force [-] bolt	pin	Δ bolt versus pin [%]
Transversal	1.2125	1.1578	
	1.1866	1.0741	
	1.1541	1.1139	
	1.1256		
mean μ	1.1697	1.1153	4.65
SEM [%]	1.6194	2.1674	
Longitudinal	1.0764	1.112	
	1.1292	1.1325	
	1.117	1.1291	
		1.1367	
mean μ	1.1075	1.1276	-1.81
SEM [%]	1.4410	0.4806	
Diagonal	1.2031	1.1747	
	1.1742	1.1461	
	1.1446		
mean μ	1.1740	1.1604	1.16
SEM [%]	1.4385	1.2323	

(b) Thick specimens

Weld direction	Normalised force [-] bolt	pin	Δ bolt versus pin [%]
Transversal	1.2355	1.1989	
	1.1414	1.0936	
	1.1978	1.0839	
	1.2013	1.1351	
		1.1397	
mean μ	1.1940	1.1302	5.34
SEM [%]	1.6320	1.8043	
Longitudinal	1.0552	1.1356	
	1.0047	1.1019	
	0.99	1.0373	
	0.9999	0.9536	
		0.9762	
mean μ	1.0125	1.0409	-2.81
SEM [%]	1.4396	3.3631	
Diagonal	1.2181	0.9735	
	1.1162	1.0902	
	1.0392	1.2099	
	1.0591	1.1678	
		1.1595	
mean μ	1.1082	1.1202	-1.09
SEM [%]	3.6203	3.6957	

Table H.7: Bolt pin agreement tear-out tests

Appendix tear-out curves

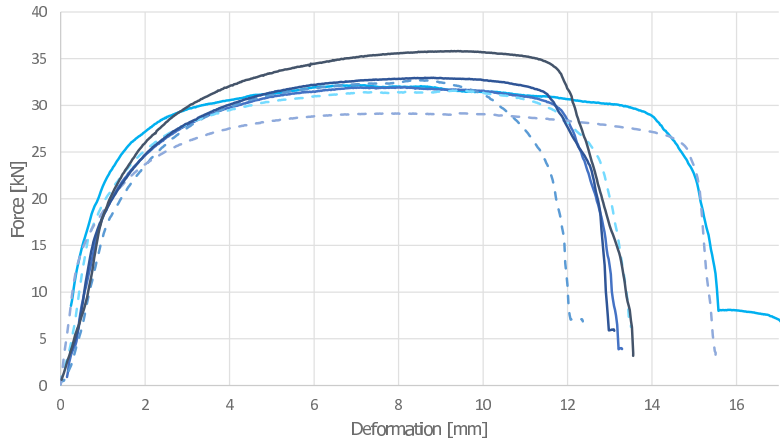

(a) Transversal

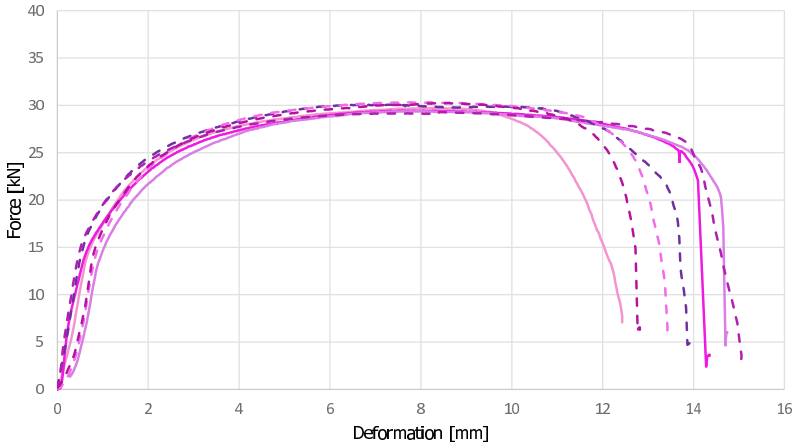

(b) Longitudinal

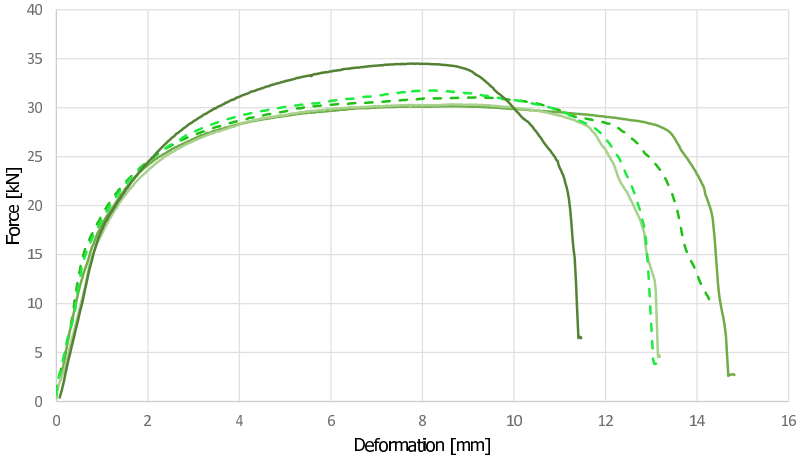

(c) Diagonal

Figure I.1: Tear-out force-deformation curves thin specimens

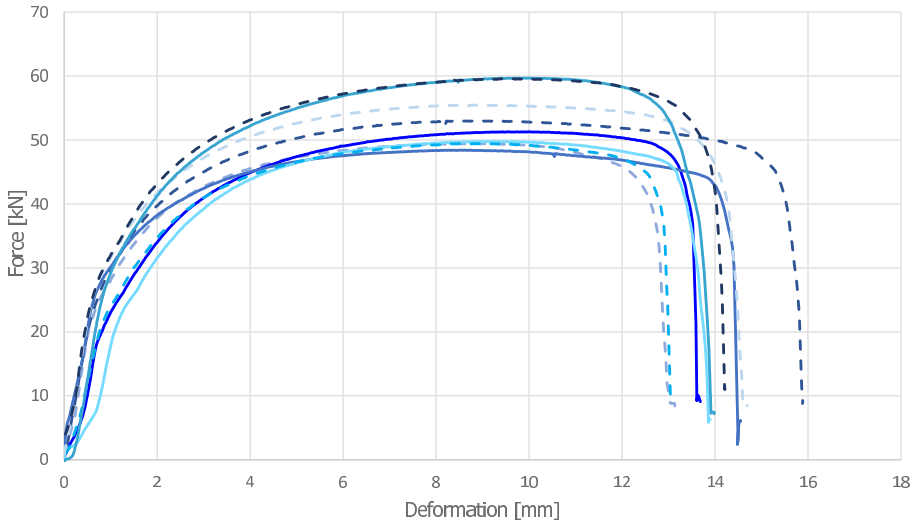

(a) Transversal

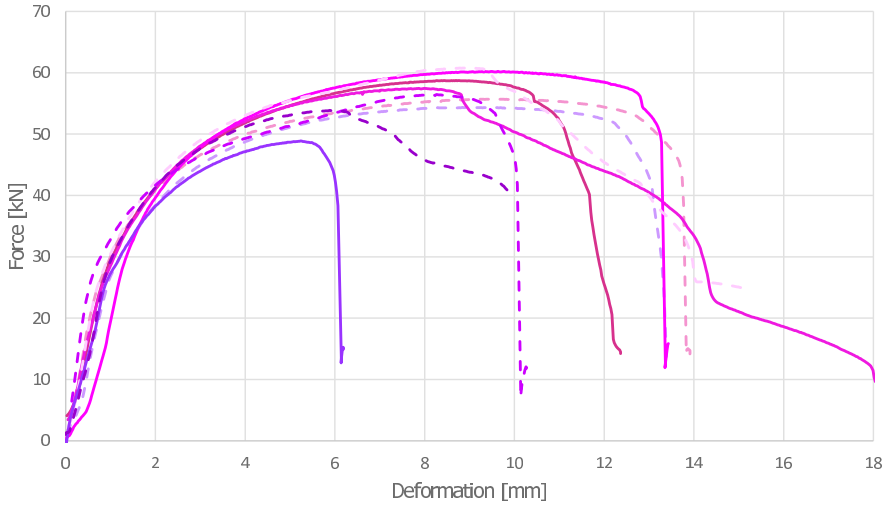

(b) Longitudinal

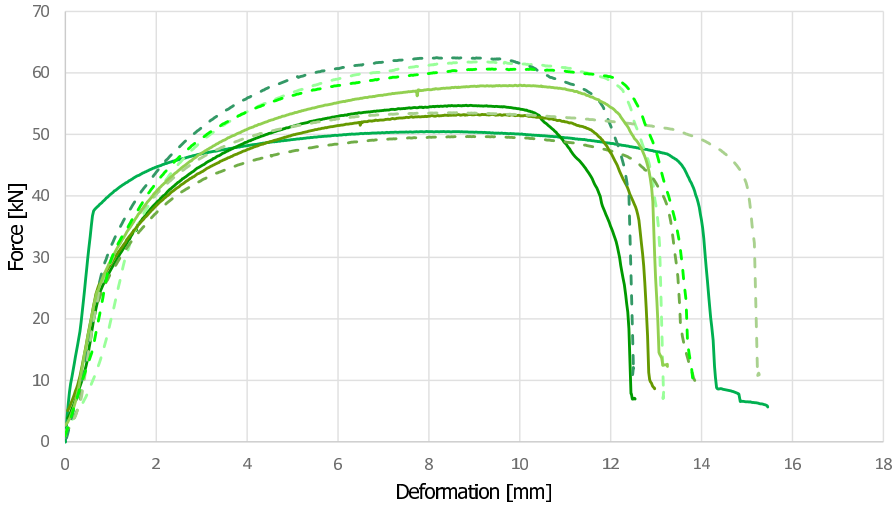

(c) Diagonal

Figure I.2: Tear-out force-deformation curves thick specimens

J

Appendix normalised tear-out curves

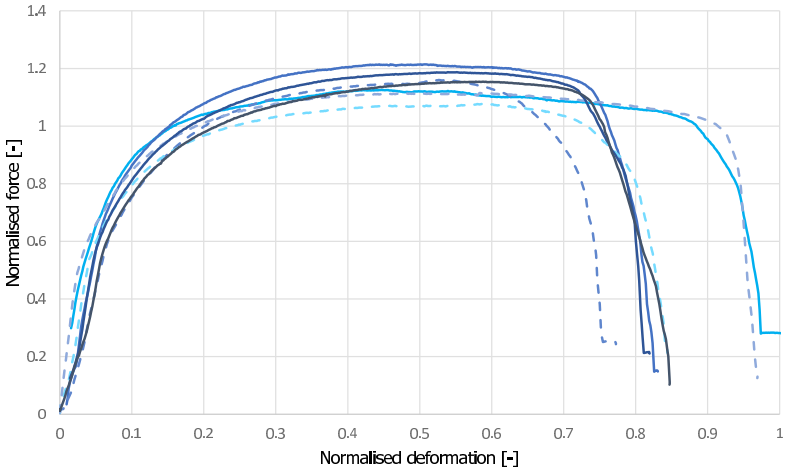

(a) Transversal

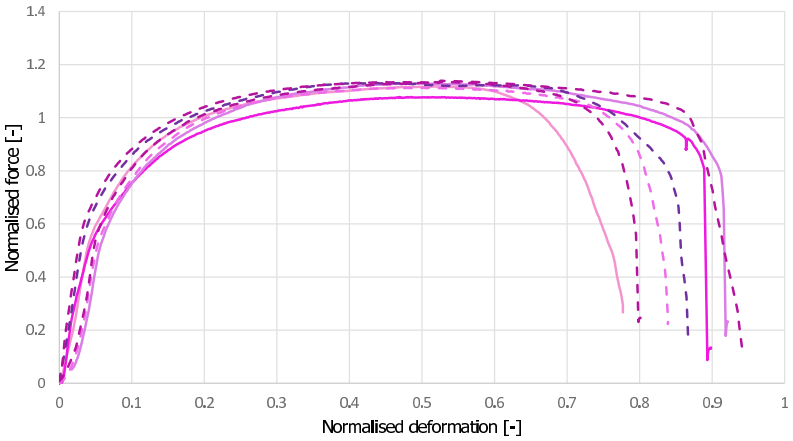

(b) Longitudinal

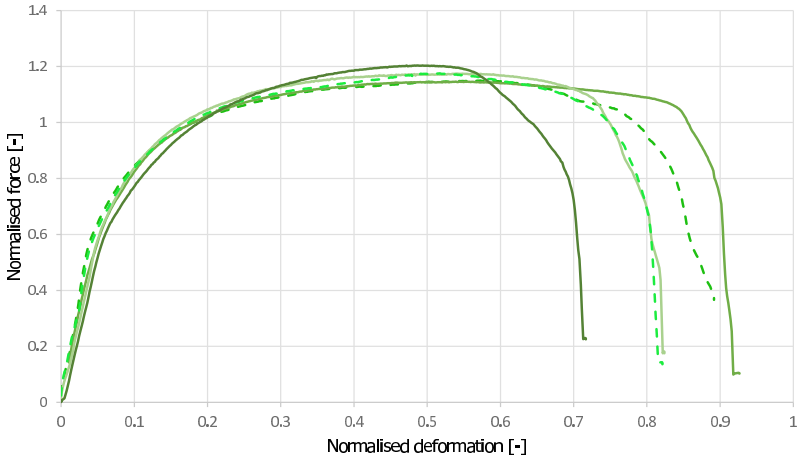

(c) Diagonal

Figure J.1: Normalised tear-out curves thin specimens

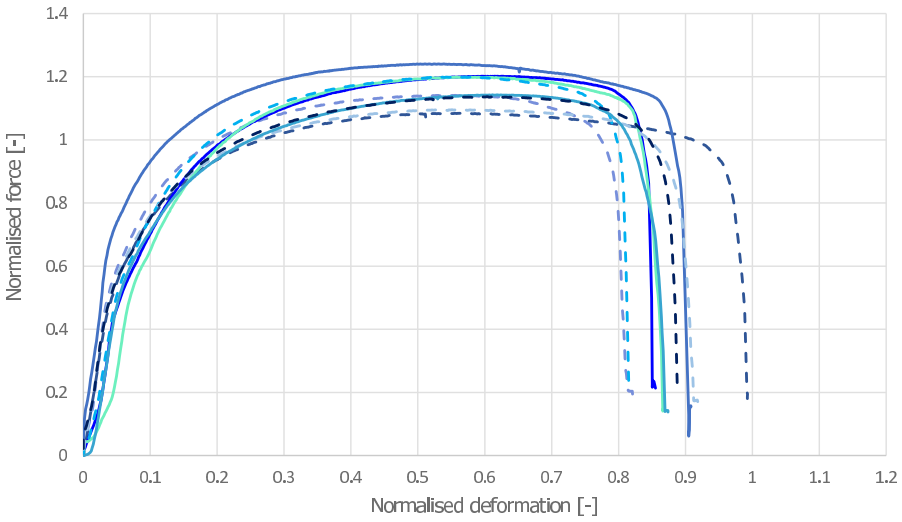

(a) Transversal

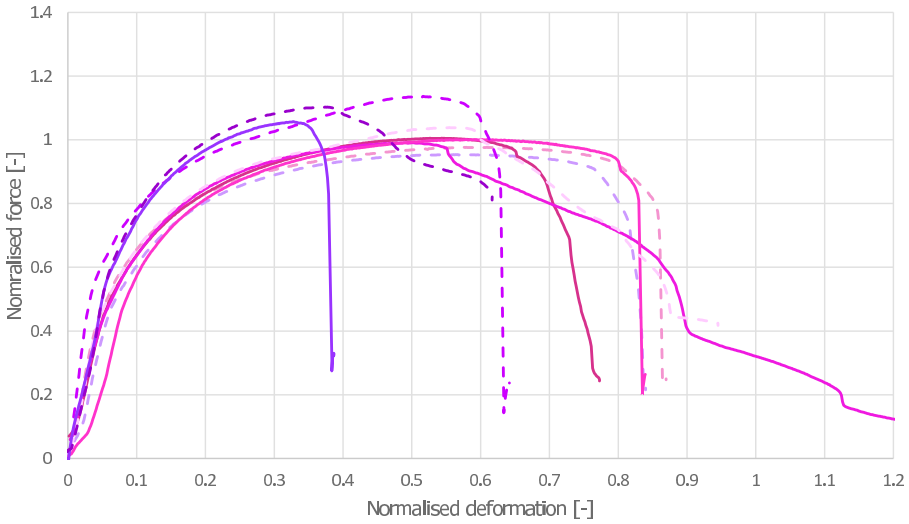

(b) Longitudinal

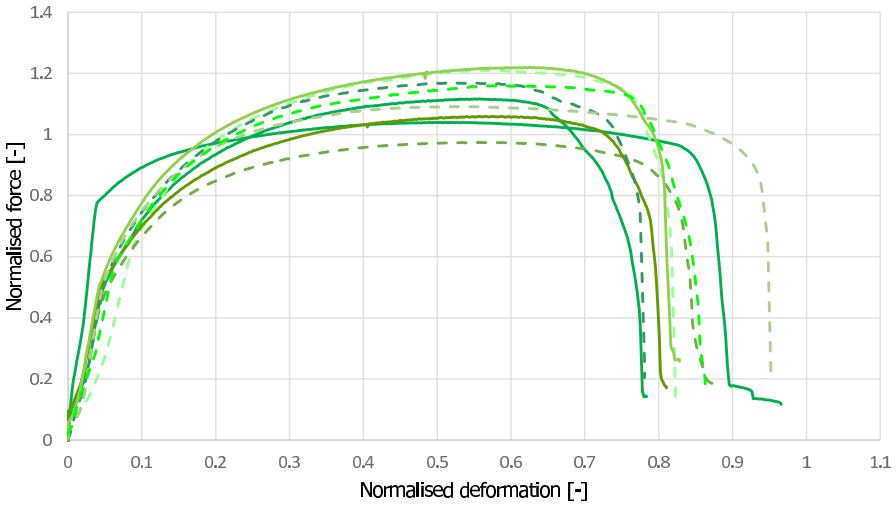

(c) Diagonal

Figure J.2: Normalised tear-out curves thick specimens

K

Appendix DIC

K.1. Paint DIC

The Digital Image Correlation (DIC) specimens had to be painted in order to detect the strains in the samples via photographs.

The white metal spray did not result in the wanted images, due to fast detaching and cracking of the paint when the specimen elongated. The first two tensile coupon specimens were painted with the metal spray. The others were painted with a water-based wall paint. This resulted in corrosion of the surface; small brown-orange dots appeared through the paint. The white metal water-based wall paint was not flexibel enough when the specimen was torn apart; it was peeled off, so it was not possible to track the strains by the DIC and therefore the cracks. A new idea had to be brought up; the use of rubber paint instead. This flexibel paint stretched along with the elongation, like a rubber band and stayed on the specimen, even after failure.

The first rubber painted samples that were tested on tear-out were not suitable for DIC, especially not for the large deformations just before tear-out failure. The paint layer was applied on top of the black oxide layer, which is the first to come off when large forces are applied on the steel and therefore large deformations occur. This caused the paint layer to peel off as well.

To overcome this problem, the specimens were sandblasted and the oxide layer was removed, so the paint was stuck onto the printed steel itself and could deform according to the steel. In figure K.1a a tested thin tear-out sample can be seen, where the paint layer is pulled off, because it was not sandblasted. In figure K.1b a specimen before testing is shown, where the part around the hole is painted. The part nearest to the hole is sandblasted and is more steel-coloured. The black part is the non-sandblasted part with the oxide layer.

K.2. Tear-out DIC

The tear-out DIC results are not analysed, as is explained in section 5.1.6. In figure K.2 two shots of the major strains during the tear-out test is taken of a transversal and a longitudinal pinned connection. Figure 4.8 shows the direction of the welds, compared to the applied force. In figure K.2a of the transversal specimen strains are largest in the printing direction, so perpendicular to the force. The strains are also largest in the direction of the welds for the longitudinal specimen, as can be seen in figure K.2b, so in the direction of the force.

The pictures show that different end distances e_1 are used; 19.92mm for the transversal sample T14A-1 (figure K.2a) and 24.14 mm for the longitudinal L13A-1 (figure K.2b). The dimensions can also be seen in appendix H. The end distance that is visible during DIC equals $e_1 - \frac{d_0}{2} + \frac{d}{2}$.

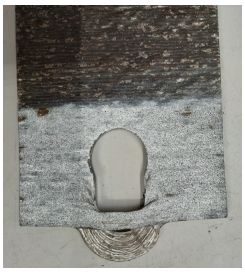

(a) Tested thin sample with paint on oxide layer

(b) Half sandblasted thick sample

Figure K.1: Sandblasting tear-out samples

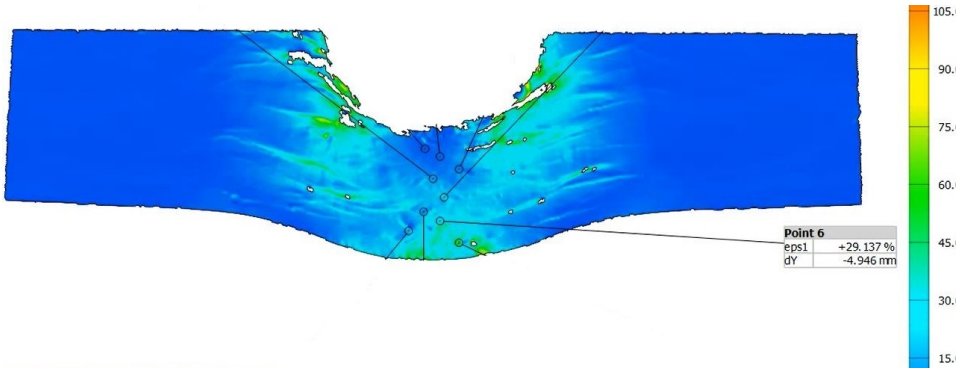

(a) Transversal

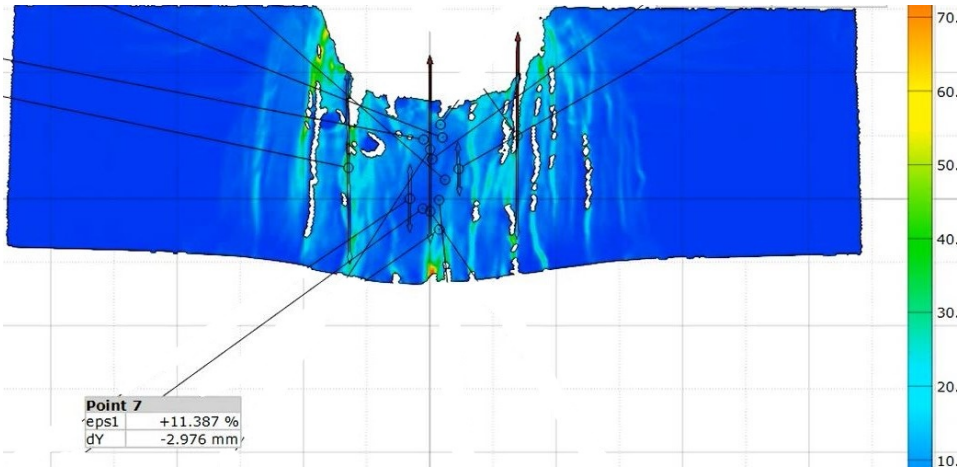

(b) Longitudinal

Figure K.2: Major strains of tear-out with a pinned connection, analysed by DIC

L

Appendix fracture line tear-out specimens

The orange numbers in table L.2 indicate a tensile failure instead of a shear failure, as can be seen in picture L.1.

Table L.1: Fracture lines thin tear-out specimens

Sample name	End distance e3 [mm]	fracture line including hole elongation [mm]	fracture line Lf [mm]	ξ = e3/Lf [-]	Sample name	End distance e3 [mm]	fracture line including hole elongation [mm]	fracture line Lf [mm]	ξ = e3/Lf [-]	Sample name	End distance e3 [mm]	fracture line including hole elongation [mm]	fracture line Lf [mm]	ξ = e3/Lf [-]
T10A-1	17.58	21.5	10.0	1.76	L9A-2	17.13	18.5	10.0	1.71	D9A-1	17.90	21.5	12.5	0.14
T10A-2	16.99	18.0	10.5	1.62	L9B-1	17.58	20.5	8.5	2.07	D9B-1	17.57	18.0	9.0	0.18
T10A-3	18.16	19.5	12.0	1.51	L9B-2	16.77	21.0	10.5	1.60	D9B-2	17.12	17.0	12.0	0.13
T10B-1	18.01	20.5	10.5	1.71	L9B-3	17.14	18.5	10.0	1.71	D10C-1	17.91	17.0	11.0	0.16
T10C-1	16.88	17.5	9.0	1.88	L9C-1	16.78	19.0	10.0	1.68	D10C-2	19.00	18.0	13.0	0.14
T10C-2	17.78	19.5	11.5	1.55	L9C-2	17.56	19.0	9.0	1.95	μ		18.3	11.5	**0.15**
T10C-3	18.97	21.5	13.0	1.46	L9C-3	17.17	21.0	11.0	1.56	σ				0.0201
Average/mean μ		19.7	10.9	**1.64**	μ		19.6	9.86	**1.75**	V				0.134
Standard deviation σ				0.149	σ				0.186	SEM				0.00897
Coefficient of Variation V				0.0563	V				0.106					
SEM				0.0563	SEM				0.0705					

Table L.2: Fracture lines thick tear-out specimens

Sample name	End distance e3 [mm]	fracture line including hole elongation [mm]	fracture line Lf [mm]	ξ = e3/Lf [-]	Sample name	End distance e3 [mm]	fracture line including hole elongation [mm]	fracture line Lf [mm]	ξ = e3/Lf [-]	Sample name	End distance e3 [mm]	fracture line including hole elongation [mm]	fracture line Lf [mm]	ξ = e3/Lf [-]
T14A-1	15.80	19.0	10	1.58	L13A-1	20.02	23.0	12.0	1.67	D13A-1	17.48	20.0	10.0	1.75
T14A-2	17.96	21.0	12.5	1.44	L13A-2	20.00	20.0	12.0	1.67	D13A-2	17.65	19.0	11.0	1.60
T14A-3	15.56	17.5	9.5	1.64	L13A-3	20.51	22.0	13.5	1.52	D13A-3	18.39	21.0	12.0	1.53
T14B-1	15.49	18.0	8.0	1.94	L13B-1	19.28	26.0	11.0	1.75	D13B-1	18.03	20.0	9.5	1.90
T14B-2	15.67	18.0	10.0	1.57	L13B-2	20.00	22.0	12.0	1.67	D13B-2	17.78	18.0	11.5	1.55
T14B-3	15.56	18.0	9.0	1.73	L13B-3	19.46	26.5	11.5	1.69	D13B-3	18.91	23.5	14.0	1.35
T14C-1	18.39	21.5	10.5	1.75	L13C-1	16.65	18.0	11.0	1.51	D14C-1	17.88	20.0	9.5	1.88
T14C-2	18.98	19.0	9.0	2.11	L13C-2	15.50	16.5	12.0	1.29	D14C-2	17.14	18.5	12.0	1.43
T14C-3	18.89	23.5	11.0	1.72	L13C-3	16.37	24.5	10.0	1.64	D14C-3	19.08	22.5	11.5	1.66
Average/mean μ		19.5	9.94	**1.72**	μ		22.1	11.67	**1.60**	μ		20.3	11.2	**1.63**
Standard deviation σ				0.203	σ				0.140	σ				0.189
Coefficient of Variation V				0.118	V				0.0872	V				0.116
SEM				0.0676	SEM				0.0465	SEM				0.0630

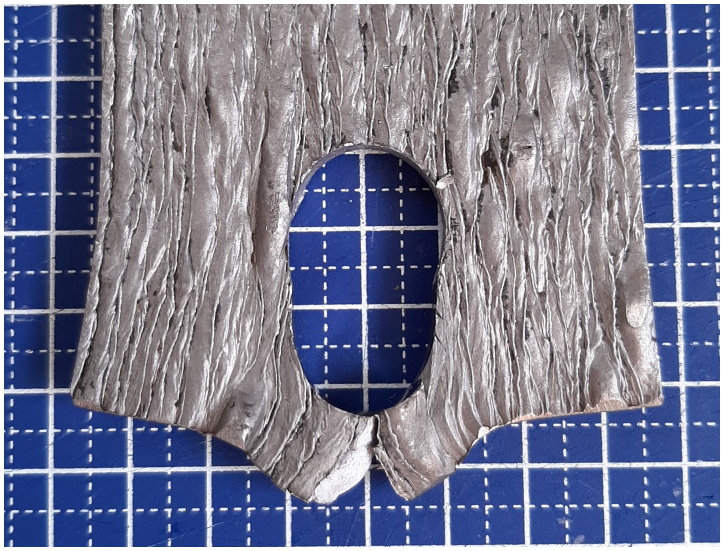

Figure L.1: Tensile failure of longitudinal thick tear-out specimen

M

Appendix pores

Figure M.1: Pores in tensile coupon

In the first printed object a weld was printed incorrectly, as the robot ran out of shielding gases and pores arose in the object along the whole weld. The transversal tensile coupons were cut out of the object and tested. This resulted in failure along the same weld, namely where the pores where incorporated, as can be seen in figure M.1. A controlled printing process is very important to prevent these inconsistencies in the material.


TU Delft